

APPENDIX E

IMPACT ASSESSMENT APPROACH AND RESULTS

This page intentionally left blank.

CONTENTS

E.1.0	INTRODUCTION	E-1
E.2.0	MODELING APPROACH.....	E-2
E.2.1	NUMERICAL CASES CONSIDERED.....	E-7
E.2.2	RECHARGE ESTIMATES AND VADOSE ZONE FLOW AND TRANSPORT PARAMETERS.....	E-9
E.2.2.1	Recharge Estimates.....	E-9
E.2.2.2	Vadose Zone Flow and Transport Parameters.....	E-9
E.2.2.3	Stochastic Model for Macroscopic Anisotropy	E-10
E.2.2.4	Clastic Dike Infilling Material Properties.....	E-12
E.2.2.5	Enhanced Density and Viscosity Estimates.....	E-12
E.2.2.6	Effective Transport Parameters.....	E-12
E.2.3	GROUNDWATER FLOW AND TRANSPORT.....	E-14
E.2.3.1	Flow and Transport Parameters	E-14
E.2.3.2	Unit Dose Factors	E-17
E.2.4	CONTAMINANT INVENTORY	E-17
E.2.4.1	Basis for Inventory Estimates	E-17
E.2.4.2	Inventory Distributions	E-21
E.2.4.3	Inventory Assignment.....	E-22
E.3.0	HUMAN HEALTH RISK AND DOSE ESTIMATION APPROACH	E-29
E.3.1	RECEPTOR SCENARIO RATIONALE	E-30
E.3.1.1	Residential Exposure Scenario (MTCA Method B)	E-31
E.3.1.2	Industrial Exposure Scenario (MTCA Method C).....	E-31
E.3.1.3	Industrial Worker Scenario	E-32
E.3.1.4	Residential Farmer Scenario	E-33
E.3.1.5	Recreational Shoreline User Scenario	E-34
E.3.2	TANK WASTE CONSTITUENTS OF POTENTIAL CONCERN.....	E-34
E.3.2.1	Rationale for Excluding Contaminants of Potential Concern.....	E-34
E.3.2.2	Contaminants of Potential Concern for Risk Assessment	E-35
E.3.3	ESTIMATING TOTAL INCREMENTAL LIFETIME CANCER RISK AND HAZARD INDEX.....	E-36
E.3.4	DOSE METHODOLOGY	E-36
E.4.0	VADOSE ZONE MODELING RESULTS.....	E-38
E.4.1	BASE CASE, NO ACTION ALTERNATIVE (CASE 1).....	E-38
E.4.2	BARRIER ALTERNATIVE AND NO WATER-LINE LEAKS CASE (CASE 2).....	E-43
E.4.3	NO BARRIER AND 25,000 GALLON WATER-LINE LEAK CASE (CASE 3).....	E-44
E.4.4	NO BARRIER AND CLASTIC DIKES CASE (CASE 4)	E-51
E.4.5	NONUNIFORM INVENTORY DISTRIBUTION AND NO BARRIER CASE (CASE 5)	E-52
E.4.6	NONUNIFORM INVENTORY DISTRIBUTION AND BARRIER CASE (CASE 6).....	E-53

E.4.7	LOCATION OF INVENTORY DISTRIBUTION AND NO BARRIER CASE (CASE 7)	E-54
E.4.8	DENSITY AND VISCOSITY EFFECTS CASE (CASE 8)	E-55
E.4.9	BASE CASE WITH 50 MM/YR METEORIC RECHARGE CASE (CASE 9).....	E-56
E.4.10	BASE CASE WITH 30 MM/YR METEORIC RECHARGE (CASE 10)	E-59
E.4.11	BASE CASE WITH 10 MM/YR METEORIC RECHARGE (CASE 11)	E-61
E.4.12	ALTERNATE INVENTORY DISTRIBUTION CASE (CASE 12).....	E-64
E.4.13	NO BARRIER AND 200,000 GAL WATER-LINE LEAK CASE (CASE 13).....	E-65
E.4.14	THREE-DIMENSIONAL SIMULATIONS	E-72
E.4.15	SOLUTE MASS BALANCE	E-73
E.5.0	STREAMTUBE MODELING RESULTS	E-75
E.6.0	HUMAN HEALTH RISK AND DOSE RESULTS.....	E-81
E.6.1	BASE CASE, NO ACTION ALTERNATIVE (CASE 1).....	E-82
E.6.2	BARRIER ALTERNATIVE AND NO WATER-LINE LEAKS CASE (CASE 2).....	E-85
E.6.3	BASE CASE WITH 50 MM/YR METEORIC RECHARGE (CASE 9)	E-88
E.6.4	BASE CASE WITH 30 MM/YR METEORIC RECHARGE (CASE 10)	E-91
E.6.5	BASE CASE WITH 10 MM/YR METEORIC RECHARGE (CASE 11)	E-94
E.7.0	REFERENCES	E-97

ATTACHMENTS

E1	VADOSE ZONE INVENTORY ESTIMATES	E1-i
E2	INVENTORY DISTRIBUTIONS	E2-i
E3	VADOSE ZONE AND UNCONFINED AQUIFER MODELING RESULTS	E3-i
E4	SOLUTE TRANSPORT TIME SEQUENCES	E4-i
E5	RECHARGE SENSITIVITY MODELING RESULTS.....	E5-i

FIGURES

E.1.	Location Map of Single-Shell Tank WMA S-SX and Surrounding Facilities in the 200 West Area.....	E-3
E.2.	Cross-Section SX-DD'	E-4
E.3.	Cross-Section SX-FF'	E-4
E.4.	Cross-Section S-CC'	E-5
E.5.	VAM3D-Generated Steady State Hydraulic Head Distribution for the Hanford Site, Following Simulation for 1,000 Years.....	E-15
E.6.	VAM3D-Generated Pathline Distribution at Steady State, Following Simulation for 1,000 Years	E-16
E.7.	Material Property Distribution for the Upper Three Elemental Layers for VAM3D Sitewide Groundwater Model	E-18
E.8.	Case 1 Aqueous-Phase Saturation at 2000 (steady-flow conditions) for Cross-Section SX-DD'	E-40
E.9.	Case 1 Aqueous-Phase Saturation at 2050 (0.1 mm/yr) for Cross-Section SX-DD'	E-41
E.10.	Case 1 Aqueous-Phase Saturation at 2540 (0.1 mm/yr) for Cross-Section SX-DD'	E-42
E.11.	Case 1 Aqueous-Phase Saturation at 3000 (3.5 mm/yr) for Cross-Section SX-DD'	E-42
E.12.	Case 3 Aqueous-Phase Saturation at 2000 plus 5 days for Cross-Section SX-FF'	E-46
E.13.	Case 3 Aqueous-Phase Saturation at 2000 plus 10 days for Cross-Section SX-FF'	E-46
E.14.	Case 3 Aqueous-Phase Saturation at 2000 plus 25 days for Cross-Section SX-FF'	E-47
E.15.	Case 3 Aqueous-Phase Saturation at 2000 plus 50 days for Cross-Section SX-FF'	E-47
E.16.	Case 3 Aqueous-Phase Saturation at 2000 plus 183 days for Cross-Section SX-FF' ..	E-48
E.17.	Case 3 Aqueous-Phase Saturation at 2000 plus 365 days for Cross-Section SX-FF' ..	E-48
E.18.	Case 3 Technetium-99 Aqueous Concentration at 2001 for Cross-Section SX-FF'	E-49
E.19.	Case 3 Technetium-99 Aqueous Concentration at 2040 for Cross-Section SX-FF'	E-50
E.20.	Case 9 Aqueous-Phase Saturation at 2000 (50 mm/yr) for Cross-Section SX-DD'	E-58
E.21.	Case 10 Aqueous-Phase Saturation at 2000 (30 mm/yr) for Cross-Section SX-DD' ...	E-61
E.22.	Case 11 Aqueous-Phase Saturation at 2000 (50 mm/yr) for Cross-Section SX-DD' ...	E-63
E.23.	Case 13 Aqueous-Phase Saturation at 2000 plus 5 days for Cross-Section SX-FF'	E-66
E.24.	Case 13 Aqueous-Phase Saturation at 2000 plus 10 days for Cross-Section SX-FF' ..	E-67
E.25.	Case 13 Aqueous-Phase Saturation at 2000 plus 25 days for Cross-Section SX-FF' ..	E-67
E.26.	Case 13 Aqueous-Phase Saturation at 2000 plus 50 days for Cross-Section SX-FF' ..	E-68
E.27.	Case 13 Aqueous-Phase Saturation at 2000 plus 183 days for Cross-Section SX-FF'	E-68
E.28.	Case 13 Aqueous-Phase Saturation at 2000 plus 365 days for Cross-Section SX-FF'	E-69
E.29.	Case 13 Technetium-99 Aqueous Concentration at 2001 for Cross-Section SX-FF' ..	E-71
E.30.	Case 13 Technetium-99 Aqueous Concentration at 2040 for Cross-Section SX-FF' ..	E-71
E.31.	Translation Geometry	E-77
E.32.	Case 1 Industrial Worker ILCR Versus Time at WMA S-SX Boundary	E-83
E.33.	Case 1 Industrial Worker ILCR Versus Time at Compliance Points Between the WMA S-SX Boundary and the Columbia River.....	E-83
E.34.	Case 2 Industrial Worker ILCR Versus Time at WMA S-SX Boundary	E-85
E.35.	Case 2 Industrial Worker ILCR Versus Time at Compliance Points Between the WMA S-SX Boundary and the Columbia River.....	E-86
E.36.	Case 9 Industrial Worker ILCR Versus Time at WMA S-SX Boundary	E-88

E.37.	Case 9 Industrial Worker ILCR Versus Time at Compliance Points Between the WMA S-SX Boundary and the Columbia River.....	E-89
E.38.	Case 10 Industrial Worker ILCR Versus Time at WMA S-SX Boundary	E-91
E.39.	Case 10 Industrial Worker ILCR Versus Time at Compliance Points Between the WMA S-SX Boundary and the Columbia River.....	E-92
E.40.	Case 11 Industrial Worker ILCR Versus Time at WMA S-SX Boundary	E-94
E.41.	Case 11 Industrial Worker ILCR Versus Time at Compliance Points Between the WMA S-SX Boundary and the Columbia River.....	E-95

TABLES

E.1.	Timeline Estimates for Emplacement of Interim and Closure Barriers at the S and SX Tank Farms and Corresponding Recharge Estimates	E-9
E.2.	Composite van Genuchten-Mualem Parameters for Various Strata at the S and SX Tank Farms	E-10
E.3.	Macroscopic Anisotropy Parameters Based on Polmann (1990) Equations for Various Strata at the S and SX Tank Farms	E-12
E.4.	Effective Hydraulic Parameters for Clastic Dike Infilling Materials	E-12
E.5.	Effective Parameter Estimates, $E[\rho_b K_d]$, for Cesium-137 for the Product of Bulk Density (g/cm^3) and K_d (cm^3/g) at WMA S-SX	E-13
E.6.	Non-Reactive Macrodispersivity Estimates for Various Strata at the S and SX Tank Farms.....	E-14
E.7.	Hydraulic Properties for Various Material Types for Site-wide VAM3D Groundwater Model.....	E-19
E.8.	Transport Parameters for the Site-wide Groundwater Model.....	E-20
E.9.	Unit Dose Factors for Cesium-137 and Technetium-99	E-20
E.10.	Initial Inventory Distribution Schedule	E-27
E.11.	Unit Risk Factors for the Industrial Worker, Residential Farmer, and Recreational Shoreline User Scenarios	E-33
E.12.	Basis for Scaled Groundwater Concentrations	E-36
E.13.	Industrial Worker Scenario Groundwater Unit Dose Factors.....	E-37
E.14.	Peak Concentrations and Arrival Times at the First Compliance Point (i.e., WMA S-SX Boundary) for Case 1	E-39
E.15.	Case 1 Mean Aqueous-Phase Saturation	E-43
E.16.	Peak Concentrations and Arrival Times at the First Compliance Point (i.e., WMA S-SX Boundary) for Case 2	E-44
E.17.	Peak Concentrations and Arrival Times at the First Compliance Point (i.e., WMA S-SX Boundary) for Case 3	E-50
E.18.	Peak Concentrations and Arrival Times at the First Compliance Point (i.e., WMA S-SX Boundary) for Case 4.....	E-51
E.19.	Peak Concentrations and Arrival Times at the First Compliance Point (i.e., WMA S-SX Boundary) for Case 5	E-52
E.20.	Peak Concentrations and Arrival Times at the First Compliance Point (i.e., WMA S-SX Boundary) for Case 6.....	E-54
E.21.	Peak Concentrations and Arrival Times at the First Compliance Point (i.e., WMA S-SX Boundary) for Case 7	E-55
E.22.	Peak Concentrations and Arrival Times at the First Compliance Point (i.e., WMA S-SX Boundary) for Case 8.....	E-56
E.23.	Peak Concentrations and Arrival Times at the First Compliance Point (i.e., WMA S-SX Boundary) for Case 9.....	E-57
E.24.	Case 9 Mean Aqueous-Phase Saturation	E-58
E.25.	Peak Concentrations and Arrival Times at the First Compliance Point (i.e., WMA S-SX Boundary) for Case 10	E-60
E.26.	Case 10 Mean Aqueous-Phase Saturation	E-61
E.27.	Peak Concentrations and Arrival Times at the First Compliance Point (i.e., WMA S-SX Boundary) for Case 11	E-62

E.28.	Case 11 Mean Aqueous-Phase Saturation	E-64
E.29.	Peak Concentrations and Arrival Times at the First Compliance Point (i.e., WMA S-SX Boundary) for Case 12	E-65
E.30.	Peak Concentrations and Arrival Times at the First Compliance Point (i.e., WMA S-SX Boundary) for Case 13	E-70
E.31.	Solute Mass Balance Errors	E-74
E.32.	Distances and Travel Times from WMA S-SX	E-75
E.33.	Streamtube Characteristics.....	E-76
E.34.	Streamtube Analysis Summary for Technetium-99.....	E-79
E.35.	Streamtube Analysis Summary for Chromium.....	E-79
E.36.	Streamtube Analysis Summary for Nitrate.....	E-80
E.37.	Human Health Risk and Dose Assessment Cases.....	E-81
E.38.	Peak Long-Term Human Health Impacts for Case 1	E-84
E.39.	Peak Long-Term Human Health Impacts for Case 2.....	E-87
E.40.	Peak Long-Term Human Health Impacts for Case 9.....	E-90
E.41.	Peak Long-Term Human Health Impacts for Case 10.....	E-93
E.42.	Peak Long-Term Human Health Impacts for Case 11	E-96

LIST OF TERMS

BTC	breakthrough curve
CoPCs	contaminants of potential concern
DOE	U.S. Department of Energy
Ecology	Washington State Department of Ecology
EPA	U.S. Environmental Protection Agency
HSRAM	Hanford Site Risk Assessment Methodology
ILCR	incremental lifetime cancer risk
MTCA	Model Toxics Control Act
TWRS EIS	Tank Waste Remediation System Environmental Impact Statement
WMA	waste management area

This page intentionally left blank.

E.1.0 INTRODUCTION

A series of numerical simulations are conducted to evaluate the performance of interim corrective measures such as surface barriers in reducing long-term human health risks from potential groundwater contamination at waste management area (WMA) S-SX. The specific objectives of the numerical assessment are to: (1) quantify the risks posed by past tank releases to the groundwater if no interim corrective measures are implemented, and (2) determine to what degree implementation of selected interim corrective measures would decrease the risks posed by past tank releases. The assessments focus specifically on impacts to groundwater resources (i.e., the concentration of contaminants in groundwater) and long-term risk to human health (associated with groundwater use). The evaluations consider the extent of contamination presently within the vadose zone, contaminant movement through the vadose zone to the saturated zone (groundwater), contaminant movement in the groundwater to points of compliance, and the types of assumed human receptor activities at the points of compliance. The impact assessment results present several key evaluations for decision-maker input that may impact current operations and future decisions on tank retrieval and closure.

E.2.0 MODELING APPROACH

Both base case (existing tank farm conditions) and engineered alternatives for the interim corrective measures are considered. The focus for the contaminant transport modeling is chemicals (i.e., nitrate and chromium) and long-lived radionuclides (i.e., technetium-99) that are environmentally mobile. The postulated conceptual model utilizes the recently collected data on technetium-99 and other constituents from borehole 41-09-39, borehole 299-W23-19 near tank SX-115, and the MACTEC-ERS cesium-137 plume maps (Goodman 2000).

For simulations with barriers, it is assumed that an interim barrier is in place by the year 2010. It is also assumed that for all simulations, as part of tank farm closure, a closure barrier is in place by the year 2040. Placing a barrier is expected to significantly reduce infiltration of meteoric water and therefore arrival of contaminants at the water table. The modeling considers the estimated inventories of contaminants within the vadose zone and calculates the associated risk (i.e., exceeding the drinking water standards [40 CFR 141] at the compliance point). Inventory estimates are considered to be a critical factor in calculations, and uncertainties in inventories are considered. It is assumed that no tank leaks will occur in the future. It is also assumed that, as part of 'good housekeeping,' water-line leaks from existing piping will be addressed and resolved. However, as discussed later, as part of sensitivity analysis, simulations are run to evaluate long-term effects of water-line leaks in the vicinity of tank SX-115.

The umbrella structure of the tank and shedding of water are simulated. Sediments adjacent to the tanks attain elevated water contents and, while remaining unsaturated, they develop what is known as moisture-dependent anisotropy. Such effects are simulated in the model. Numerical results are obtained for compliance at the WMA boundary, 200 West fence boundary, exclusion boundary beyond the 200 Areas, and the Columbia River. Except for the 200 West fence boundary, these boundaries are based on DOE-RL (2000). Instead of the 200 West fence boundary, DOE-RL (2000) refers to the 200 Areas boundary. However, since the 200 Areas and the exclusion boundaries are relatively close the 200 Areas boundary is replaced by the 200 West fence boundary. Streamtube/analytical models are used to route computed contaminant concentrations at the water table to compliance points.

Two-dimensional cross-sectional models are used to model vadose zone flow and transport. Three representative (west-east) cross-sectional models for the S and SX tank farms (Figure E.1) are considered:

- Cross-section through tanks SX-107, SX-108, and SX-109
- Cross-section through tanks SX-113, SX-114, and S-115
- Cross-section through tanks S-104, S-105, and S-106.

Note that, in this appendix and elsewhere in the main text (Section 4.0), the three cross-sections are labeled in two ways. For example, the row containing tanks SX-107, SX-108, and SX-109 is often labeled as cross-section SX-DD'. Similarly, cross-section SX-FF' refers to the row containing tanks SX-113, SX-114, and SX-115 and cross-section S-CC' refers to the row containing tanks S-104, S-105, and S-106. Figures E.2 through E.4 show the three geologic cross-sections.

Figure E.1. Location Map of Single-Shell Tank WMA S-SX and Surrounding Facilities in the 200 West Area

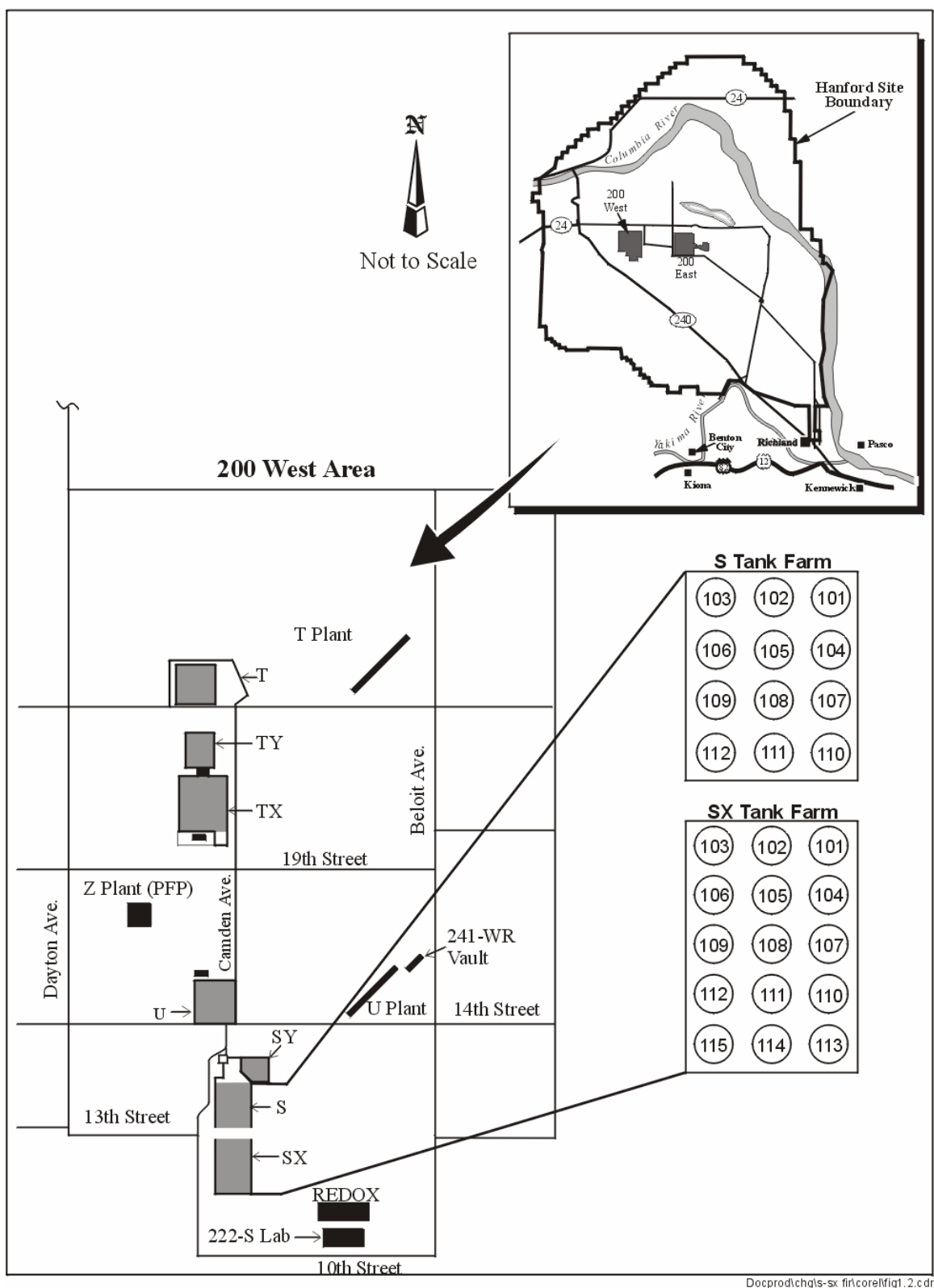


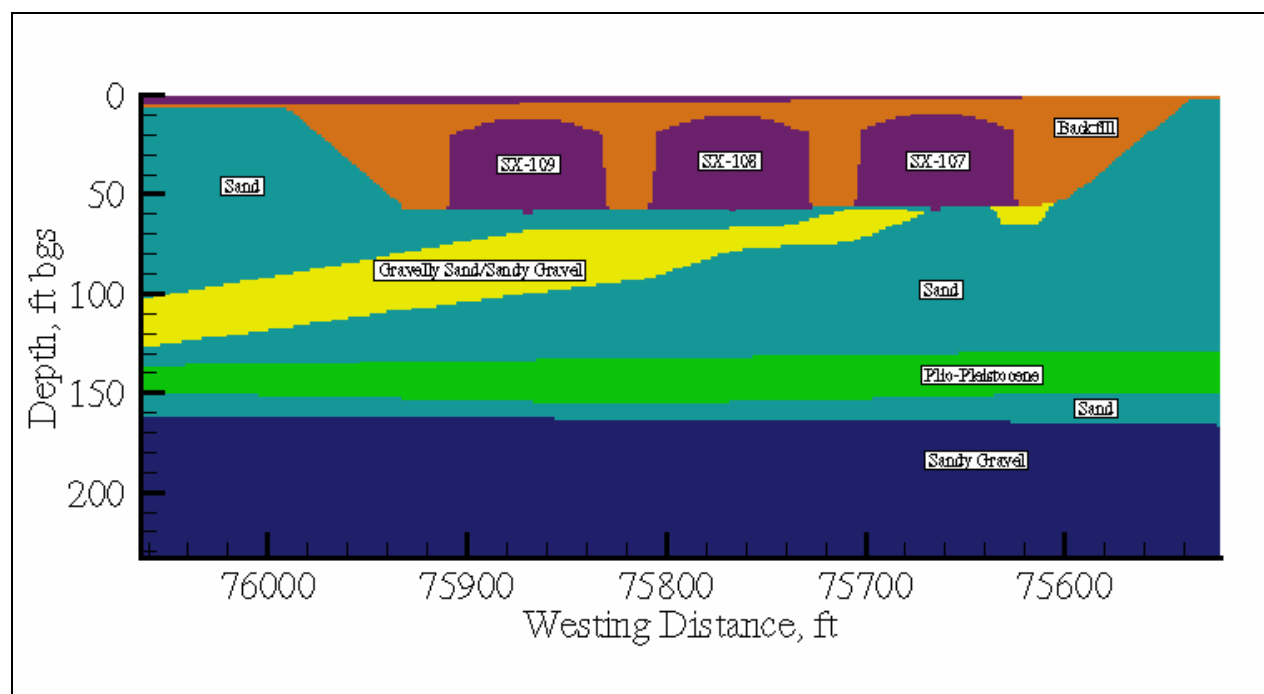
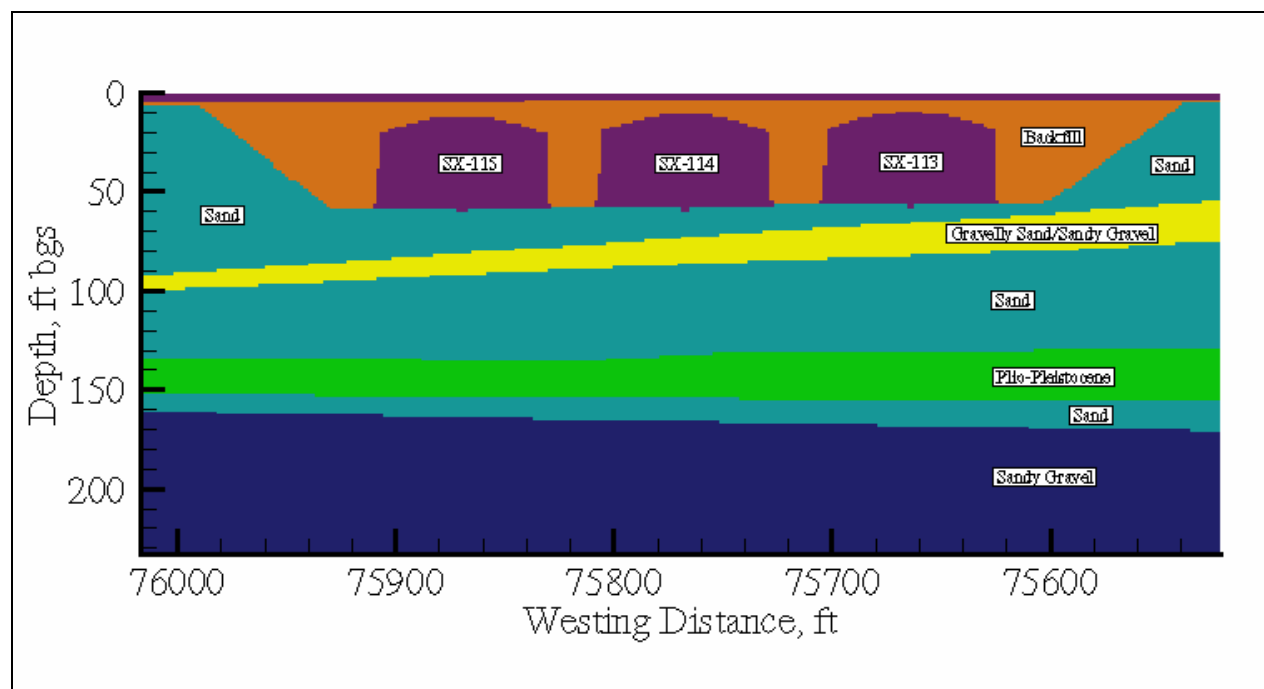
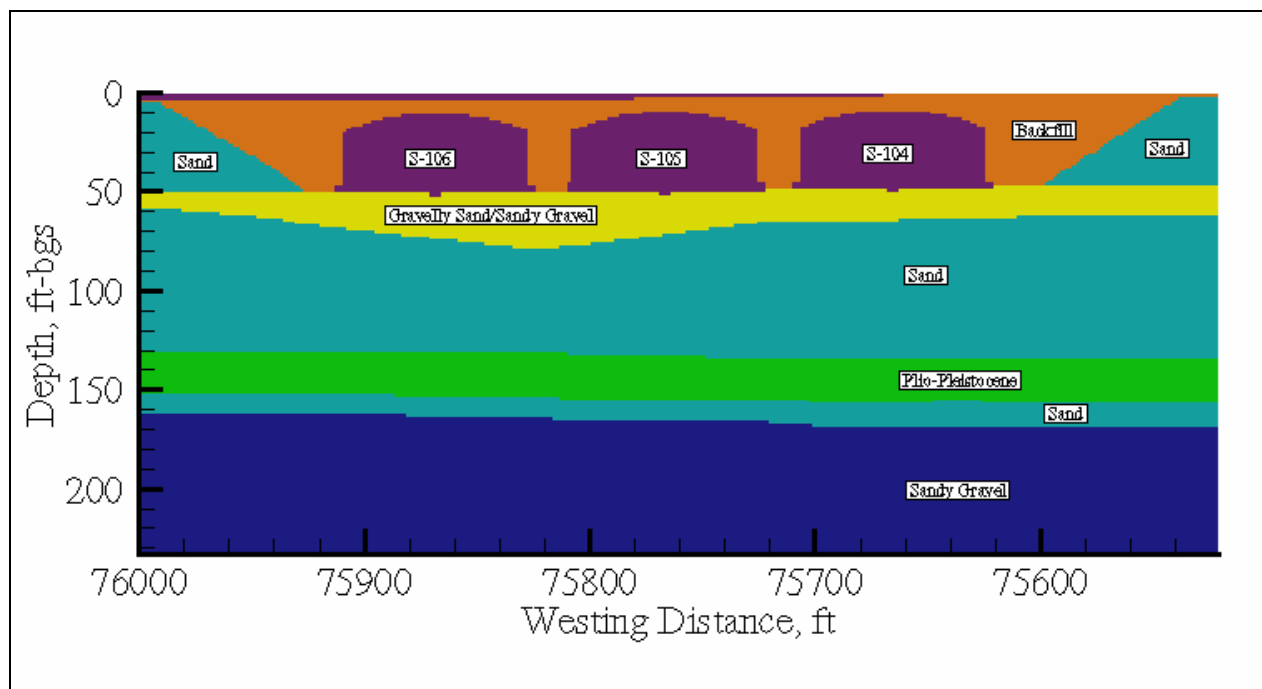
Figure E.2. Cross-Section SX-DD'**Figure E.3. Cross-Section SX-FF'**

Figure E.4. Cross-Section S-CC'

Simulation of flow and transport through each cross-section generates a breakthrough curve (BTC) at the water table. The temporal and spatial distribution for each of these BTCs is recognized and the principle of superposition is used to generate a composite BTC at the compliance boundary. An analytical/streamline approach is used to route the BTCs through the unconfined aquifer to the compliance boundary. The BTCs are converted into dose estimates using appropriate factors.

Fluid flow within the vadose zone is described by Richards' equation, whereas the contaminant transport is described by the conventional advective-dispersive transport equation with an equilibrium linear sorption coefficient (K_d) formulation. Detailed stratigraphic cross-sectional model data are based on information in *Subsurface Physical Conditions Description of the S-SX Waste Management Area* (Johnson et al. 1999), *Geology of the 241-S Tank Farm* (Price and Fecht 1976a), and *Geology of the 241-SX Tank Farm* (Price and Fecht 1976b). The model includes the effects of dipping strata. The enhanced spreading at the fine-grained/coarse-grained interfaces and the increased downdip movement of the plume along these interfaces are included in the model.

Data on laboratory measurements for moisture retention, particle-size distribution, saturated and unsaturated hydraulic conductivity, and bulk density for individual stratum are based on data on 200 East and 200 West Area soils (Khaleel et al. 2000). For each stratum defined by the stratigraphic cross-sectional model, the small-scale laboratory measurements are upscaled to obtain equivalent horizontal and vertical unsaturated hydraulic conductivities as a function of mean tension (Khaleel et al. 2000). Upscaling of unsaturated hydraulic conductivities ($K's$) leads to development of macroscopic anisotropies (as a function of mean tension) for each layer. An averaging of van Genuchten parameters (θ_r , θ_s , α , and n) (van Genuchten 1980) is used to define a moisture retention curve for each stratum.

In case multiple samples are not available for each stratum, data from other sites in the WMA S-SX vicinity are used. Attempts are made to use hydraulic properties that were obtained using both laboratory-measured moisture retention and unsaturated hydraulic conductivity. This is primarily to avoid extrapolating the unsaturated conductivities (van Genuchten 1980; Mualem 1976) to the dry end, based on saturated conductivity estimate (Khaleel et al. 1995). Also, to reflect field conditions, the laboratory data are corrected for the presence of any gravel fraction in the sediment samples (Khaleel and Relyea 1997).

As with flow modeling, each stratum is modeled with different transport parameters (i.e., bulk density, diffusivity, and dispersivity). As discussed earlier, contaminant mobility is quantified by sorption coefficients. A highly disturbed geochemical environment exists in the WMA S-SX vadose zone. The zones exist because chemistry of some leaked fluids radically differs from water and could change the soil water geochemical regime as migration occurs. The available database suggests that the most severe changes have occurred in soils underlying and near tanks SX-107, SX-108, and SX-109. While there is uncertainty about the sorption coefficient of cesium-137 and how it changes with concentration of competing ions, there is no doubt the sorption coefficient of technetium-99 is close to 0 mL/g in Hanford Site sediments. The low sorption coefficient coupled with a long half-life (2.03×10^5 years) allows technetium-99 to migrate over long distances in both the vadose zone and groundwater, posing a threat to groundwater quality for a long time.

Initial Conditions

Initial conditions are needed for moisture content (or pressure head) and contaminant concentration. For simulations not considering a barrier, initial conditions for pressure head (and moisture content) are established by allowing the vadose zone to equilibrate with an infiltration rate representative of natural infiltration for tank farm conditions. The data on infiltration rates with and without barriers are included in Section E.2.2.1. Initial conditions for contaminant concentration are provided as part of inventory estimates for cesium-137, technetium-99, nitrate, and chromium.

Model Setup and Boundary Conditions

A two-dimensional (west-east) vertical (x-z) slice of the flow domain is used for modeling flow and transport. The simulation domain extends horizontally to include the WMA S-SX boundaries and the water table, which is located about 65 m (213 ft) below ground surface. The geologic strata are assumed continuous but not of constant thickness. A variable grid spacing is used to model features such as the presence of clastic dikes between tanks. Sloped interfaces for geologic units are included based on information in Johnson et al. (1999), Price and Fecht (1976a), and Price and Fecht (1976b).

For flow modeling, Neumann boundary conditions are prescribed at the surface with the flux equal to the recharge rate estimate. For transport modeling, a zero flux boundary is prescribed at the surface for cesium-137, technetium-99, nitrate, and chromium. The western and eastern boundaries are assigned no-flux boundaries for both flow and transport. The water table boundary is prescribed by water table elevations and the unconfined aquifer hydraulic gradient. No-flux boundaries are used for the lower boundary.

To account for the residual effects of tank leaks, the variable density and viscosity of the leaked fluid are considered. The increased fluid density effects are expected to enhance the vertical mobility of both the fluid and the contaminant. The density effect can elongate the plume vertically and tends to decrease the lateral spreading caused by stratigraphic variations in material properties and moisture-dependent anisotropy.

Clastic dikes are included in the modeling as a sensitivity analysis. Clastic dikes occur in many locations in the 200 West Area and have been hypothesized as potential pathways for vertical transport that could explain the deep migration of contaminants at the SX tank farm. Preliminary data on clastic dike infilling materials are based on *Far-Field Hydrology Data Package for Immobilized Low-Activity Tank Waste Performance Assessment* (Khaleel 1999). Detailed inputs for various flow and transport parameters are presented later.

E.2.1 NUMERICAL CASES CONSIDERED

The following simulation runs (Cases 1 through 13) are considered for two-dimensional simulations. Note that Cases 1 through 4 consider a spatially uniform distribution of the inventory for the three cross-sections. Cases 5, 6, and 7 consider a nonuniform distribution of the same inventory. Case 7 considers a different location of the inventory within the two-dimensional cross-section. Cases 3 and 13 consider different volumes for water-line leaks, whereas Cases 9 through 11 consider varying estimates of natural recharge. Note that for Cases 3 and 13, the three-dimensional water-line leak was modeled as a point source of water spread over a circular area between two tanks. The circular leak area was translated for the two-dimensional simulations using a unit computational grid width and assuming that the center of the leak area was situated on the center line between tanks. Details are given in Section E.4.0. The simulations are run for a period of compliance of 1,000 years. Note that each of the 13 cases summarized below involves three cross-sectional runs.

- **Case 1: Base Case, No Action Alternative.** Flow and transport runs for cross-sections through tanks SX-107, SX-108, and SX-109; tanks SX-113, SX-114, and SX-115; and tanks S-104, S-105, and S-106 considering natural infiltration *only*, *no* water-line leak, *no* interim barrier, and a closure barrier by the year 2040.
- **Case 2: Barrier Alternative and No Water-Line Leak.** Flow and transport runs for cross-sections through tanks SX-107, SX-108, and SX-109; tanks SX-113, SX-114, and SX-115; and tanks S-104, S-105, and S-106 considering placement of an interim barrier by 2010; a closure barrier by 2040 (i.e., the interim barrier replaced by the closure barrier); and *no* water-line leak.
- **Case 3: No Barrier and 25,000 gal Water-Line Leak.** Flow and transport runs for cross-sections through tanks SX-107, SX-108, and SX-109; tanks SX-113, SX-114, and SX-115; and tanks S-104, S-105, and S-106 considering natural infiltration, water-line leak (25,000 gal) for tank SX-115 *only*, and *no* barrier until closure.
- **Case 4: No Interim Barrier and Clastic Dikes.** Flow and transport runs for cross-sections through tanks SX-107, SX-108, and SX-109; tanks SX-113, SX-114, and

SX-115; and tanks S-104, S-105, and S-106 considering natural infiltration, clastic dikes midway between tanks SX-108 and SX-109, and *no* interim barrier until closure.

- **Case 5: Nonuniform Inventory Distribution and No Barrier.** Flow and transport runs for cross-sections through tanks SX-107, SX-108, and SX-109; tanks SX-113, SX-114, and SX-115; and tanks S-104, S-105, and S-106 considering natural infiltration *only*; *no* water-line leak; *no* barrier until closure; and a higher distribution of inventory at a few locations (e.g., a few nodes, with a high concentration, either at the same depth or at different depths).
- **Case 6: Nonuniform Inventory Distribution and Barrier.** Flow and transport runs for cross-sections through tanks SX-107, SX-108, and SX-109; tanks SX-113, SX-114, and SX-115; and tanks S-104, S-105, and S-106 considering barrier infiltration (interim barrier replaced at closure); *no* water-line leak; and a higher distribution of inventory at a few locations (e.g., a few nodes, with a high concentration, either at the same depth or at different depths).
- **Case 7: Displaced-Nonuniform Inventory Distribution and No Barrier.** Flow and transport runs for cross-sections through tanks SX-107, SX-108, and SX-109; tanks SX-113, SX-114, and SX-115; and tanks S-104, S-105, and S-106 considering natural infiltration *only*, *no* water-line leak, *no* barrier until closure, and an inventory location close to the water table.
- **Case 8: Density and Viscosity Effects.** Flow and transport runs for cross-sections through tanks SX-107, SX-108, and SX-109; tanks SX-113, SX-114, and SX-115; and tanks S-104, S-105, and S-106 considering natural infiltration *only*, *no* water-line leak, enhanced density and viscosity, and *no* barrier until closure.
- **Case 9: Base Case with 50 mm/yr Meteoric Recharge.** Flow and transport runs for cross-sections through tanks SX-107, SX-108, and SX-109; tanks SX-113, SX-114, and SX-115; and tanks S-104, S-105, and S-106 considering natural infiltration (50 mm/yr) *only*, *no* water-line leak, *no* interim barrier, and a closure barrier by the year 2040.
- **Case 10: Base Case with 30 mm/yr Meteoric Recharge.** Flow and transport runs for cross-sections through tanks SX-107, SX-108, and SX-109; tanks SX-113, SX-114, and SX-115; and tanks S-104, S-105, S-106 considering natural infiltration (30 mm/yr) *only*, *no* water-line leak, *no* interim barrier, and a closure barrier by the year 2040.
- **Case 11: Base Case with 10 mm/yr Meteoric Recharge.** Flow and transport runs for cross-sections through tanks SX-107, SX-108, and SX-109; tanks SX-113, SX-114, and SX-115; and tanks S-104, S-105, S-106 considering natural infiltration (10 mm/yr) *only*, *no* water-line leak, *no* interim barrier, and a closure barrier by the year 2040.
- **Case 12: Alternate Inventory Distribution and No Barrier.** Flow and transport runs for cross-sections through tanks SX-107, SX-108, and SX-109; tanks SX-113, SX-114, and SX-115; and tanks S-104, S-105, and S-106 considering natural infiltration (100 mm/yr) *only*, *no* water-line leak, *no* interim barrier, a closure barrier by the year 2040, and an alternate inventory distribution.

- **Case 13: No Barrier and 200,000 gal Water-Line Leak.** Flow and transport runs for cross-sections through tanks SX-107, SX-108, and SX-109; tanks SX-113, SX-114, and SX-115; and tanks S-104, S-105, and S-106 considering natural infiltration (100 mm/yr), water-line leak (200,000 gal) for tank SX-115 *only*, and *no* barrier until closure.

In addition to the preceding two-dimensional simulations, a fully three-dimensional simulation (see Section E.4.14) is also considered. However, the risk calculations are all based on two-dimensional simulation results. The three-dimensional simulation is performed as a check on the two-dimensional analysis.

E.2.2 RECHARGE ESTIMATES AND VADOSE ZONE FLOW AND TRANSPORT PARAMETERS

Modeling inputs for recharge estimates and effective (upscaled) flow and transport parameters are presented in this section. The effective parameters are based on laboratory measurements of moisture retention, saturated and unsaturated hydraulic conductivity, and bulk density for sediment samples in the 200 Areas.

E.2.2.1 Recharge Estimates

The S and SX tank farm surfaces are covered with gravel to prevent vegetation growth and provide radiation shielding for site workers. Bare gravel surfaces, however, enhance net infiltration of meteoric water compared to undisturbed naturally-vegetated surfaces. Infiltration is further enhanced in the tank farms by the effect of percolating water being diverted by an impermeable, sloping surface of the tank domes. The basis for recharge estimates (Table E.1) for field investigation report modeling is presented in the main text (Section 3.1.2).

Table E.1. Timeline Estimates for Emplacement of Interim and Closure Barriers at the S and SX Tank Farms and Corresponding Recharge Estimates

Condition Simulated	Recharge Estimate (mm/yr)
No barrier [2000-2010]	100
Interim barrier [2010-2040]	0.5
Closure barrier (1 st 500 yrs) [2040-2540]	0.1
Degraded closure barrier (post 500 yrs) [2540-3000]	3.5

E.2.2.2 Vadose Zone Flow and Transport Parameters

This section provides effective (upscaled) values of flow and transport parameters for the vadose zone. Specific flow parameters include moisture retention and saturated and unsaturated hydraulic conductivity. Transport parameters include bulk density, diffusivity, sorption coefficients, and macrodispersivity. Details on deriving the effective (upscaled) parameters are addressed in *Modeling Data Package for S-SX Field Investigation Report (FIR)* (Khaleel et al. 2000).

Table E.2 lists composite, fitted van Genuchten-Mualem (van Genuchten 1980; van Genuchten et al. 1991) parameters for various strata at the S and SX tank farms. Again, note that the material type numbers noted in Table E.2 (and in Tables E.3, E.5, and E.6) are identical to those indicated in the modeling data package (Appendix B of Khaleel et al. 2000). Estimates for the equivalent horizontal and vertical hydraulic conductivities are presented in Section E.2.2.3.

Table E.2. Composite van Genuchten-Mualem Parameters for Various Strata at the S and SX Tank Farms

Strata/Material Type	Number of Samples	θ_s	θ_r	α (1/cm)	n	ℓ	Fitted K_s (cm/s)
Backfill (1)	10	0.1380	0.0100	0.0210	1.3740	0.5	5.60E-04
Sand (2)	12	0.3819	0.0443	0.0117	1.6162	0.5	9.88E-05
Gravelly sand/sandy gravel (3)	11	0.2126	0.0032	0.0141	1.3730	0.5	2.62E-04
Plio-Pleistocene (4)	4	0.4349	0.0665	0.0085	1.8512	0.5	2.40E-04
Sandy gravel (5)	10	0.1380	0.0100	0.0210	1.3740	0.5	5.60E-04

Source: Khaleel et al. (2000).

E.2.2.3 Stochastic Model for Macroscopic Anisotropy

Variable, tension-dependent anisotropy provides a framework for upscaling small-scale, laboratory measurements to the effective (upscaled) properties for the large-scale tank farm vadose zone. A stochastic model (Polmann 1990) is used to evaluate tension-dependent anisotropy for sediments at the WMA S-SX; details are in Appendix C of Khaleel et al. (2000). The following is a brief description of the variable anisotropy model used in the field investigation report modeling.

Yeh et al. (1985) analyze steady unsaturated flow through heterogeneous porous media using a stochastic model; parameters such as hydraulic conductivity are treated as random variables rather than as deterministic quantities. The Gardner (1958) relationship is used in Yeh et al. (1985) to describe unsaturated hydraulic conductivity (K) as a function of saturated hydraulic conductivity (K_s) and tension (ψ), that is,

$$K(\psi) = K_s \exp(-\beta\psi) \quad (\text{E.1})$$

where:

β = fitting parameter.

Equation E.1 can be written as

$$\ln K(\psi) = \ln K_s - \beta\psi \quad (\text{E.2})$$

Equation E.2 is referred to as the log-linear model, because $\ln K$ is linearly related to ψ through the constant slope β . However, such a constant slope is often inadequate in describing $\ln K(\psi)$ over ranges of tension of practical interest for field applications. As an alternative, the slope β can be approximated locally by straight lines over a fixed range of tension. The $\ln K_s$ in Equation E.2 can then be derived by extrapolating the local slopes back to zero tension.

Using a linear correlation model between the log-conductivity zero-tension intercept and β , Polmann (1990) presents a generalized model that accounts for the cross-correlation of the local soil property (i.e., $\ln K_s$ and β) residual fluctuations. Compared to uncorrelated $\ln K_s$ and β model, partial correlation of the properties is shown to have a significant impact on the magnitude of the effective parameters derived from the stochastic theory. The Polmann (1990) equations for deriving the effective parameters are as follows.

$$\begin{aligned} \langle \ln K \rangle &= \langle \ln K_s \rangle - A \langle \psi \rangle - \sigma_{\ln K_s}^2 \lambda [p - p^2 \langle \psi \rangle - \zeta^2 \langle \psi \rangle] / (1 + A\lambda) \\ \sigma_{\ln K}^2 &= \sigma_{\ln K_s}^2 [(1 - p \langle \psi \rangle)^2 + \zeta^2 \langle \psi \rangle^2] / (1 + A\lambda) \\ K_h^{eq} &= \exp[\langle \ln K \rangle + (\sigma_{\ln K}^2 / 2)] \\ K_v^{eq} &= \exp[\langle \ln K \rangle - (\sigma_{\ln K}^2 / 2)] \end{aligned} \quad (E.3)$$

where:

$$\begin{aligned} \sigma_{\ln K}^2 &= \text{variance of log unsaturated conductivity (which depends on mean tension)} \\ \langle \psi \rangle &= \text{mean tension} \\ \sigma_{\ln K_s}^2 &= \text{variance of } \ln K_s \\ \langle \ln K_s \rangle &= \text{mean of } \ln K_s \\ p &= \text{slope of the } \beta \text{ versus } \ln K_s \text{ regression line} \\ \zeta &= \sigma_\delta / \sigma_{\ln K_s} \\ \sigma_\delta &= \text{standard deviation of the residuals in the } \beta \text{ versus } \ln K_s \text{ regression} \\ A &= \text{mean slope, } \beta, \text{ for } \ln K_s \text{ vs. } \psi \\ \lambda &= \text{vertical correlation lengths for } \ln K_s \text{ (assumed to be same as that of } \beta) \\ K_h^{eq} &= \text{equivalent unsaturated horizontal conductivity} \\ K_v^{eq} &= \text{equivalent unsaturated vertical conductivity.} \end{aligned}$$

E.2.2.3.1 Macroscopic Anisotropy Parameters. Table E.3 lists the variable, macroscopic anisotropy parameter estimates for various strata at WMA S-SX. Details on derivation of the parameter estimates are included elsewhere (Appendix C of Khaleel et al. 2000).

**Table E.3. Macroscopic Anisotropy Parameters Based on Polmann (1990)
Equations for Various Strata at the S and SX Tank Farms**

Strata/Material Type	Number of Samples	$\langle \ln K_s \rangle$	$\sigma_{\ln K_s}^2$	p	ζ	λ (cm)	A
Backfill (1)	10	-15.76	3.56	-1.1E-4	1.84E-4	30	0.00371
Sand (2)	12	-14.6	1.50	-7.2E-4	6.55E-4	50	0.00620
Gravelly sand/sandy gravel (3)	11	-14.85	1.94	-2.6E-4	2.50E-4	30	0.00368
Plio-Pleistocene (4)	4	-10.43	1.01	2.4E-3	9.34E-4	50	0.0104
Sandy gravel (5)	10	-15.76	3.56	-1.1E-4	1.84E-4	30	0.00371

E.2.2.4 Clastic Dike Infilling Material Properties

Data on physical and hydraulic parameters are needed for clastic dike infilling materials to model their effects on flow and contaminant transport. Data on bulk density, particle-size distribution, moisture retention, saturated and unsaturated hydraulic conductivities for clastic dike infilling materials are included in Appendix C of Khaleel et al. (2000). Table E.4 provides the effective parameters.

Table E.4. Effective Hydraulic Parameters for Clastic Dike Infilling Materials

Material	θ_s (cm ³ /cm ³)	θ_r (cm ³ /cm ³)	α (1/cm)	n (-)	Saturated Hydraulic Conductivity (cm/s)
Clastic dike	0.4348	0.04675	0.07343	1.7115	1.20E-03

E.2.2.5 Enhanced Density and Viscosity Estimates

Numerical simulation cases in Section E.2.1 identify one run with enhanced density and viscosity estimates for the leaked fluid. The impact of fluid properties (density and viscosity) on contaminant migration is investigated by considering a fluid specific gravity of 1.4 (Ward et al. 1997).

E.2.2.6 Effective Transport Parameters

Effective transport parameter (bulk density, diffusivity, and dispersivity) estimates are presented in this section. Because of natural variability, the transport parameters are all spatially variable. The purpose is again, similar to the flow parameters, to evaluate the effect of such variability on the large-scale transport process.

E.2.2.6.1 Bulk Density and Sorption Coefficient. Both bulk density (ρ_b) and sorption coefficient estimates are needed to calculate retardation factors for different species. The effective, large-scale estimate for the product $[\rho_b K_d]$ is the average of the product of

small-scale laboratory measurements for bulk density and sorption coefficient (Gelhar 1993). Table E.5 provides the effective, large-scale estimates for cesium-137. The average ρ_b , $E[\rho_b]$ (Table E.5) estimates are based on data in Khaleel et al. (2000) for the five strata and clastic dike samples. The sorption coefficient estimates (Table E.5) for cesium-137 are based on *Data from Geochemical Data Package for the Immobilized Low-Activity Waste Performance Assessment* (Kaplan and Serne 1999) for undisturbed sediments. No other species are included, because the sorption coefficients for technetium-99, chromium, and nitrate are estimated to be zero. Calculations (Table E.5) for $E[\rho_b]$ and $E[\rho_b K_d]$ include correction for the gravel fraction.

Table E.5. Effective Parameter Estimates, $E[\rho_b K_d]$, for Cesium-137 for the Product of Bulk Density (g/cm^3) and K_d (cm^3/g) at WMA S-SX

Strata/Material Type	K_d	$E[\rho_b]$	$E[\rho_b K_d]$
Backfill (1)	500	1.94	971
Sand (2)	500	1.76	864
Gravelly sand/sandy gravel (3)	500	2.07	600
Plio-Pleistocene (4)	500	1.65	814
Sandy gravel (5)	500	2.13	488
Clastic dike	500	1.52	759

E.2.2.6.2 Diffusivity. It is assumed that the effective, large-scale diffusion coefficients for all strata at the S and SX tank farms are a function of volumetric moisture content, θ , and can be expressed using the empirical relation from “Permeability of Porous Solids” (Millington and Quirk 1961):

$$D_e(\theta) = D_0 \frac{\theta^{10/3}}{\theta_s^2} \quad (\text{E.4})$$

where:

$D_e(\theta)$ = effective diffusion coefficient of an ionic species

D_0 = effective diffusion coefficient for the same species in free water.

The molecular diffusion coefficient for all species in pore water is assumed to be $2.5 \times 10^{-5} \text{ cm}^2/\text{sec}$ (Kincaid et al. 1995).

E.2.2.6.3 Macrodispersivity. An extended review is provided in Appendix C of Khaleel et al. (2000) on the rationale for vadose zone macrodispersivity estimates. Macrodispersivity estimates are needed for both reactive (cesium-137) and non-reactive (i.e., technetium-99, chromium, and nitrate) species.

E.2.2.6.3.1 Macrodispersivity Estimates for Non-Reactive Species. Macrodispersivity estimates for non-reactive species (i.e., technetium-99, chromium, and nitrate) are listed in Table E.6. Details on the basis for the estimates are provided in Appendix C of

Khaleel et al. (2000). Macrodispersivities for clastic dike sediments are assumed to be same as those for the Plio-Pleistocene unit.

Table E.6. Non-Reactive Macrodispersivity Estimates for Various Strata at the S and SX Tank Farms

Strata/Material Type	A_L (cm)	A_T (cm)
Backfill (1)	~150	15
Sand (2)	~150	15
Gravelly sand (3)	~100	10
Plio-Pleistocene (4)	~50	5
Sandy gravel (5)	~150	15

E.2.2.6.3.2 Heterogeneous Sorption Enhanced Macrodispersivities for the Reactive Species. As expected, the net effect of sorption is to retard the velocity of the contaminant. Because sorption for specific contaminants may be a function of soil properties, as the soil properties experience spatial variability, the sorption also varies (Gelhar 1993; Talbott and Gelhar 1994).

Stochastic analysis results for macrodispersivity enhancement for the five strata are presented in Table C-7 of Khaleel et al. (2000) for the reactive species (i.e., cesium-137). Note that the unsaturated conductivities were evaluated at -100 cm via the fitted van Genuchten-Mualem relation. The macrodispersivity enhancement ranged from about 1.07 for backfill sediments to about 2.35 for Plio-Pleistocene unit sediments. No dispersivity enhancement is assumed for the clastic dike sediments.

E.2.3 GROUNDWATER FLOW AND TRANSPORT

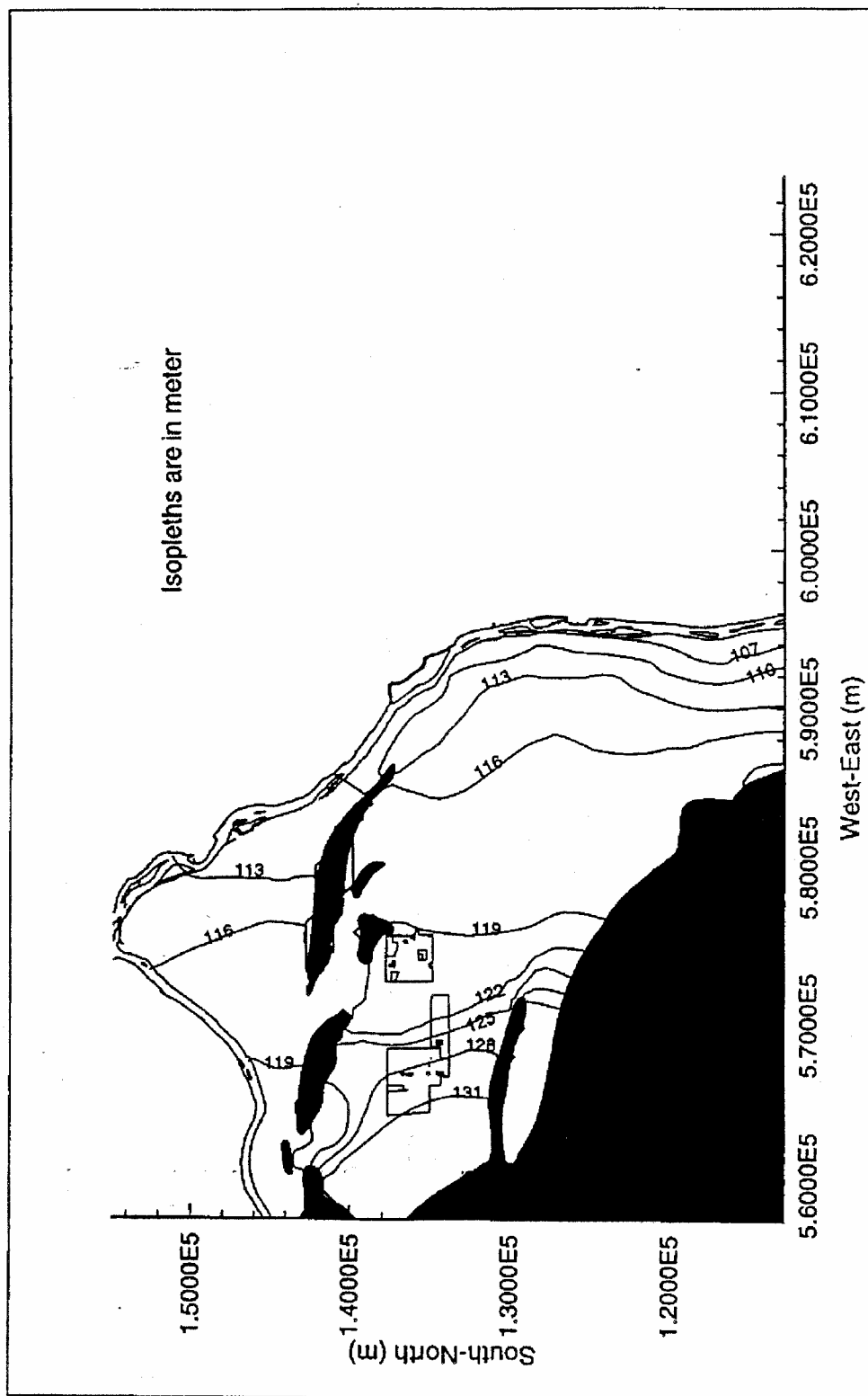
The preceding section provides vadose zone flow and transport parameters. This section includes flow and transport parameters for the unconfined aquifer. Also included are the unit dose conversion factors.

E.2.3.1 Flow and Transport Parameters

Instead of the Hanford Site-wide groundwater model, an analytical/streamtube approach is used to model groundwater flow and transport. However, as indicated in the following sections, flow and transport information needed for the analytical/streamtube model is based on the VAM3D Site-wide groundwater model (Law et al. 1996).

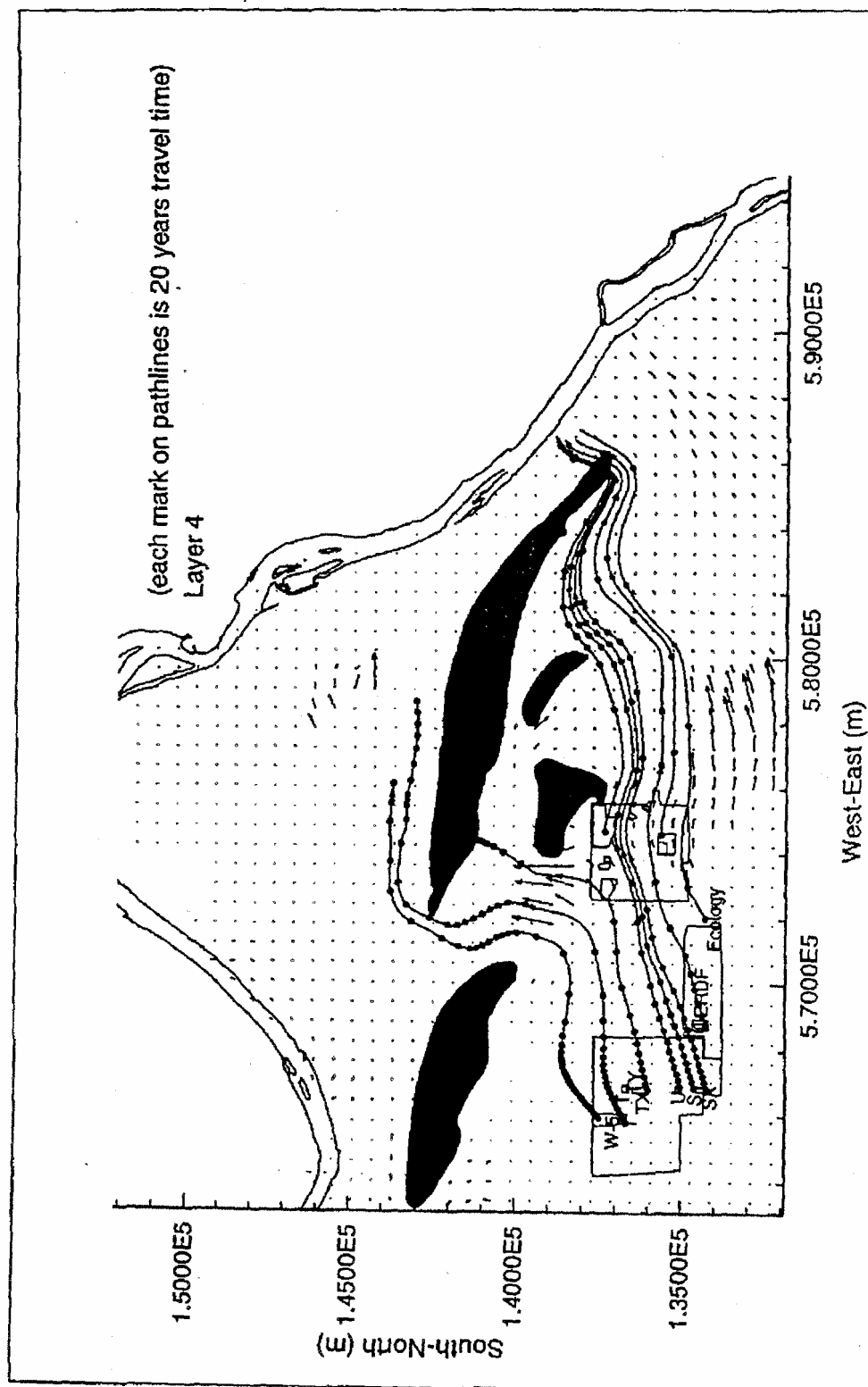
Figure E.5 shows the VAM3D-generated water table map at steady state, following simulation for 1,000 years. Figure E.5 can be used to generate streamlines/pathlines. Figure E.6 shows a streamline/pathline originating from the S and SX tank farms.

Figure E.5. VAM3D-Generated Steady State Hydraulic Head Distribution for the Hanford Site, Following Simulation for 1,000 Years



Source: Lu 1996.

Figure E.6. VAM3D-Generated Pathline Distribution at Steady State, Following Simulation for 1,000 Years



Source: Lu 1996.

Information on groundwater velocity distribution is needed for the analytical/streamtube model. Figure E.7 prescribes the material property numbers for various regions within the flow domain of the Site-wide model. Darcy's law, combined with Figure E.5 and Table E.7, which provides the saturated hydraulic conductivity and porosity for each material type, are used to perform necessary velocity calculations. Other parameters needed for groundwater transport modeling are listed in Table E.8. Note that a small vertical macrodispersivity of 10 mm is used based on the limited vertical mixing observed in stratified aquifers such as those in the 200 Areas (van der Kamp et al. 1994); the other macrodispersivities are the same as those used in the Site-wide model (Law et al. 1996).

E.2.3.2 Unit Dose Factors

Table E.9 lists the unit dose factors needed to convert cesium-137 and technetium-99 concentrations in groundwater to a radiation dose. Table E.9 is based on a drinking water consumption scenario of 730 L/yr.

E.2.4 CONTAMINANT INVENTORY

This section provides details on the basis for vadose zone contaminant inventory estimates and their distributions. Also included are details on how various inventory distributions are implemented in the numerical model.

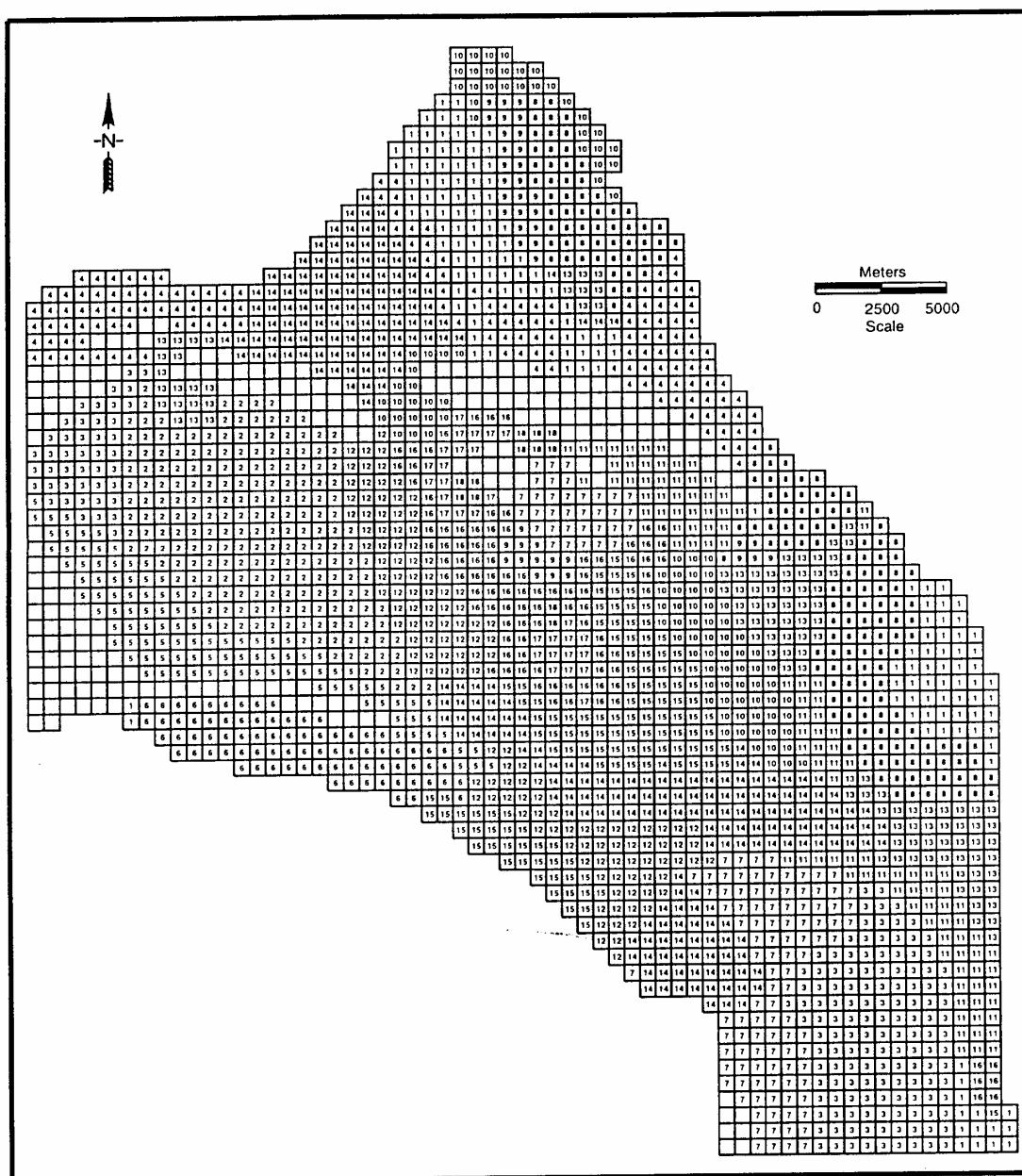
E.2.4.1 Basis for Inventory Estimates

Vadose zone inventory estimates for the four species (i.e., cesium-137, technetium-99, chromium, and nitrate) are primarily based on *Estimation of SX-Farm Vadose Zone Cs-137 Inventories from Geostatistical Analysis of Drywell and Soil Core Data* (Goodman 2000) and the recently collected borehole data. The Goodman (2000) estimates are used to assign inventory estimates for cesium-137 and the borehole data are used to assign estimates for the mobile species (i.e., technetium-99, chromium, and nitrate).

Goodman (2000) presents kriging analysis of cesium-137 inventory estimates in the vadose zone under the SX farm tanks based on measurements in the drywells, laterals, and borehole 41-09-39 soil cores. The details on inventory used in modeling are presented in *Inventory Estimates for Single-Shell Tank Leaks in S and SX Tank Farms* (Jones 2000) and Khaleel et al. (2000), and are included in Attachment E1. For technetium-99, chromium, and nitrate, the inventory estimates are scaled with respect to measured concentrations in boreholes. Note that data in Attachment E1 are decayed as of January 1, 2000. The decay coefficient for cesium-137 is 0.0231 yr^{-1} (i.e., half-life is 30 years).

Results of laboratory analyses of samples from borehole 41-09-39 provide the basis for inventory estimates for the mobile species under tanks SX-107, SX-108, and SX-109. Concentration measurements for samples from borehole 299-W23-19 southwest of tank SX-115 serve as the basis for estimates for the mobile species under tanks SX-113, SX-115, and S-104. Tank S-104 inventory estimates for cesium-137 are based on data from *Tank Summary Data Report for Tank S-104* (DOE-GJPO 1997). Tank SX-115 inventory estimates for cesium-137 are based on data from *Characterization of Subsurface Contamination in the SX Farm* (Raymond and Shdo 1966).

Figure E.7. Material Property Distribution for the Upper Three Elemental Layers for VAM3D Sitewide Groundwater Model



Source: Law et al. 1996.

**Table E.7. Hydraulic Properties for Various Material Types for
Site-wide VAM3D Groundwater Model**

Zone	K_{xx} (m/y)	K_{yy} (m/y)	K_{zz} (m/y)	S_s (1/m)	Porosity (Percent)
1	.800E+03	.800E+03	.800E+02	.100E-05	10
2	.190E+04	.190E+04	.190E+03	.100E-05	25
3	.500E+04	.500E+04	.500E+03	.100E-05	10
4	.650E+04	.650E+04	.650E+03	.100E-05	10
5	.140E+05	.140E+05	.140E+04	.100E-05	25
6	.720E+05	.720E+05	.720E+04	.100E-05	25
7	.260E+05	.260E+05	.260E+04	.100E-05	10
8	.300E+05	.300E+05	.300E+04	.100E-05	25
9	.430E+05	.430E+05	.430E+04	.100E-05	25
10	.055E+06	.055E+06	.055E+05	.100E-05	25
11	.770E+05	.770E+05	.770E+04	.100E-05	25
12	.899E+05	.899E+05	.899E+04	.100E-05	25
13	.140E+06	.140E+06	.140E+05	.100E-05	25
14	.300E+06	.300E+06	.300E+05	.100E-05	25
15	.750E+06	.750E+06	.750E+05	.100E-05	25
16	.113E+07	.113E+07	.113E+06	.100E-05	25
17	.183E+07	.183E+07	.183E+06	.100E-05	25
18	.213E+07	.213E+07	.213E+06	.100E-05	25

K_{xx} = Hydraulic conductivity in the North-South direction

K_{yy} = Hydraulic conductivity in the East-West direction

K_{zz} = Hydraulic conductivity in the vertical direction

S_s = Specific storage

m/y = meters per year

1/m = 1 per meter

Source: Law et al. (1996).

Table E.8. Transport Parameters for the Site-wide Groundwater Model

Parameter	Estimate
Longitudinal macrodispersivity, cm	3050
Lateral macrodispersivity, cm	305
Vertical macrodispersivity	10
Diffusion coefficient, cm ² /sec	2.5×10^{-5}
Cs-137 sorption coefficient, cm ³ /g	500
Cs-137 decay coefficient, 1/yr	0.0231

Table E.9. Unit Dose Factors for Cesium-137 and Technetium-99

Radionuclide	Dose factor*
Cs-137	0.0365
Tc-99	0.00107

*Units are mrem per pCi/L of concentration in the groundwater.

Source: Rittmann (1999).

E.2.4.2 Inventory Distributions

Because of significant uncertainties with inventory estimates, several distributions were considered. These included (1) uniform, (2) nonuniform, (3) displaced-nonuniform, and (4) an alternate distribution.

E.2.4.2.1 Uniform Distribution. For uniform distribution, the total inventory is assigned to discrete vadose zones, each having different values based on inventory variability. For uniform inventory distribution, the assigned inventory is uniformly distributed within each zone. For the cross-section with tanks SX-107, SX-108, and SX-109 (Figure E.1) the uniform distribution combines, by depth of each zone, the inventory noted in Attachment E1 under both tanks SX-108 and SX-109. The total inventory under both tanks is then distributed in the lateral direction across the two tanks (including the space between the tanks) by depths noted in Attachment E1. Note that both concentration and mass are honored in distributing the inventory in the lateral direction for each depth. For tank SX-107, the inventory is distributed across the diameter of that tank only.

For the cross-section with tanks SX-113, SX-114, and SX-115 (Figure E.1), the individual inventory for tanks SX-113 and SX-115 is distributed in the lateral direction across the tank diameter by depths noted in Attachment E1.

For the cross-section with tank S-104 (Figure E.1), the inventory is distributed uniformly in the lateral direction across the tank diameter by depths noted in Attachment E1.

E.2.4.2.2 Nonuniform Distribution. For nonuniform distribution, the distribution of inventory, by depth, is maintained. However, the inventory within each zone in the lateral direction is nonuniformly distributed but maintains the same mass of inventory as in the uniform distribution. The nonuniform inventory distribution cases are run *only* for the three mobile species.

For the cross-section with tanks SX-107, SX-108, and SX-109, two nonuniform distributions are generated; one for tanks SX-109 and SX-108 and the other for tank SX-107. For tanks SX-109 and SX-108, the nonuniform distribution combines, by depth, the inventory noted in Attachment E1 for tanks SX-109 and SX-108. The total inventory for both tanks is distributed in the lateral direction within the space between tanks SX-109 and SX-108 by depths noted in Attachment E1. For tank SX-107, the total inventory for each depth is distributed in the lateral direction within one-half the space *only* between tanks SX-107 and SX-108, beginning on the western edge of tank SX-107.

For the cross-section with tanks SX-113, SX-114, and SX-115, two nonuniform distributions are generated; one for tank SX-113 and the other for tank SX-115. For tank SX-113, the inventory for each depth is distributed in the lateral direction within one-half the space *only* between tanks SX-113 and SX-114, beginning on the western edge of tank SX-113. Similarly, for tank SX-115 the inventory for each depth is distributed in the lateral direction within one-half the space *only* between tanks SX-114 and SX-115, beginning on the eastern edge of tank SX-115.

For the cross-section with tank S-104, the inventory is distributed in the lateral direction within one-half the space *only* between tanks S-104 and S-105, beginning on the western edge of tank S-104.

E.2.4.2.3 Displaced-Nonuniform Distribution. To examine sensitivity (for mobile species only) relative to depth, a run considers location of the inventory close to the water table. A depth translation of the inventory data in Attachment E1 is used for the *nonuniform* distribution of the inventory for the three mobile species. The peak inventories, as noted in Attachment E1, are positioned within the Ringold Formation at about 50.3 m (165 ft) below ground surface; all other inventory locations are relative to this peak location.

E.2.4.2.4 Alternate Distribution. To further evaluate uncertainty in the lateral extent of the inventory, an alternate distribution was considered. The alternate distribution uses the tank diameters to define the radial extent of the contaminants.

E.2.4.3 Inventory Assignment

This section presents details on how the Attachment E1 inventory estimates were implemented numerically in STOMP (White and Oostrom 2000a, 2000b) calculations. As discussed in Section E.2.4.2, four different inventory distributions were investigated: uniform, nonuniform, displaced-nonuniform, and an alternate. Inventory distributions were one of two types: variable diameter or fixed diameter. Variable-diameter distributions honored both the concentration and total solute mass reported for a depth. In contrast, fixed-diameter distributions only honored the total solute mass reported for a depth. The uniform distribution was of the variable-diameter type, whereas the nonuniform, displaced-nonuniform, and alternate were fixed-diameter type distributions.

The uniform distribution most closely represented the inventory distributions (Attachment E1) and comprised of a series of concentric stacked disks. In the uniform distribution, the solute concentration within each disk equaled the Attachment E1 value, and the disk diameter was sized to honor the total solute mass for a particular depth. Therefore, the uniform distribution consisted of a series of concentric disks of varying concentration and diameter with depth. The nonuniform distribution comprised of a series of concentric stacked disks of equal diameter. This distribution honored the total solute mass reported in Attachment E1 for the depth, but altered the concentration according to the disk diameter. As the nonuniform distributions were used to investigate concentrating solute mass within the high flux regions between tanks, solute concentrations were generally higher than those reported Attachment E1. The displaced distribution was similar to the nonuniform distribution but displaced toward the water table. The alternate distribution was a fixed-diameter distribution that used the tank diameters to define the radial extent of solute. The algorithms used to develop variable-diameter and fixed diameter distributions differ and will be described in the sections that follow.

E.2.4.3.1 Variable-Diameter Distribution. The variable-diameter distribution honors both the concentration values and inventory mass at each depth by varying the distribution area as a function of depth. The first step in creating a variable-diameter distribution was to vertically interpolate Attachment E1 values on to the computational grid. The concentration and total solute mass are reported (Attachment E1) at discrete depths or in depth bins for each

combination of tank (i.e., S-104, SX-107, SX-108, SX-109, SX-113, and SX-115) and solute species (i.e., cesium-137, technetium-99, nitrate, and chromium). The cesium-137 data are reported in contiguous depth bins of 9.84 ft for all 6 tanks. The technetium-99, nitrate, and chromium data are reported in disjointed depth bins of 1 ft for tanks SX-107, SX-108, and SX-109 and at discrete depths for tanks S-104, SX-113, and SX-115. Prior to translating to the computational grid, the discrete data were converted into contiguous binned data by using node-centered discretization (i.e., each discrete depth was converted to a depth bin with the discrete depth centered in depth bin). This discretization yielded depth bins that varied in height with elevation.

After converting those data reported as discrete depths to depth bins, the solute concentrations and inventory integrals were translated to the computational grid using an overlapping approach for each combination of tank and solute specie. The computational grids used vertical spacings of 0.4572 m (1.5 ft), compared with the inventory depth bins that varied in height from 0.1524 m (0.5 ft) to 3.7338 m (12.25 ft). For these sets of dimensions, three domain overlapping conditions occurred:

- Computational grid totally within the inventory depth bin
- Computational grid partially within the inventory depth bin
- Depth bin totally within the computational grid.

For the first two conditions, a fraction of the inventory in the depth bin was assigned to the grid horizon based on the fraction of overlap. For example, if a 0.4572 m (1.5 ft) grid cell was completely enclosed by a 1.242 m (4.075 ft) depth bin, then 36.81% of the inventory integral would be located in the grid horizon. For the third condition the entire inventory integral for the depth bin would be located in the grid horizon. The overlapping approach, described above, distributes the inventory vertically across the computational domain according to Attachment E1 data and exactly preserves the total inventory for each tank and specie combination.

The horizontal distribution of inventory depended on whether the inventory was variable- or fixed-diameter type. As discussed earlier, the variable-diameter distribution honored both the inventory concentration and total mass reported in Attachment E1, whereas the fixed-diameter distribution only honored the total mass and computed the concentration needed to distribute that inventory mass over a declared region (e.g., the region between two tanks).

The variable-diameter inventory distribution honored both the inventory concentration and total mass at each grid horizon by spreading the inventory over horizon-dependent surface area. When developed the variable-diameter distribution resembles a series of stacked disks of varying diameters, which when translated to two-dimensions resulted in a series of stacked rectangles of varying width but having the same height as in the two-dimensional cross-section.

Note that the inventory concentration was specified as sediment concentrations (e.g., pCi/g) and not as aqueous concentrations. The first step in computing a variable-diameter distribution was to convert the inventory concentration and integral into a surface area, according to Equation E.5.

$$A_{horz}^{3D} = \frac{I_{horz}^{3D}}{C_{horz} z_{horz} \bar{\rho}_b^{3D}{}_{horz}} \quad (E.5)$$

where:

A_{horz}^{3D} = surface area (m²) for the grid horizon (three-dimensional domain)

$\bar{\rho}_b^{3D}{}_{horz}$ = average soil bulk density (kg/m³) for the grid horizon (three-dimensional domain)

I_{horz}^{3D} = total solute mass (Ci or µg) for the grid horizon (three-dimensional domain)

C_{horz} = solute concentration for the grid horizon (Ci/kg soil or µg/kg soil)

z_{horz} = height of the grid horizon (m).

The surface area (three-dimensional domain) was converted to a surface area per unit width for the grid horizon (two-dimensional cross-section) according to Equation E.6.

$$A_{horz}^{2D} = \sqrt{\frac{4 A_{horz}^{3D}}{\pi}} \quad (E.6)$$

where:

A_{horz}^{2D} = surface area per unit width (m²/m) for the grid horizon (two-dimensional cross-section).

Note that ‘per unit width’ appears because the numerical simulations are based on two-dimensional cross-sectional models.

Assuming that the average soil bulk density for the grid horizon (three-dimensional domain) is equal to that for the two-dimensional cross-section, then the total inventory mass per unit width is computed according to Equation E.7.

$$I_{horz}^{2D} = A_{horz}^{2D} C_{horz} z_{horz} \bar{\rho}_b^{2D}{}_{horz} \quad (E.7)$$

where:

I_{horz}^{2D} = solute inventory per unit width (Ci/m or µg/m) for the grid horizon (two-dimensional cross-section)

$\bar{\rho}_b^{2D}{}_{horz}$ = average soil bulk density (kg/m³) for the grid horizon (two-dimensional cross-section).

To compute number of grid cells (nodes) over which the solute was distributed, the product of the solute concentration for the grid horizon was multiplied by the node length, height, and bulk density and integrated outward from the grid cell that contains the distribution centroid. For each grid horizon, the inventory was distributed over an odd number of grid cells centered on the distribution centroid (e.g., tank centroid). The solute concentration on the two outer grid cells

was adjusted to yield an integrated inventory for the grid horizon that honors the grid-horizon total mass described above. This scheme is expressed mathematically as shown in Equation E.8.

$$I_{horz}^{2D} = \sum_{i=2}^{n-1} C_{horz} \Delta x^i \Delta z^i \rho_b^i + \hat{C} \left[\left(\Delta x^1 \Delta z^1 \rho_b^1 \right) + \left(\Delta x^n \Delta z^n \rho_b^n \right) \right] \quad (E.8)$$

where:

n = odd number of node indices centered around the distribution centroid

Δx = node length (m)

Δz^i = node height (m)

ρ_b^i = node bulk density (kg/m³)

\hat{C} = solute concentration assigned to the two outer most nodes.

The inventory distribution procedure described above worked for cases where the average soil bulk density was known over the distribution area. Because of the heterogeneous nature of the sediments, the average soil bulk density was unknown. Therefore, the actual calculation procedure followed the modified form expressed by Equations E.9 through E.12.

$$\tilde{A}_{horz}^{3D} = \frac{I_{horz}^{3D}}{C_{horz} z_{horz}} \quad (E.9)$$

$$\tilde{A}_{horz}^{2D} = \sqrt{\frac{4 \tilde{A}_{horz}^{3D}}{\pi}} \quad (E.10)$$

$$\tilde{I}_{horz}^{2D} = \tilde{A}_{horz}^{2D} C_{horz} z_{horz} \quad (E.11)$$

$$\tilde{I}_{horz}^{2D} = \sum_{i=2}^{n-1} C_{horz} \Delta x^i \Delta z^i \sqrt{\rho_b^i} + \hat{C} \left[\left(\Delta x^1 \Delta z^1 \sqrt{\rho_b^1} \right) + \left(\Delta x^n \Delta z^n \sqrt{\rho_b^n} \right) \right] \quad (E.12)$$

where:

\tilde{A}_{horz}^{3D} = surface area per unit bulk density (m²/[kg/m³]) for the grid horizon (three-dimensional domain)

\tilde{A}_{horz}^{2D} = surface area per unit width per unit square root bulk density (m²/m (kg/m³)^{1/2}) for the grid horizon (two-dimensional cross-section)

\tilde{I}_{horz}^{2D} = solute inventory per unit width per unit square root bulk density (Ci/m (kg/m³)^{1/2} or µg/m (kg/m³)^{1/2}) for the grid horizon (two-dimensional cross-section).

E.2.4.3.2 Variable-Diameter Distribution. The fixed-diameter distribution only honors the Attachment E1 inventory total mass at each depth using a declared distribution area. Solute

concentration is computed according to the inventory total mass and distribution area. As with the variable-diameter distribution, the first step in computing the fixed-diameter distribution was to vertically interpolate the Attachment E1 total masses on to the computational grid.

This interpolation procedure was identical to that for the variable-diameter distribution.

The horizontal distribution of inventory was based on the user declared distribution surface area (i.e., radius for a circular distribution) and the inventory total mass for the depth bin.

The concentration within this disk was then computed according to Equation E.13.

$$C_{horz} = \frac{I_{horz}^{3D}}{A_{horz}^{3D} z_{horz} \bar{\rho}_b^{3D}} \quad (E.13)$$

where:

A_{horz}^{3D} = surface area (m²) for the grid horizon (three-dimensional domain)

$\bar{\rho}_b^{3D}$ = average soil bulk density (kg/m³) for the grid horizon (three-dimensional domain)

I_{horz}^{3D} = solute inventory (Ci or µg) for the grid horizon (three-dimensional domain)

C_{horz} = solute concentration for the grid horizon (Ci/kg soil or µg/kg soil)

z_{horz} = height of the grid horizon (m).

To determine the number of grid cells over which the inventory was distributed the three-dimensional surface area was converted to a surface area per unit width, according to Equation E.14.

$$A_{horz}^{2D} = \sqrt{\frac{4 A_{horz}^{3D}}{\pi}} \quad (E.14)$$

where:

A_{horz}^{2D} = surface area per unit width (m²/m) for the grid horizon (two-dimensional cross-section).

For each grid horizon, the inventory was distributed over an odd number of grid cells centered on the distribution centroid (e.g., tank centroid) with a length equal to the surface area per unit width. The solute concentrations on the two outer grid cells were adjusted honor the inventory total mass. This scheme is expressed mathematically as shown in Equation E.15.

$$\hat{C} = \frac{I_{horz}^{2D} - \sum_{i=2}^{n-1} C_{horz} \Delta x^i \Delta z^i \rho_b^i}{\left[(\Delta x^1 \Delta z^1 \rho_b^1) + (\Delta x^n \Delta z^n \rho_b^n) \right]} \quad (E.15)$$

where:

n = odd number of node indices centered around the distribution centroid

Δx = node length (m)

Δz^i = node height (m)

ρ_b^i = node bulk density (kg/m³)

\hat{C} = solute concentration assigned to the two outer-most nodes.

E.2.4.3.3 Inventory Distribution Maps. Color-scaled images of the initial inventories, expressed as aqueous concentration for the twelve combinations of solute specie and cross-section, are shown for the uniform distribution in Attachment E2, Figures E2.1 through E2.12, for the nonuniform distribution in Figures E2.13 through E2.24, and for the translated-nonuniform distribution in Figures E2.25 through E2.36, and for the alternate distribution in Figures E2.37 through E2.48. The relationship between initial inventory distribution and simulation cases is shown in Table E.10.

Table E.10. Initial Inventory Distribution Schedule

Simulation Case	Inventory Distribution	Figures*
1	Uniform	E2.1 through E2.12
2	Uniform	E2.1 through E2.12
3	Uniform	E2.1 through E2.12
4	Uniform	E2.1 through E2.12
5	Nonuniform	E2.13 through E2.24
6	Nonuniform	E2.13 through E2.24
7	Displaced nonuniform	E2.25 through E2.36
8	Uniform	E2.1 through E2.12
9	Uniform	E2.1 through E2.12
10	Uniform	E2.1 through E2.12
11	Uniform	E2.1 through E2.12
12	Alternate	E2.37 through E2.48
13	Uniform	E2.1 through E2.12

*All figures are located in Attachment E2.

Specie inventories provided in the modeling data package were expressed in soil concentration (e.g., µg/g soil, pCi/g soil). These concentrations were converted to aqueous-phase concentrations based on the soil bulk density (i.e., from particle density and porosity) and the initial saturation, according to Equation E.16.

$$C_\ell = \frac{C_s \rho_s (1 - n_T) y_\ell}{s_\ell n_D} \quad (\text{E.16})$$

where:

C_ℓ = aqueous-phase concentration

C_s = soil concentration

ρ_s = soil particle density

n_T = total porosity

y_ℓ = equilibrium fraction of solute in the aqueous phase

s_ℓ = aqueous-phase saturation

n_D = diffusive porosity.

Except for density-dependent Case 8 run, the nitrate solute specie was considered a passive scalar for all simulations; therefore, aqueous-phase properties were independent of its concentration and no precipitation of the solute was considered.

E.3.0 HUMAN HEALTH RISK AND DOSE ESTIMATION APPROACH

This section presents the approach used to estimate human health risk (risk) and dose associated with exposure to contaminants of concern from past leaks and releases from WMA S-SX.

Risk is used herein to refer to the following:

- Incremental lifetime cancer risk (ILCR), which can occur from exposure to carcinogenic chemicals and radionuclides
- Hazard index, which is a measure of the potential for toxic health effects from exposure to noncarcinogenic chemicals.

Dose is the measure of radioactivity potentially received in a human body.

The interim measures under consideration for WMA S-SX address mitigation of groundwater impacts. The exposure pathways for this risk assessment therefore are based on the groundwater exposure medium. The exposure scenarios used for this assessment are as follows:

- Industrial
- Residential
- Industrial worker
- Residential farmer
- Recreational shoreline user.

Risk associated with the use of groundwater from a hypothetical water supply well was estimated at several downgradient points of compliance over a 1,000-year timeframe. Groundwater contaminant concentration estimates were based on the results of the contaminant transport analysis presented in Sections E.4.0 and E.5.0.

The risk assessment for this WMA S-SX field investigation report is qualitative at this stage in the corrective action process even though substantial site-specific data have been generated. Qualitative WMA risk evaluations have been performed at the Hanford Site using historical process and characterization data (DOE-RL 1995c; DOE-RL 1996). These qualitative risk evaluations have been used to initially evaluate the applicability and relative effectiveness of interim measures (e.g., eliminate leaking water lines and replace well caps). The risk assessment presented herein also relies on historical process and characterization data but is supplemented with additional site-specific data collected under the *Resource Conservation and Recovery Act of 1976* corrective action program as described in Appendices A and B. The results of this risk assessment are used to support evaluation of potential interim measures or interim corrective measures and to determine the need for additional WMA-specific characterization data.

Procedures for the approach and assumptions necessary to calculate human health risk are described in the following:

- “The Model Toxics Control Act Cleanup Regulation” (WAC 173-340), which implements “Model Toxics Control Act” (MTCA) requirements

- *Hanford Site Risk Assessment Methodology* (DOE-RL 1995b; HSRAM), which is the risk assessment methodology that the U.S. Department of Energy (DOE), Washington State Department of Ecology (Ecology), and the U.S. Environmental Protection Agency (EPA) have agreed to use to support Hanford Site cleanup decisions.

The WAC 173-340 implementing regulations define exposure scenarios and input parameters for two types of site uses: unrestricted (MTCA Method B) and industrial (MTCA Method C). Both the Method B and C exposure scenarios include potential consumption of groundwater. The Method B exposure scenario essentially assumes residential use; the scenario has been used in risk assessments of the Hanford Site 100 Areas to represent unrestricted land use (DOE-RL 1995a). The Method C exposure scenario has not been applied for site-specific decisions at the Hanford Site.

Under MTCA, risk assessment requirements for nonradioactive contaminants stipulate that carcinogenic risks shall be less than 10^{-6} (10^{-5} for multiple contaminants) for Method B and 10^{-5} for Method C. Also, concentrations of individual noncarcinogenic contaminants that pose acute or chronic toxic effects to human health shall not exceed a hazard quotient of 1.0. The MTCA risk criteria apply only to nonradioactive contaminants. The EPA guidance indicates that action is generally warranted when the cumulative carcinogenic risk is greater than 10^{-4} or the cumulative noncarcinogenic hazard index exceeds 1.0. Carcinogenic risks below 10^{-6} or hazard indices less than 1.0 are regarded as ‘points of departure’ below which no action is required. DOE orders require that groundwater protection standards be consistent with federal and Washington State requirements (i.e., EPA and Ecology requirements).

E.3.1 RECEPTOR SCENARIO RATIONALE

Current land use planning assumptions are documented in *Final Hanford Comprehensive Land-Use Plan Environmental Impact Statement* (DOE 1999), which provides an evaluation of several land uses for the Hanford Site for the next 50 years. That environmental impact statement and associated “Hanford Comprehensive Land-Use Plan Environmental Impact Statement (HCP EIS), Hanford Site, Richland, Washington; Record of Decision (ROD)” (64 FR 61615) identify ‘industrial-exclusive use’ as the planned use for the 200 Areas Central Plateau, an area that encompasses the 200 East and 200 West Areas. Ecology is evaluating how the DOE land-use planning efforts fit within the Ecology cleanup framework. Ecology has not yet agreed to an industrial use scenario. Therefore, multiple exposure scenarios are considered in the WMA S-SX risk assessment to account for the uncertainty of long-term Hanford Site land use.

As shown in *Phase I RCRA Facility Investigation/Corrective Measures Study Work Plan for Single-Shell Tank Waste Management Areas* (DOE-RL 2000), DOE and Ecology have agreed to use MTCA Methods B and C in the corrective action program. MTCA Methods B and C risks are calculated based on equations and parameters specified in the MTCA protocol for establishing groundwater cleanup levels (WAC 173-340-720). Risk is calculated for the residential farmer, industrial worker, and recreational shoreline user exposure scenarios based on the HSRAM. Estimates of risk based on the three HSRAM exposure scenarios are provided in this assessment to allow for comparison to risks cited in *Tank Waste Remediation System, Hanford Site, Richland, Washington, Final Environmental Impact Statement* (DOE and

Ecology 1996; TWRS EIS) and *Retrieval Performance Evaluation Methodology for the AX Tank Farm* (DOE-RL 1999b). Risk calculations for the three HSRAM-based scenarios use groundwater pathway unit risk factors adapted without modification directly from the TWRS EIS.

E.3.1.1 Residential Exposure Scenario (MTCA Method B)

The MTCA cleanup standards are applicable only to nonradioactive constituents. Under the Method B groundwater cleanup level protocol, exposure to hazardous and carcinogenic chemicals is based solely on ingestion of drinking water (with an inhalation correction factor used for volatile chemicals). Method B exposures for noncarcinogenic health effects are based on a drinking water intake rate of 1 L/day (0.2 gal/day) and an average body weight of 16 kg (35 lb) (WAC 173-340-720(3)(a)(ii)(A)). Method B exposures for carcinogenic health effects are based on a drinking water intake rate of 2 L/day (0.5 gal/day), an average body weight of 70 kg (150 lb), an exposure duration of 30 years, and a lifetime of 75 years (WAC 173-340-720(3)(a)(ii)(B)). Oral reference doses (mg/kg-day) and oral slope factors (kg-day/mg) developed by the EPA are applied to convert the exposures to the health effect appropriate for each constituent.

Four hypothetical receptor locations identified by DOE and Ecology (DOE-RL 2000) as the points of compliance for which potential risk will be calculated are as follows:

- Downgradient WMA boundary
- Downgradient boundary of the 200 West Area
- Downgradient boundary of the 200 Area exclusion zone as defined by the Hanford Future Site Uses Working Group (FSUWG 1992)
- Downgradient at the Columbia River shoreline.

The Method B risk is calculated at all four points of compliance. Note that for the WMA S-SX boundary, risk is calculated at three separate locations corresponding to the three cross-sections (S-CC', SX-DD', SX-FF') considered in the contaminant transport analysis.

E.3.1.2 Industrial Exposure Scenario (MTCA Method C)

As in the MTCA Method B residential exposure scenario, the MTCA Method C industrial exposure scenario is applicable only to nonradioactive constituents. Under the Method C groundwater cleanup level protocol, exposure to hazardous and carcinogenic chemicals is based solely on ingestion of drinking water (with an inhalation correction factor used for volatile chemicals). Method C exposures for noncarcinogenic health effects are based on a drinking water intake rate of 2 L/day (0.5 gal/day) and an average body weight of 70 kg (150 lb) (WAC 173-340-720(4)(b)(ii)(A)). Method C exposures for carcinogenic health effects are based on a drinking water intake rate of 2 L/day (0.5 gal/day), an average body weight of 70 kg (150 lb), an exposure duration of 30 years, and a lifetime of 75 years (WAC 173-340-720(4)(b)(ii)(B)). Oral reference doses (mg/kg-day) and oral slope factors

(kg-day/mg) developed by the EPA are applied to convert the exposures to the health effect appropriate for each constituent.

Method C risk is calculated for the same four points of compliance as defined for the Method B calculations in Section E.3.1.1.

E.3.1.3 Industrial Worker Scenario

An industrial worker scenario consistent with the scenario described in HSRAM is used to represent potential exposure to workers in a commercial or industrial setting. The receptors are adult employees assumed to work at a location for 20 years. A body weight of 70 kg (150 lb) and a lifetime of 70 years are assumed. The scenario involves mainly indoor activities, although outdoor activities (e.g., soil contact) also are included. The groundwater exposure pathways for this scenario include drinking water ingestion (1 L/day [0.2 gal/day]), dermal absorption during showering, shower-water ingestion, and inhalation. These exposures would not be continuous because the worker would go home at the end of each workday (i.e., after 8 hours). The scenario is intended to represent nonremediation workers assumed to wear no protective clothing.

Industrial worker risk is evaluated using a unit risk factor approach consistent with that used for the TWRS EIS and DOE-RL (1999b) analyses. This approach involves calculating risk as the product of the groundwater concentration and the unit risk factor. The basic expression for risk using an unit risk factor approach is:

$$R_{x,y,t} = \sum C_{x,y,t}^i \cdot URF_S^i \quad (\text{E.17})$$

Where:

$R_{x,y,t}$	=	risk at point of compliance x,y,t
$C_{x,y,t}^i$	=	groundwater concentration at point of compliance x,y,t for contaminant i
URF_S^i	=	groundwater unit risk factor for contaminant i and receptor scenario S
x,y	=	horizontal location coordinates
t	=	time.

The summation in Equation E.17 represents addition of the contributions from all constituents. The unit risk factors used for the three HSRAM-based exposure scenarios are shown in Table E.11. These unit risk factors are for the groundwater pathway and are taken from the risk analysis presented in the TWRS EIS. These unit risk factors were also used in DOE-RL (1999).

Industrial worker risk is calculated for the same four points of compliance as defined in Section E.3.1.1.

Table E.11. Unit Risk Factors for the Industrial Worker, Residential Farmer, and Recreational Shoreline User Scenarios

Contaminant of Concern	Units	Industrial Worker ^a	Residential Farmer ^b	Recreational Shoreline User ^c
C-14	ILCR per Ci/mL	5.23E+06	6.06E+08	8.70E+05
Se-79	ILCR per Ci/mL	3.22E+07	2.87E+08	5.36E+06
Tc-99	ILCR per Ci/mL	7.11E+06	2.61E+08	1.18E+06
I-129	ILCR per Ci/mL	9.33E+08	1.29E+10	1.55E+08
Cr	HQ per g/mL	3.31E+06	1.14E+07	3.47E+05
F	HQ per g/mL	1.65E+05	1.61E+06	2.27E+04
Hg	HQ per g/mL	3.85E+07	8.36E+08	4.85E+06
NO ₃	HQ per g/mL	6.20E+03	7.59E+06	8.52E+02
NO ₂	HQ per g/mL	9.92E+03	3.73E+04	1.36E+03
EDTA	HQ per g/mL	7.61E+06	1.47E+09	1.05E+06

^aSource = TWRS EIS, Appendix D, Tables D.2.1.21 and D.2.1.23 (groundwater pathway).

^bSource = TWRS EIS, Appendix D, Tables D.2.1.18 and D.2.1.20 (groundwater pathway).

^cSource = TWRS EIS, Appendix D, Tables D.2.1.24 and D.2.1.26 (groundwater pathway).

ILCR = incremental lifetime cancer risk.

HQ = hazard quotient.

E.3.1.4 Residential Farmer Scenario

A residential farmer scenario is used to represent exposures associated with the use of the land for residential and agricultural purposes. This scenario is a slight modification to the residential scenario described in HSRAM; it includes all of the exposure pathways for the residential scenario plus most of the food ingestion pathways described in the HSRAM agriculture scenario. The residential farmer scenario includes using groundwater for drinking water (ingestion rate of 2 L/day [0.5 gal/day]) and other domestic uses as well as for irrigation to produce and consume animals, vegetables, and fruit products. The exposures are assumed to be continuous and include occasional shoreline related recreational activities, which includes contact with surface water sediments. A composite adult is used as the receptor for some of the exposure pathways. The composite adult is evaluated using child parameters for 6 years and adult parameters for 24 years, with total exposure duration of 30 years. Body weights of 16 kg (35 lb) for a child and 70 kg (150 lb) for an adult and a lifetime of 70 years are assumed.

Residential farmer risk is evaluated using a unit risk factor approach as discussed for the industrial worker scenario in Section E.3.1.3. The unit risk factors used are shown in Table E.11.

Residential farmer risks are calculated for the same four points of compliance as defined in Section E.3.1.1.

E.3.1.5 Recreational Shoreline User Scenario

A recreational shoreline user scenario consistent with the scenario described in the HSRAM is used to represent exposure to contamination in groundwater seeps along the Columbia River shoreline from recreational swimming, boating, and other shoreline activities. The scenario involves outdoor activities and occurs only in an area within 400 m (0.25 mi) of the river shoreline. These exposures would not be continuous but would occur for 14 days a year for 30 years. Exposure to both adults and children are taken into account using the same composite adult as described in the residential farmer scenario in Section E.3.1.4.

Recreational shoreline user risk is evaluated using a unit risk factor approach as described in the industrial worker scenario in Section E.3.1.3. The unit risk factors used are shown in Table E.11. Recreational shoreline user risks are calculated only at the downgradient Columbia River shoreline point of compliance that is defined in Section E.3.1.1.

The recreational land user scenario is not included in the WMA S-SX risk assessment because this receptor does not have access to the groundwater pathways.

E.3.2 TANK WASTE CONSTITUENTS OF POTENTIAL CONCERN

Determination of the constituents of potential concern (CoPCs) to be used in the WMA S-SX risk assessment starts with the estimated inventory released from the tank farm system to the environment. That estimated inventory is provided in *Inventory Estimates for SST Leaks in S and SX Tank Farms* (Jones et al. 2000). The CoPCs listed in the Jones et al. 2000 estimate include the analytes listed in the model cited in *Hanford Defined Wastes: Chemical and Radionuclide Compositions* (Agnew 1997). The following sections provide the rationale used to exclude some of these CoPCs to calculate human health risk and dose in the WMA S-SX risk assessment. Because not all of the constituents associated with the released tank waste will migrate to the groundwater, the contaminants of concern in a groundwater pathway must be selected. The rationale for making this constituents selection is provided in the following sections.

E.3.2.1 Rationale for Excluding Contaminants of Potential Concern

Following are the criteria used to exclude CoPCs from consideration in the WMA S-SX risk assessment.

- Constituents with distribution coefficients (K_d) equal or greater than 0.6. *Composite Analysis for Low-Level Waste disposal in the 200 Area Plateau of the Hanford Site* (Kincaid et al. 1998) provides reference to distribution coefficient selection used in previous studies and for past tank leaks. *Hanford Immobilized Low-Activity Tank Waste Disposal Performance Assessment* (DOE-RL 1999a), along with Kincaid et al. (1998), provides rationale for selection of CoPCs for risk calculations. Numerical modeling results provided in the TWRS EIS indicate that constituents with distribution coefficients equal to or greater than one take over 1,000 years to reach the vadose zone/saturated zone interface. Numerical modeling of past tank leaks for concurrent S tank farm retrieval performance evaluation (Thompson 2001) and for DOE-RL (1999b) indicate that within 1,000 years constituents with distribution coefficients equal to or greater than 0.6 would

not reach the underlying aquifer or would reach the underlying aquifer at very low concentrations (less than 3.0×10^{-2} pCi/L) that would not contribute to significant human health risks (less than 4.0×10^{-8} ILCR for the residential farmer scenario) using base case recharge estimates as shown in Table 3.1.

CoPCs eliminated because of the distribution coefficient criterion are aluminum, iron, bismuth, lantharium, zirconium, lead, nickel, strontium, manganese, calcium, plutonium (total), nickel-59, nickel-63, cobalt-60, strontium-90, yttrium-90, zirconium-93, niobium-93m, cadmium-113m, antimony-125, tin-126, cesium-134, cesium-137, barium-137, samarium-151, europium-152, europium-154, and europium-155, radium-226, radium-228, plutonium series, americium series, curium series, uranium series, and thorium-232.

- Low-activity radionuclides present in low concentrations and with short half-lives if they have decayed for at least five half-lives. A decay time of 5 half-lives is sufficient for decay of 96.9% of the radionuclide activity and results in a reduced level of potential risk (EPA 1995). Based on numerical modeling results provided in the TWRS EIS, constituents with distribution coefficients of 0 take 150 years to reach the vadose zone/saturated zone interface.

CoPCs eliminated because of the half-life criterion are ruthenium-106 and tritium.

- Constituents without documented human health risk or toxicity factors. The basis for these factors is documented in the *Integrated Risk Information System* (EPA 2000a) or the *User's Guide: Radionuclide Carcinogenicity* (EPA 2000b) databases. A constituent lacking a toxicity reference dose or a carcinogenic slope factor is eliminated.

CoPCs eliminated because of the health effects criterion are carbonate, chloride, calcium, hydroxide, potassium, phosphate, sulfate, silica, and sodium.

Although several organic chemicals are listed in the Agnew (1997) model, only EDTA (ethylenediaminetetraacetic acid) was carried forward because it is the only constituent that has a reference dose. All others were not listed in the Integrated Risk Information System.

In addition, field data was used for revising the risk-producing contaminants of potential concern (Section 3.3.5) that met the criteria in Section 4.3.2.1, but were determined to have inventories associated with below background levels or very small inventories in the vadose zone. The field data assisted in eliminating the uranium series isotopes (see Section 3.3.5) that appears to be overestimated in Jones et al. (2000).

E.3.2.2 Contaminants of Potential Concern for Risk Assessment

The CoPCs to be used in the WMA S-SX risk assessment after applying the exclusion criteria described in Section E.3.2.1 are:

- **Chemicals:** chromium, fluoride, mercury, nitrate, nitrite, and EDTA
- **Radionuclides:** carbon-14; selenium-79; technetium-99; and iodine-129.

E.3.3 ESTIMATING TOTAL INCREMENTAL LIFETIME CANCER RISK AND HAZARD INDEX

The total ILCR for a particular receptor scenario at a particular point in time and space is expressed as the sum of the ILCR calculated for the individual carcinogenic chemical and radionuclide CoPCs. Note that because none of the chemical CoPCs identified in Section E.3.2.2 is classified as carcinogenic, ILCR values for this assessment are based only on radionuclide exposures. Although hexavalent chromium is classified as carcinogenic by inhalation, carcinogenic impacts from hexavalent chromium would apply only for airborne releases from a facility, or for suspension of surface contamination. Because groundwater is the only exposure medium considered in this assessment, neither of these exposure routes applies and hexavalent chromium is treated as an ingestion toxicant. As for the total ILCR, the total hazard index is expressed as the sum of the hazard quotients calculated for the individual noncarcinogenic chemical CoPCs. Total ILCR and hazard index values are calculated for each receptor scenario and point of compliance for the 1,000-year period of analysis used in the contaminant transport simulations.

Risks for CoPCs included in the contaminant transport analysis (i.e., technetium-99, nitrate, and chromium) are based on the modeled groundwater concentrations. Risks for CoPCs not included in the contaminant transport analysis are based on scaled groundwater concentrations. Scaling is performed by multiplying the non-modeled CoPC source inventories (as reported in Jones et al. 2000) by the ratio of the modeled groundwater concentration to source inventory for one of the modeled CoPCs. The basis for the scaling calculations is shown in Table E.12.

Table E.12. Basis for Scaled Groundwater Concentrations

Simulated CoPC	Non-simulated CoPC Ratioed from Simulated CoPC
Tc-99	C-14, Se-79, I-129
Cr	None
NO ₃	NO ₂ , Hg, F, EDTA

CoPC = constituent of potential concern.

E.3.4 DOSE METHODOLOGY

Radionuclide doses are calculated as the product of the groundwater concentration and a unit dose factor. The unit dose factors used are groundwater pathway unit dose factors provided in Kincaid et al. (1998). Unit dose factors are shown in Table E.13. Dose calculations are performed only for the industrial worker exposure scenario. Exposure pathways and parameters associated with this scenario are described in Section E.3.1.3.

Table E.13. Industrial Worker Scenario Groundwater Unit Dose Factors

Constituent	Unit	Unit Dose Factor
C-14	(mrem/yr)/(pCi/L)	5.22E-04
Se-79	(mrem/yr)/(pCi/L)	2.17E-03
Tc-99	(mrem/yr)/(pCi/L)	3.65E-04
I-129	(mrem/yr)/(pCi/L)	6.90E-02

Source = Kincaid et al. (1998).

Industrial worker dose is calculated at the four points of compliance as defined in Section E.3.1.1.

E.4.0 VADOSE ZONE MODELING RESULTS

All simulations reported herein were performed using the STOMP simulator (White and Oostrom 2000a, 2000b). Detailed discussion on the numerical implementation for STOMP and simulation results are presented in *FY00 Initial Assessments for S-SX Field Investigation Report (FIR): Simulations of Contaminant Migration with Surface Barriers* (White et al. 2001). Results presented in the following sections are essentially based on White et al. (2001).

In this section, reporting of modeling results are focused on key flow and transport behavior, mass balance errors, and BTCs at the first compliance point (i.e., WMA S-SX boundary) for the 13 cases for two-dimensional simulations (Section E.2.1). The simulated peak aqueous concentration, time to peak concentration, and the maximum aqueous initial concentration values for the two-dimensional simulations are summarized. The maximum aqueous initial concentration values (based on the inventory estimates in Section E.2.4.3) are presented for comparison with the simulated peak aqueous concentration.

Note that the simulated BTCs and the plume maps for various cases are presented in Attachments E3 and E4, respectively, whereas the results of the recharge sensitivity runs are presented in Attachment E5. Translation of these results to the down-gradient compliance points and streamtube modeling results are described in Section E.5.0. Note that, as a check on the two-dimensional analysis, results of a three-dimensional simulation are presented in this section. However, the risk calculations are all based on two-dimensional simulation results. Also, note that the three cross-sections are labeled in two ways. For example, the row containing tanks SX-107, SX-108, and SX-109 is often labeled as cross-section SX-DD'. Similarly, cross-section SX-FF' refers to the row containing tanks SX-113, SX-114, and SX-115, and cross-section S-CC' refers to the row containing tanks S-104, S-105, and S-106.

E.4.1 BASE CASE, NO ACTION ALTERNATIVE (CASE 1)

The base case suite of simulations, Case 1, investigated solute transport through three cross-sections in WMA S-SX considering natural surface infiltration, with no water-line leaks and no interim surface barriers but with a closure barrier by the year 2040. These simulations were initialized using a steady-flow solution defined by a surface recharge rate of 100 mm/yr and a hydraulic gradient in the unconfined aquifer. Inventories of the four contaminant species were initialized using the uniform distribution pattern. Plot-file output for these simulations was generated at the years 2000, 2010, 2020, 2030, 2040, 2050, 2060, 2070, 2080, 2090, 2100, 2540, and 3000 and include values for the aqueous saturation (θ/θ_s where θ = aqueous moisture content and θ_s = saturated moisture content), aqueous pressure, aqueous moisture content, and concentrations for the four solute species. The moisture content field for these simulations remains unchanged from the initial steady-flow field until the year 2040, when the closure barrier becomes effective.

Solute BTCs at the first compliance point for the three cross-sections (S-CC', SX-DD', and SX-FF') are shown in Attachment E3, Figures E3.1 through E3.9, for the three solute species (technetium-99, chromium, and nitrate), respectively. Aqueous fluxes at the water table for the three cross-sections (S-CC', SX-DD', and SX-FF') are shown in Figures E3.10 through E3.12,

respectively. No cesium-137 was transported to the first compliance point for any of the simulated cross-sections. This is true for Case 1 as well as for all the other simulated cases.

Breakthrough times and aqueous concentrations at the first compliance point are shown in Table E.14, along with the maximum initial aqueous concentrations. Area-weighted averages (across the three cross-sections) of the solute BTCs were generated for the three solute species and are shown in Attachment E3, Figures E3.13 through E3.15 for technetium-99, chromium, and nitrate, respectively. Comparison of the peak inventory and peak arrival concentrations generally shows an order of magnitude reduction in concentration as the solute migrates through the vadose zone and across the unconfined aquifer within the WMA. Arrival times show a weak dependence on the cross-section geology.

Table E.14. Peak Concentrations and Arrival Times at the First Compliance Point (i.e., WMA S-SX Boundary) for Case 1

Parameter	S-CC'	SX-DD'	SX-FF'
Tc-99			
Arrival Time	2032.9 yr	2050.3 yr	2032.6 yr
Peak Conc.	1.379×10^5 pCi/L	1.233×10^6 pCi/L	2.869×10^5 pCi/L
Max. Initial Conc.*	4.491×10^6 pCi/L	9.480×10^7 pCi/L	5.074×10^6 pCi/L
Cr			
Arrival Time	2050.3 yr	2053.0 yr	2051.7 yr
Peak Conc.	2.818×10^3 µg/L	1.032×10^5 µg/L	4.538×10^3 µg/L
Max. Initial Conc.	6.456×10^4 µg/L	1.244×10^7 µg/L	1.089×10^5 µg/L
NO₃			
Arrival Time	2032.9 yr	2050.3 yr	2032.9 yr
Peak Conc.	8.461×10^5 µg/L	3.349×10^6 µg/L	1.013×10^6 µg/L
Max. Initial Conc.	3.254×10^7 µg/L	4.448×10^8 µg/L	3.616×10^7 µg/L

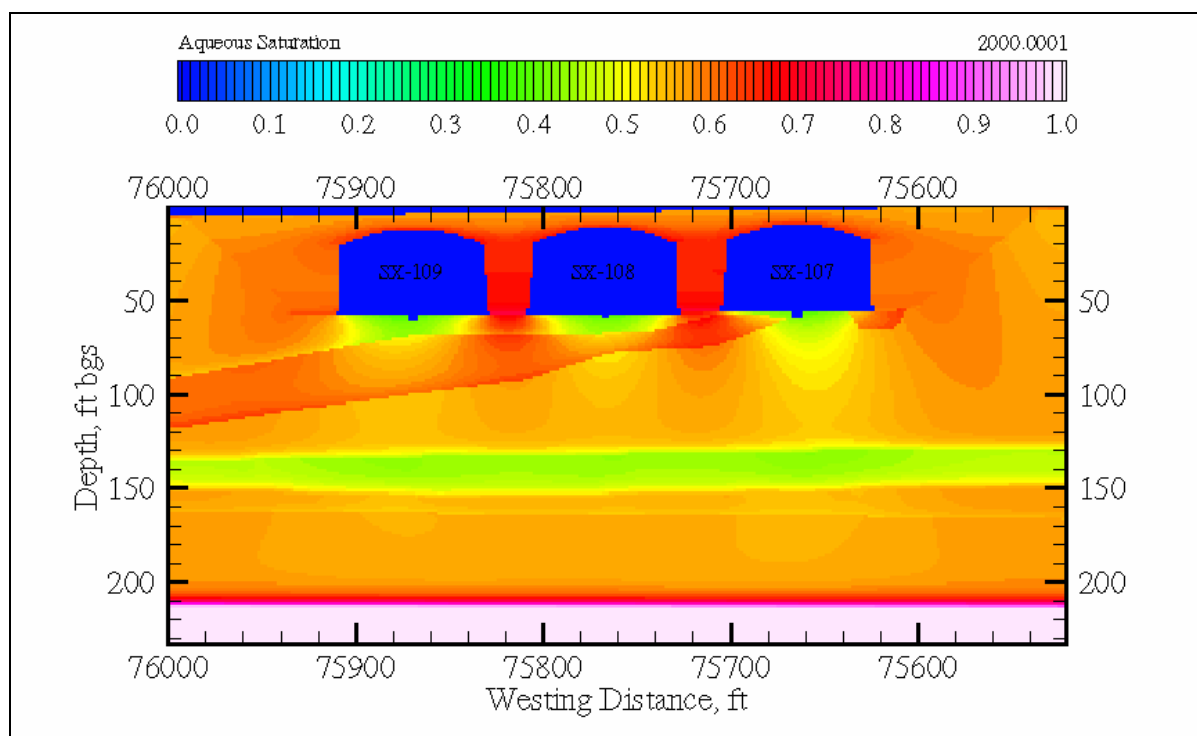
*Maximum initial concentration is based on inventory data (Section E.2.4.3) and listed for comparison with the simulated peak concentration at the compliance boundary.

Color-scaled images of solute concentrations for the three mobile species (technetium-99, chromium, and nitrate) and three cross-sections (S-CC', SX-DD', and SX-FF') are shown as a series of time sequences in Attachment E4, Figures E4.1 through E4.63. The aqueous concentrations of the solutes are color valued using exponential scaling from the drinking water standard for the specie to the maximum initial inventory concentration, where the standards are 900 pCi/L for technetium-99, 50 µg/L for chromium, and 45,000 µg/L for nitrate. Note the differences in time sequences for cross-section SX-DD' (Figures E4.1 through E4.21); the initial inventory was spread across the region between tanks SX-108 and SX-109 and centered beneath tank SX-107. Although differences are noticeable in the plume located between tanks SX-109 and SX-108 with the plume beneath tank SX-107, the overall rate of migration toward the groundwater is nearly identical. The initial inventory beneath tank SX-107 shows a slight delay in arrival times. The initial inventory distribution for chromium was located beneath the tanks.

The time sequence for chromium, depicted in Figures E4.8 through E4.14, shows an initial upward movement of the solute toward the tank bottoms. This migration occurred, in part, by diffusion, but was additionally aided by the divergent flow of recharge water in the region between tanks at the tank bottom depth. Again, for all cross-sections and solutes, the migration is principally toward the groundwater. Small variations in solute migration direction are noted in cross-section SX-DD' from the sloped gravelly sand strata, but none significantly alter the breakthrough concentrations at the WMA S-SX boundary, located on the lower right-hand corner of the domain.

The aqueous saturation field is dependent on the surface recharge, impermeable structures (e.g., single-shell tanks), various strata and their hydrologic parameters. The steady-flow saturation field for cross-section SX-DD' (tanks SX-107, SX-108, and SX-109) with 100 mm/yr of meteoric recharge is shown in Figure E.8. This field shows the impact of the tanks on the aqueous saturation, where higher than ambient saturations occur above and between the tanks and lower than ambient saturations occur just below the tanks. By 2040 a closure barrier was assumed to be active, which lowered the meteoric recharge from 100 mm/yr to 0.1 mm/yr.

**Figure E.8. Case 1 Aqueous-Phase Saturation at 2000
(steady-flow conditions) for Cross-Section SX-DD'**



The aqueous saturation field dried in response to the change in surface recharge, as shown in Figure E.9 for the year 2050. The impact of the impermeable tanks on the aqueous saturation was reduced at lower surface recharge, as shown by comparing Figures E.8 and E.9. The closure barrier was assumed to remain effective for 500 years, at which point it degrades, allowing meteoric recharge to increase to 3.5 mm/yr. In the 500-year period between 2040 and 2540, the aqueous saturation field continued to slowly dry reaching a minimum average level at 2540, as

shown in Figure E.10. In the 460-year period between 2540 and 3000, the aqueous saturation field wetted, in response to the increased meteoric recharge of 3.5 mm/yr for the degraded surface barrier. The aqueous saturation at year 3000 is shown in Figure E.11. The closure barrier was assumed to decrease the meteoric recharge from 100 mm/yr to 0.1 mm/yr for 500 years and then degrade to 3.5 mm/yr for the next 460 years. These variations in surface recharge had the greatest impact on aqueous saturation in the region between tanks within the backfill material and the soils immediately below the bottom level of the tanks.

The Plio-Pleistocene unit soil showed the least change in aqueous saturation with change in the surface recharge. The regions directly beneath the tanks additionally showed lower variability in aqueous saturation.

**Figure E.9. Case 1 Aqueous-Phase Saturation at 2050
(0.1 mm/yr) for Cross-Section SX-DD'**

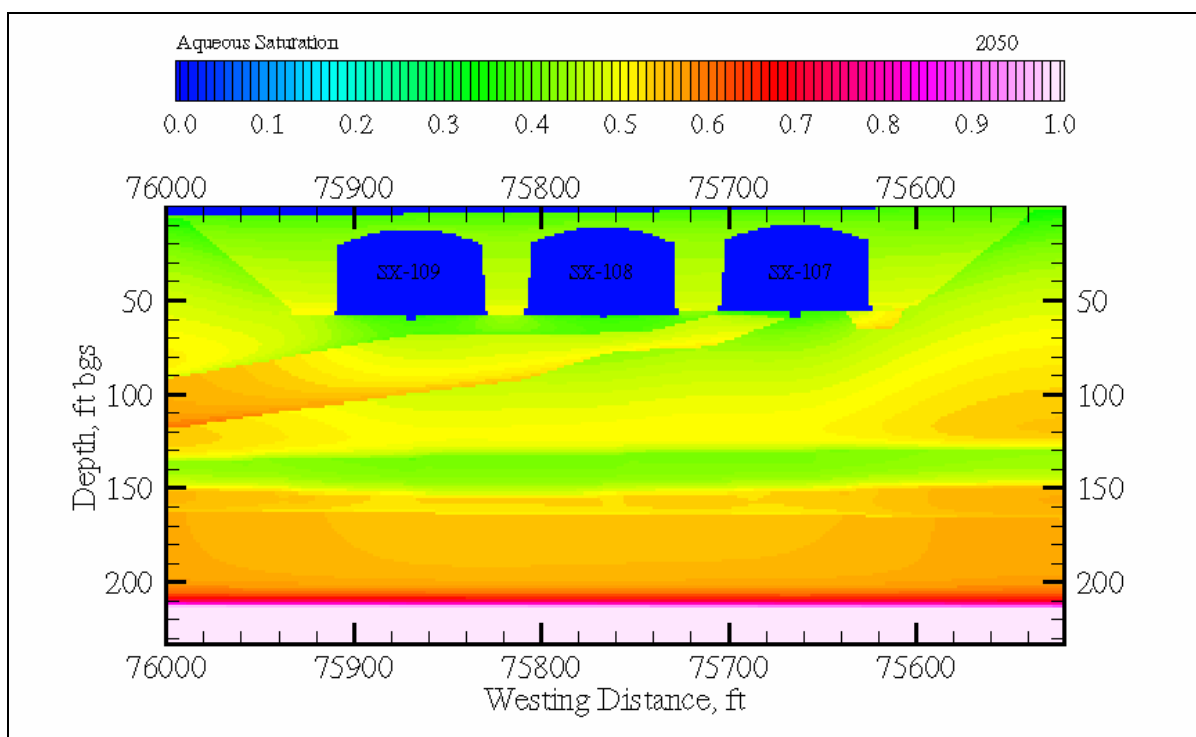


**Figure E.10. Case 1 Aqueous-Phase Saturation at 2540
(0.1 mm/yr) for Cross-Section SX-DD'**

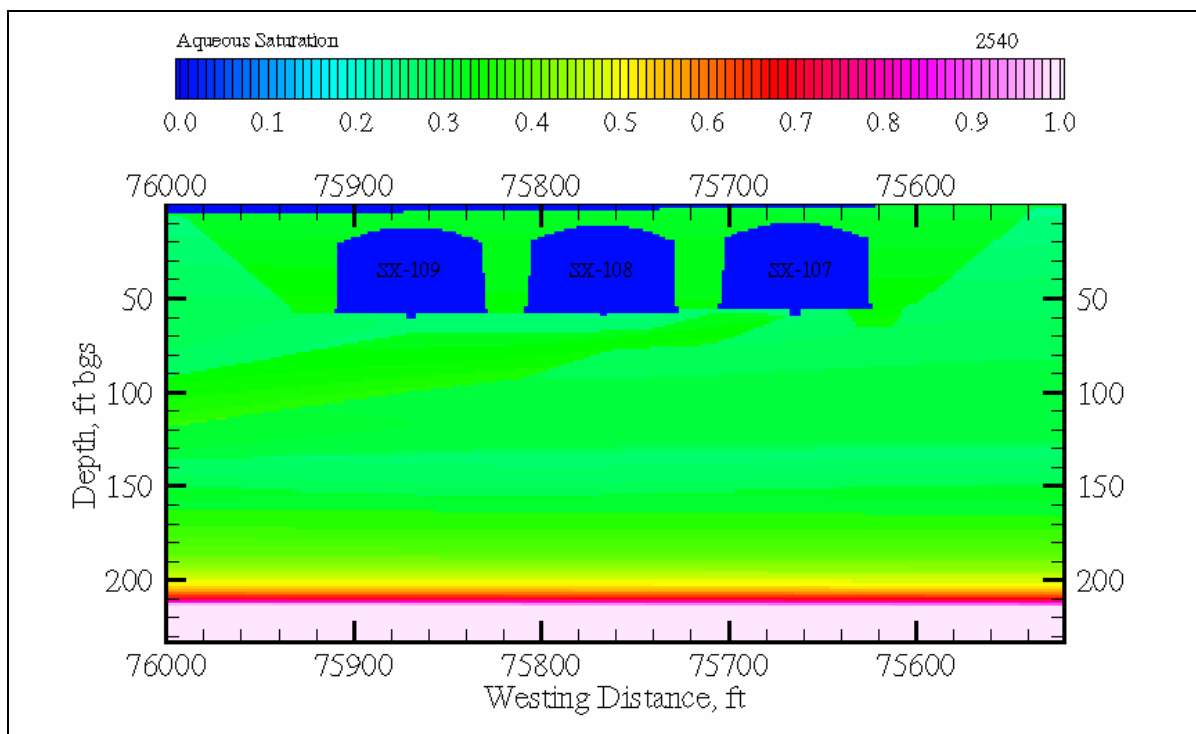
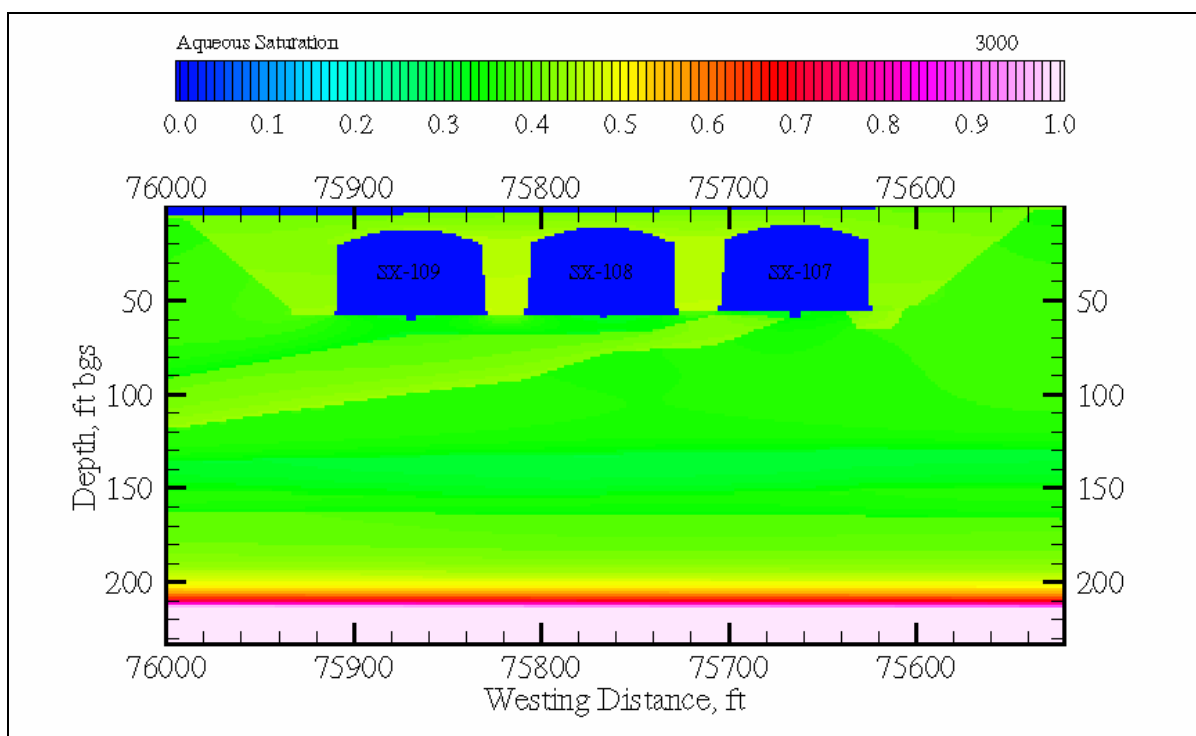


**Figure E.11. Case 1 Aqueous-Phase Saturation at 3000
(3.5 mm/yr) for Cross-Section SX-DD'**



The water table level showed little variation with the rate of surface recharge; therefore, the mean aqueous saturation in the cross-section gives a general indication of the effect of surface recharge on the hydrologic environment. Mean aqueous phase saturations at selected times during the simulation period are shown in Table E.15 for the three cross-sections (S-CC', SX-DD', and SX-FF'). As expected, the mean saturations follow the trends in surface recharge (i.e., higher mean saturations at higher surface recharge), but the rate of change in mean saturation is slow, as is evidenced by the gradual decrease in saturation during transition from 100 to 0.1 mm/yr in 2040 until the next rate change in 2540. In contrast, the aqueous flow field changes nearly immediately to variations in the surface recharge. The saturation values in Table E.15 show little variation between cross-sections.

Table E.15. Case 1 Mean Aqueous-Phase Saturation

Year	Meteoric Recharge	S-CC'	SX-DD'	SX-FF'
2000	100 mm/yr	0.5481	0.5471	0.5396
2040	100 to 0.1 mm/yr	0.5481	0.5471	0.5396
2050	0.1 mm/yr	0.4987	0.4988	0.4908
2060	0.1 mm/yr	0.4691	0.4962	0.4618
2070	0.1 mm/yr	0.4513	0.4516	0.4445
2080	0.1 mm/yr	0.4393	0.4396	0.4327
2090	0.1 mm/yr	0.4304	0.4307	0.4240
2100	0.1 mm/yr	0.4234	0.4237	0.4172
2540	0.1 to 3.5 mm/yr	0.3625	0.3623	0.3576
3000	3.5 mm/yr	0.4115	0.4106	0.4060

E.4.2 BARRIER ALTERNATIVE AND NO WATER-LINE LEAKS CASE (CASE 2)

The barrier alternative and no water-line leaks suite of simulations, Case 2, investigated solute transport through three cross-sections in WMA S-SX considering natural surface infiltration, with no water-line leaks and closure barrier by the year 2040. This suite of simulations differs from Case 1 simulations in that an interim surface barrier was implemented between the years 2010 and 2040. These simulations were initialized using a steady-flow solution defined by the surface recharge rate of 100 mm/yr and a hydraulic gradient in the unconfined aquifer.

Inventories of the four contaminant species were initialized using the uniform distribution pattern. Plot-file output for these simulations was generated at the years 2000, 2010, 2040, 2540, and 3000 and include values for the aqueous saturation, aqueous pressure, aqueous moisture content, and concentrations for the four solute species. The moisture content field for these simulations remains unchanged from the initial steady-flow.

Solute BTCs at the first compliance point for the three cross-sections (S-CC', SX-DD', and SX-FF') are shown in Attachment E3, Figures E3.16 through E3.24 for the three solute species (technetium-99, chromium, and nitrate), respectively. Aqueous flux at the water table for the three cross-sections (S-CC', SX-DD', and SX-FF') are shown in Figures E3.25 through E3.27, respectively. Breakthrough times and aqueous concentrations at the first compliance point are

shown in Table E.16, along with the maximum initial aqueous concentrations. Area-weighted averages (across the three cross-sections) of the solute BTCs were generated for the three solute species and are shown in Attachment E3, Figures E3.28 through E3.30 for technetium-99, chromium, and nitrate, respectively.

Table E.16. Peak Concentrations and Arrival Times at the First Compliance Point (i.e., WMA S-SX Boundary) for Case 2

Parameter	S-CC'	SX-DD'	SX-FF'
Tc-99			
Arrival Time	2028.3 yr	2059.7 yr	2028.3 yr
Peak Conc.	9.207×10^4 pCi/L	1.839×10^5 pCi/L	2.020×10^5 pCi/L
Max. Initial Conc.*	4.491×10^6 pCi/L	9.480×10^7 pCi/L	5.074×10^6 pCi/L
Cr			
Arrival Time	2053.3 yr	2072.3 yr	2049.3 yr
Peak Conc.	5.169×10^2 µg/L	9.623×10^3 µg/L	8.621×10^2 µg/L
Max. Initial Conc.	6.456×10^4 µg/L	1.244×10^7 µg/L	1.089×10^5 µg/L
NO₃			
Arrival Time	2028.0 yr	2052.0 yr	2027.7 yr
Peak Conc.	5.739×10^5 µg/L	5.466×10^5 µg/L	6.845×10^5 µg/L
Max. Initial Conc.	3.254×10^7 µg/L	4.448×10^8 µg/L	3.616×10^7 µg/L

*Maximum initial concentration is based on inventory data (Section E.2.4.3) and listed for comparison with the simulated peak concentration at the compliance boundary.

Results indicate that the interim surface barrier reduces solute concentrations at the compliance points but has negligible impact on the peak concentration arrival times at the first compliance point. The impact of the interim surface barrier on lower peak concentrations is most effected by the initial inventory distribution. Inventory distributions having concentrations of solute mass nearer the water table were less impacted by the interim barrier compared against the inventory mass located higher in the vadose zone. For example, the technetium-99 inventory for cross-section S-CC' is generally deeper than that for chromium, and the interim barrier reduced its peak concentration by 33%; whereas the reduction in peak concentration for chromium was 82%. Concentrations at the first compliance point at year 3000 were always higher for the interim barrier simulation compared against the Case 1 simulation, which indicates that a major impact of the interim barrier is a smoothing of the breakthrough concentrations at the compliance points.

E.4.3 NO BARRIER AND 25,000 GALLON WATER-LINE LEAK CASE (CASE 3)

The no barrier and 25,000 gallon water-line leak suite of simulations, Case 3, investigated solute transport through one cross-section in the S and SX tank farms considering natural surface infiltration and a closure barrier by the year 2040. This suite of simulations differs from the

Case 1 simulations in that a water-line leak occurs for tank SX-115 in cross-section SX-FF'. The water-line leak was modeled as a point source of water (25,000 gal over a 5-day period) spread over a 15 ft radius between tanks SX-114 and SX-115. The 15 ft radius leak area was translated to the two-dimensional simulation by using a computational grid width of 1 ft and assuming that the center of the circular leak area was situated on the center line between tanks. This approach results in a two-dimensional water-line leak of 1,061 gal over a 5-day period. These simulations were initialized using a steady-flow solution defined by the surface recharge rate of 100 mm/yr and a hydraulic gradient in the unconfined aquifer. Inventories of the four contaminant species were initialized using the uniform distribution pattern. Plot-file output for these simulations was generated at the years 2000, 2000.0137, 2000.0274, 2000.0685, 2000.137, 2000.5, 2001, 2040, 2540, and 3000 and include values for the aqueous saturation, aqueous pressure, aqueous moisture content, and concentrations for the four solute species.

The flow environment following the leak event is shown in a series of color-scaled images of aqueous saturation at 5, 10, 25, 50, 183, and 365 days after the leak in Figures E.12 through E.17, respectively. After 5 days (Figure E.12), the 25,000 gal leak has completely saturated the backfill material between tanks SX-114 and SX-115, with a portion of the saturated zone extending above the tank dome. After 10 days, the leak-water has descended into the undisturbed soils beneath the tanks (Figure E.13), with the peak front sitting above the coarser grained gravelly-sand strata. At 25 and 50 days (Figures E.14 and E.15), the leak has passed through the gravelly-sand strata, continued to migrate downward and diffuse laterally, but showed little migration down the sloped coarser-grained strata. Between 50 days and 1 year, the downward migration of the leak-water plume has slowed (Figures E.16 and E.17), and the aqueous saturation between tanks SX-114 and SX-115 has returned to within a few percent of the steady-flow conditions.

Solute BTCs at the first compliance point for cross-section SX-FF' are shown in Attachment E3, Figures E3.37 through E3.39, for the three solute species (technetium-99, chromium, and nitrate), respectively. Aqueous flux at the water table for cross-section SX-FF' is shown in Figure E3.42. Times and aqueous concentrations for the BTC peaks at the first compliance boundary are shown in Table E.17. Area-weighted averages of the solute BTCs were generated for the three solute species, as shown in Attachment E3, Figures E3.43 through E3.45 for technetium-99, chromium, and nitrate, respectively. These results indicate that although the water-line leak was sufficient to completely saturate the soil between the tanks, it had negligible impact on solute concentration and arrival times at the first compliance point. The rapid dispersion of the saturated water plume beneath the tanks and the homogenizing influence of the Plio-Pleistocene unit were the primary factors influencing the water-line leak.

**Figure E.12. Case 3 Aqueous-Phase Saturation at
2000 plus 5 days for Cross-Section SX-FF'**

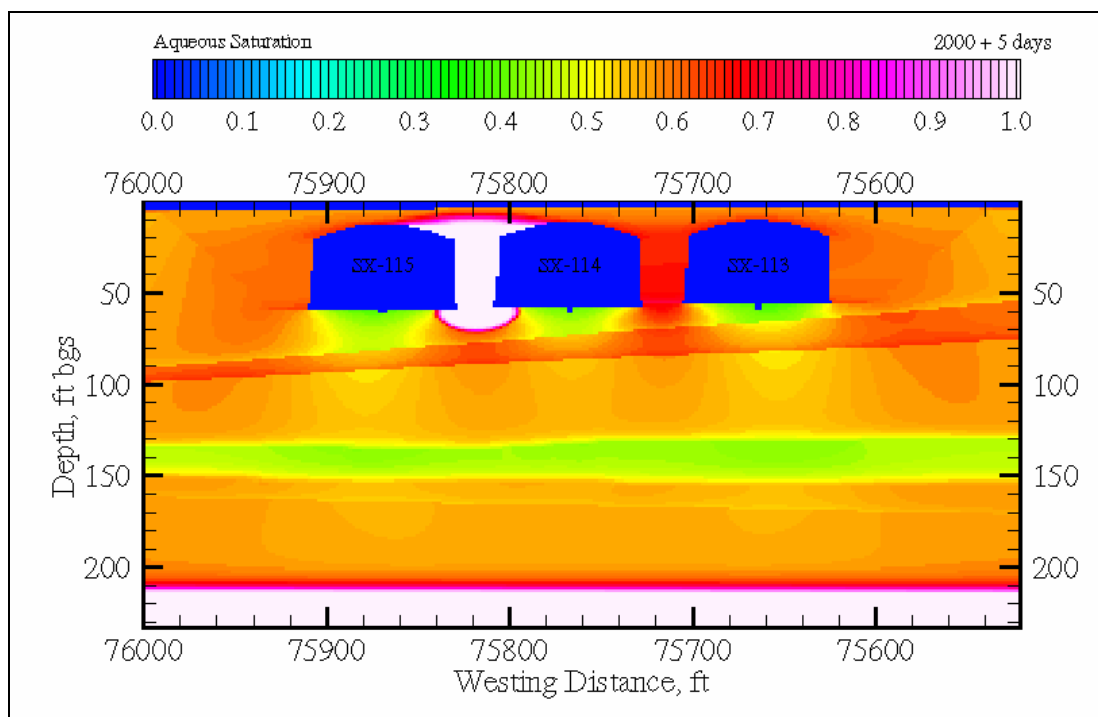


**Figure E.13. Case 3 Aqueous-Phase Saturation at
2000 plus 10 days for Cross-Section SX-FF'**

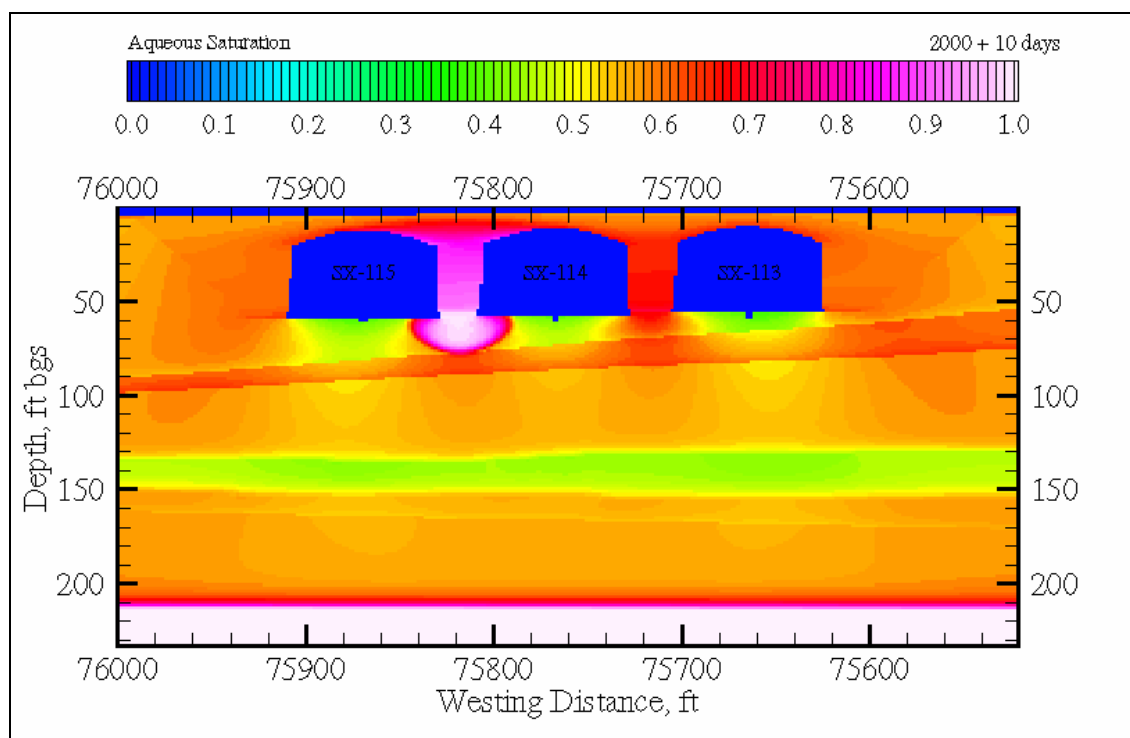


**Figure E.14. Case 3 Aqueous-Phase Saturation at
2000 plus 25 days for Cross-Section SX-FF'**

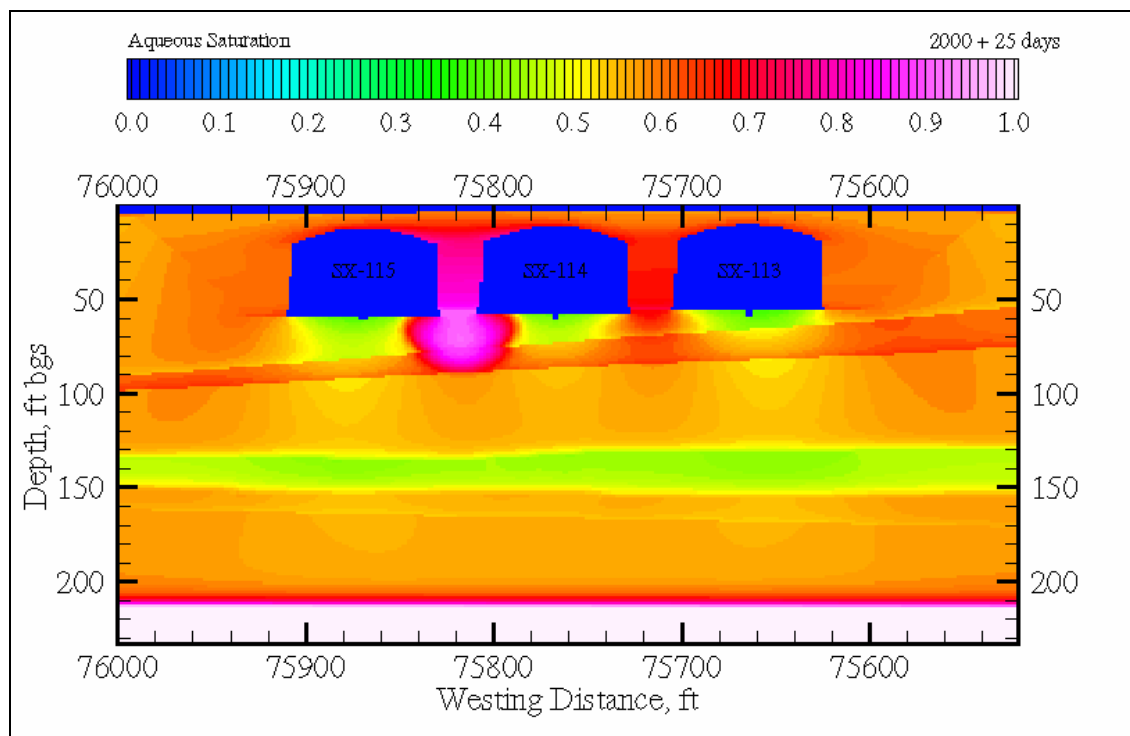


**Figure E.15. Case 3 Aqueous-Phase Saturation at
2000 plus 50 days for Cross-Section SX-FF'**

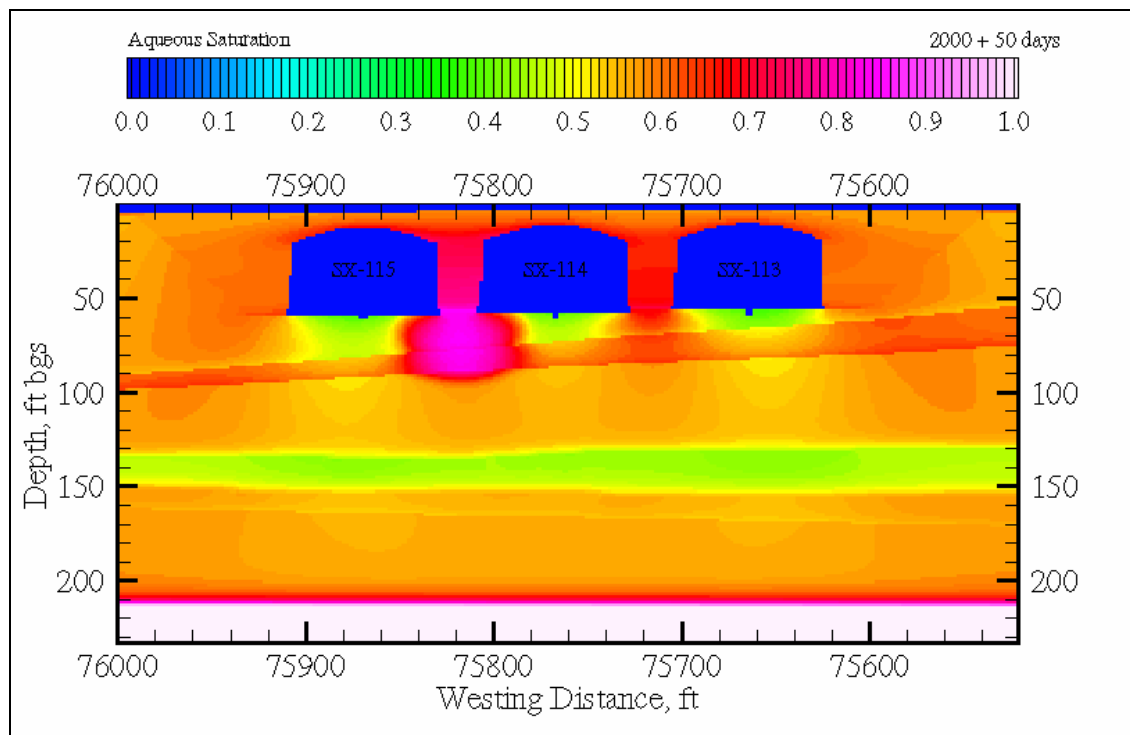


Figure E.16. Case 3 Aqueous-Phase Saturation at 2000 plus 183 days for Cross-Section SX-FF'

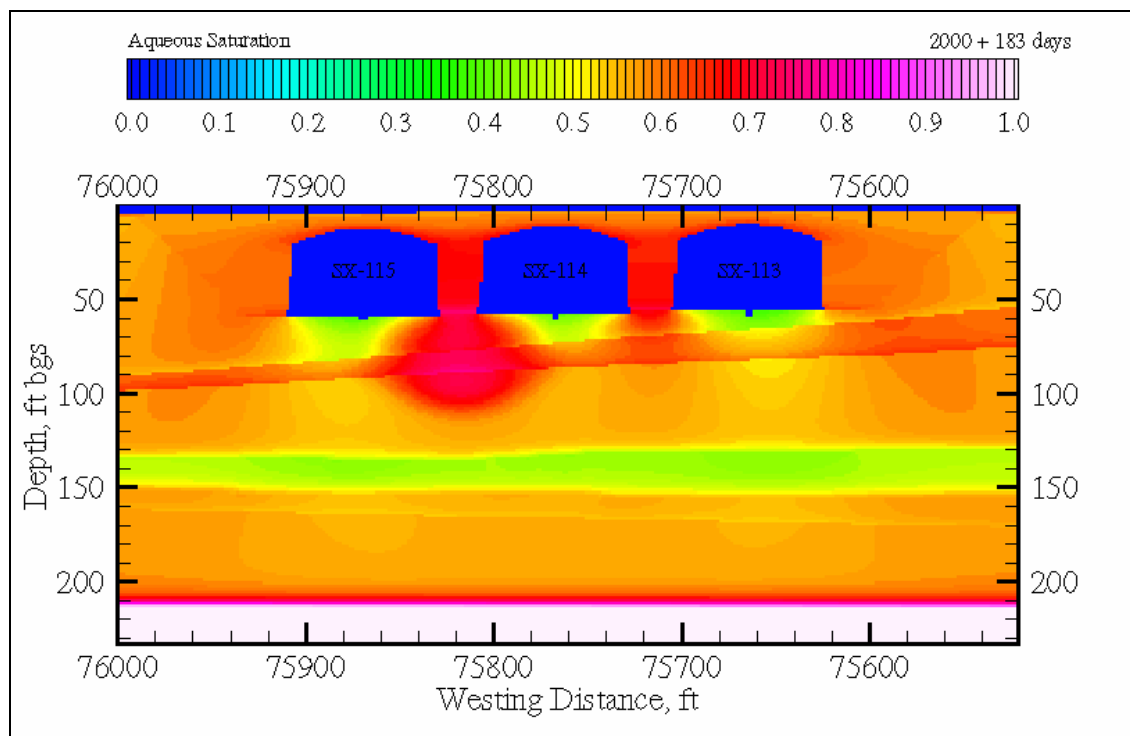
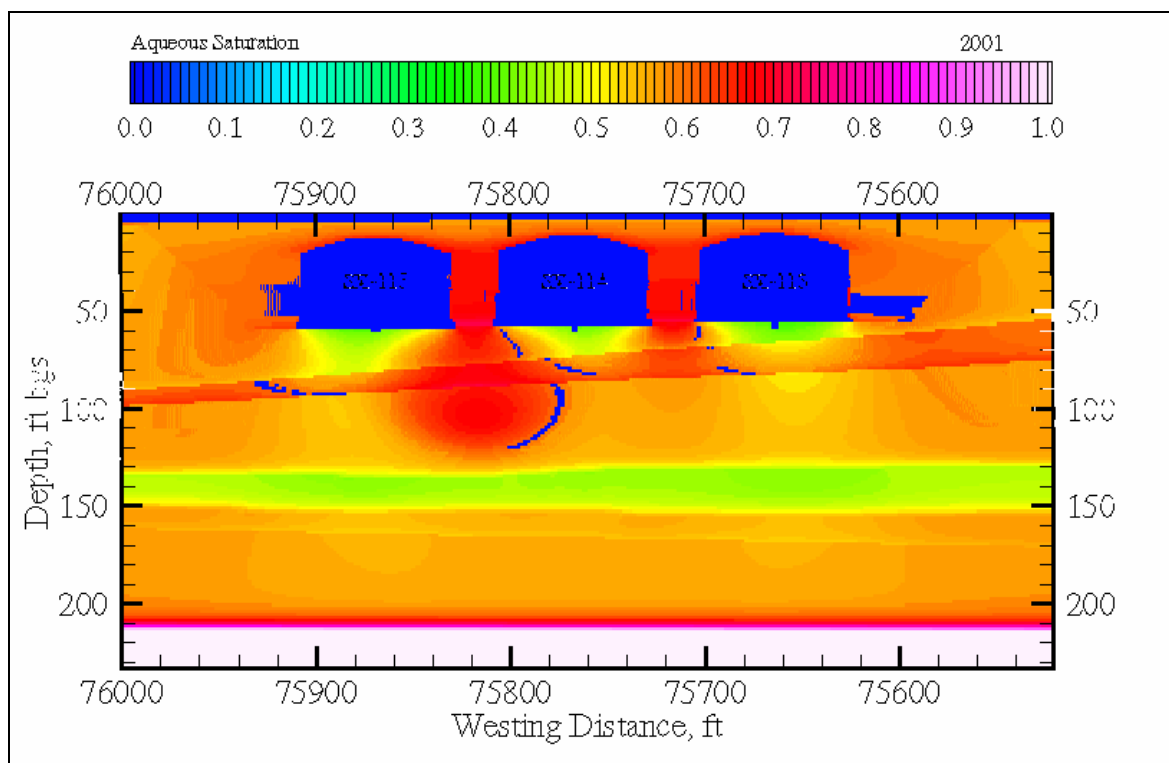


Figure E.17. Case 3 Aqueous-Phase Saturation at 2000 plus 365 days for Cross-Section SX-FF'



The impact on the transport of contaminants of the 25,000 gal leak event is shown by comparing the distribution of technetium-99 at 2001 and 2040 (Figures E.18 and E.19). By 2001, the flow field (Figure E.17) has nearly returned to steady-flow conditions leaving the distribution of technetium-99 unaltered from its initial inventory distribution, but for diffusion and reduced concentrations in the region immediately below the tank bottom between tanks SX-114 and SX-115 (Figure E.18). The distribution of technetium-99 in 2040, however, shows general downward migration toward the water table and laterally in the groundwater. These images indicate that the water-line leak event has significantly less impact on the migration of the mobile contaminant than the meteoric recharge over a 40-year period.

Figure E.18. Case 3 Technetium-99 Aqueous Concentration at 2001 for Cross-Section SX-FF'

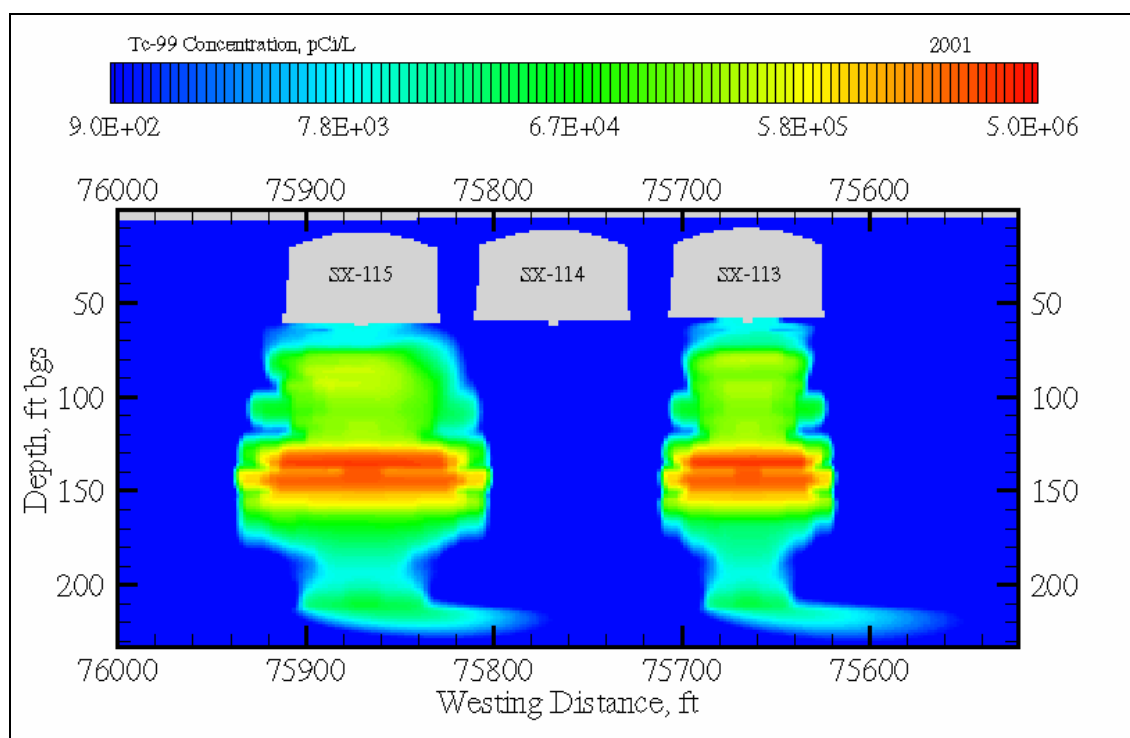


Figure E.19. Case 3 Technetium-99 Aqueous Concentration at 2040 for Cross-Section SX-FF'

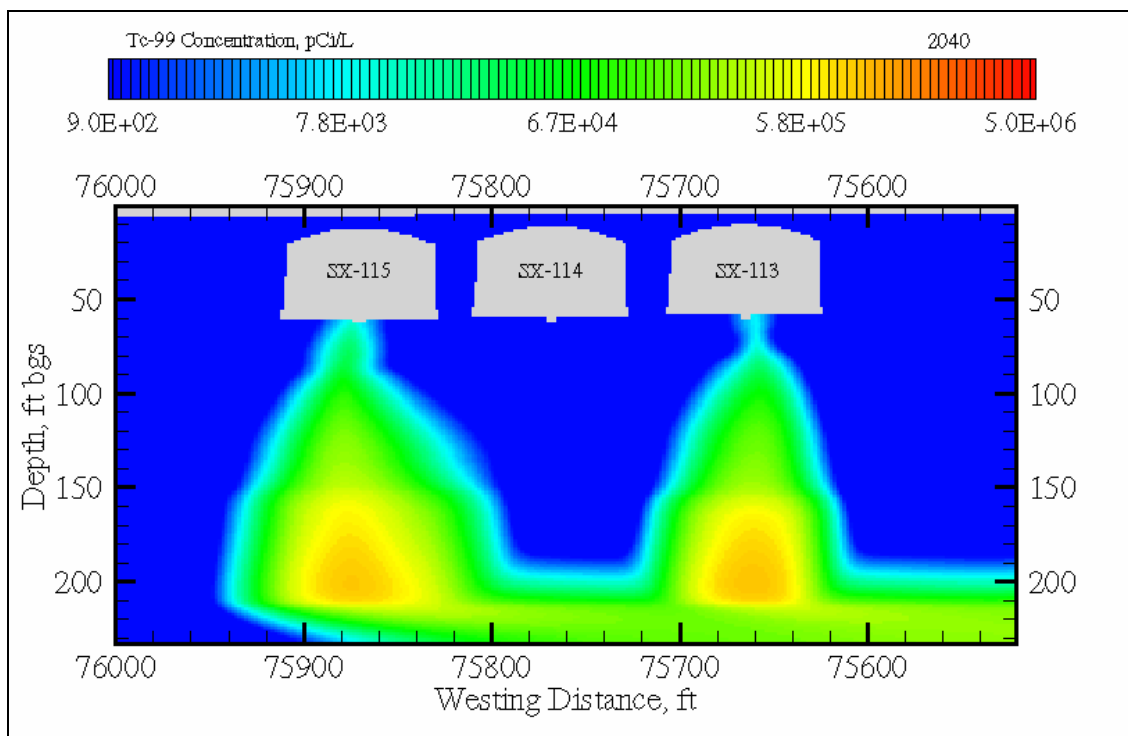


Table E.17. Peak Concentrations and Arrival Times at the First Compliance Point (i.e., WMA S-SX Boundary) for Case 3

Parameter	SX-FF'
Tc-99	
Arrival Time	2031.2 yr
Peak Conc.	2.862×10^5 pCi/L
Max Initial Conc.*	5.074×10^6 pCi/L
Cr	
Arrival Time	2051.3 yr
Peak Conc.	4.565×10^3 µg/L
Max. Initial Conc.	1.089×10^5 µg/L
NO₃	
Arrival Time	2031.9 yr
Peak Conc.	1.018×10^6 µg/L
Max Initial Conc.	3.616×10^7 µg/L

*Maximum initial concentration is based on inventory data (Section E.2.4.3) and listed for comparison with the simulated peak concentration at the compliance boundary.

E.4.4 NO BARRIER AND CLASTIC DIKES CASE (CASE 4)

The no barrier and clastic dikes suite of simulations, Case 4, investigated solute transport through one cross-section in the S and SX tank farms considering natural surface infiltration and a closure barrier by the year 2040. This suite of simulations differs from the Case 1 simulations in that a clastic dike occurs midway between tanks SX-108 and SX-109 in cross-section SX-DD'. The clastic dike was modeled as a vertical feature having hydrologic properties of its infilling material (Table E.4). The computational grid was refined in the horizontal direction in the region around the clastic dike. These simulations were initialized using a steady-flow solution defined by the upper surface recharge rate of 100 mm/yr and a hydraulic gradient in the unconfined aquifer. Inventories of the four contaminant species were initialized using the uniform distribution pattern. Plot-file output for these simulations was generated at the years 2000, 2040, 2540, and 3000 and include values for the aqueous saturation, aqueous pressure, aqueous moisture content, and concentrations for the four solute species.

Solute BTCs at the first compliance point for cross-section SX-DD' are shown in Attachment E3, Figures E3.49 through E3.51 for the three solute species (technetium-99, chromium, and nitrate), respectively. Aqueous flux at the water table for cross-section SX-DD' is shown in Figures E3.56. Times and aqueous concentrations for the BTC peaks at the first compliance boundary are shown in Table E.18. Area-weighted averages of the solute BTCs were generated for the three solute species, as shown in Attachment E3, Figures E3.58 through E3.60 for technetium-99, chromium, and nitrate, respectively. These results indicate that the clastic dike has a negligible impact on solute peak concentrations and arrival times at the first compliance point. This result is due in part to the location of the clastic dike outside of initial inventory distribution and the negligible impact of the dike on the response of the flow system.

Table E.18. Peak Concentrations and Arrival Times at the First Compliance Point (i.e., WMA S-SX Boundary) for Case 4

Parameter	SX-DD'
Tc-99	
Arrival Time	2050.3 yr
Peak Conc.	1.227×10^6 pCi/L
Max Initial Conc.*	9.480×10^7 pCi/L
Cr	
Arrival Time	2053.3 yr
Peak Conc.	1.022×10^5 µg/L
Max Initial Conc.	1.244×10^7 µg/L
NO₃	
Arrival Time	2050.7 yr
Peak Conc.	3.320×10^6 µg/L
Max Initial Conc.	4.448×10^8 µg/L

*Maximum initial concentration is based on inventory data (Section E.2.4.3) and listed for comparison with the simulated peak concentration at the compliance boundary.

E.4.5 NONUNIFORM INVENTORY DISTRIBUTION AND NO BARRIER CASE (CASE 5)

The nonuniform inventory distribution and no barrier suite of simulations, Case 5, investigated solute transport through three cross-sections in the S and SX tank farms considering natural surface infiltration, with no water-line leaks and closure barrier by the year 2040. This suite of simulations differs from the Case 1 simulations in that a nonuniform distribution was used for the initial inventory; where the inventory distribution by depth was maintained, but concentrated between tanks (Section E.2.4.2.2). These simulations were initialized using a steady-flow solution defined by the surface recharge rate of 100 mm/yr and a hydraulic gradient in the unconfined aquifer. Inventories of the four contaminant species were initialized using the nonuniform distribution pattern. Plot-file output for these simulations was generated at the years 2000, 2010, 2040, 2540, and 3000 and include values for the aqueous saturation, aqueous pressure, aqueous moisture content, and concentrations for the four solute species. The moisture content field for these simulations remains unchanged from the initial steady-flow field until the year 2040, when the closure barrier becomes effective.

Solute BTCs at the first compliance point for the three cross-sections (S-CC', SX-DD', and SX-FF') are shown in Attachment E3, Figures E3.61 through E3.69 for the three solute species (technetium-99, chromium, and nitrate), respectively. Aqueous flux at the water table for the three cross-sections (S-CC', SX-DD', and SX-FF') are shown in Figures E3.70 through E3.72, respectively. Times and aqueous concentrations for the BTC peaks at the first compliance boundary are shown in Table E.19. Area-weighted averages (across the three cross-sections) of the solute BTCs were generated for the three solute species and are shown in Attachment E3, Figures E3.73 through E3.75 for technetium-99, chromium, and nitrate, respectively.

Table E.19. Peak Concentrations and Arrival Times at the First Compliance Point (i.e., WMA S-SX Boundary) for Case 5

Parameter	S-CC'	SX-DD'	SX-FF'
Tc-99			
Arrival Time	2031.9 yr	2048.7 yr	2030.9 yr
Peak Conc.	1.779×10^6 pCi/L	5.428×10^6 pCi/L	2.627×10^6 pCi/L
Max Initial Conc.*	6.262×10^8 pCi/L	2.033×10^9 pCi/L	4.425×10^8 pCi/L
Cr			
Arrival Time	2050.3 yr	2051.3 yr	2049.3 yr
Peak Conc.	3.872×10^4 µg/L	4.485×10^5 µg/L	3.615×10^4 µg/L
Max. Initial Conc.	1.710×10^7 µg/L	1.074×10^8 µg/L	7.290×10^6 µg/L
NO₃			
Arrival Time	2031.6 yr	2049.0 yr	2029.6 yr
Peak Conc.	7.915×10^6 µg/L	7.635×10^6 µg/L	4.382×10^6 µg/L
Max. Initial Conc.	2.711×10^9 µg/L	2.159×10^9 µg/L	7.048×10^8 µg/L

*Maximum initial concentration is based on inventory data (Section E.2.4.3) and listed for comparison with the simulated peak concentration at the compliance boundary.

As indicated by the figures and Table E.19, the nonuniform distribution of initial inventory has negligible impact on arrival times of peak concentrations at the WMA S-SX boundary. This result agrees with other observations, in that peak arrival times at the WMA S-SX boundary were most strongly correlated with the initial depth of the peak concentration. The nonuniform distribution had initial aqueous concentrations that were between 4.85 and 264 times greater than corresponding values for the uniform distribution; whereas, the resulting peak concentrations at the WMA S-SX boundary were only 2.27 to 13.7 times greater than the corresponding values for the uniform distribution. The nonuniform distribution, therefore, resulted in greater dilution of the contaminant concentrations in migrating to the first compliance point from the initial inventory distribution.

E.4.6 NONUNIFORM INVENTORY DISTRIBUTION AND BARRIER CASE (CASE 6)

The nonuniform inventory distribution and barrier suite of simulations, Case 6, investigated solute transport through three cross-sections in the S and SX tank farms considering natural surface infiltration, an interim barrier, with no water-line leaks and closure barrier by the year 2040. This suite of simulations differs from the Case 1 simulations in that an interim surface barrier was implemented between the years 2010 and 2400, and a nonuniform distribution was used for the initial inventory; where the inventory distribution by depth was maintained, but concentrated between tanks (Section E.2.4.2.2). These simulations were initialized using a steady-flow solution defined by the upper surface recharge rate of 100 mm/yr and a hydraulic gradient in the unconfined aquifer. Inventories of the four contaminant species were initialized using the uniform distribution pattern. Plot-file output for these simulations was generated at the years 2000, 2010, 2040, 2540, and 3000 and include values for the aqueous saturation, aqueous pressure, aqueous moisture content, and concentrations for the four solute species. The moisture content field for these simulations remains unchanged from the initial steady-flow field until the year 2010, when the interim barrier becomes effective.

Solute BTCs at the first compliance point for the three cross-sections (S-CC', SX-DD', and SX-FF') are shown in Attachment E3, Figures E3.76 through E3.84, for the three solute species (technetium-99, chromium, and nitrate), respectively. Aqueous flux at the water table for the three cross-sections (S-CC', SX-DD', and SX-FF') are shown in Figures E3.85 through E3.87, respectively. Times and aqueous concentrations for the BTC peaks at the first compliance boundary are shown in Table E.20. Area-weighted averages (across the three cross-sections) of the solute BTCs were generated for the three solute species, as shown in Attachment E3, Figures E3.88 through E3.90 for technetium-99, chromium, and nitrate, respectively. Compared against the simulations for the nonuniform inventory distribution and no interim barrier case (Case 5), these results reflect those found for uniform inventory distributions with and without an interim barrier. As expected, the interim barrier has the greatest impact on reducing peak concentrations at the WMA S-SX boundary for those inventory distributions with solute mass located higher in the vadose zone (i.e., chromium).

Table E.20. Peak Concentrations and Arrival Times at the First Compliance Point (i.e., WMA S-SX Boundary) for Case 6

Parameter	S-CC'	SX-DD'	SX-FF'
Tc-99			
Arrival Time	2027.7 yr	2054.7 yr	2027.3 yr
Peak Conc.	1.236×10^6 pCi/L	8.669×10^5 pCi/L	2.000×10^6 pCi/L
Max. Initial Conc.*	6.262×10^8 pCi/L	2.033×10^9 pCi/L	4.425×10^8 pCi/L
Cr			
Arrival Time	2050.3 yr	2063.0 yr	2044.0 yr
Peak Conc.	6.607×10^3 µg/L	4.786×10^4 µg/L	7.732×10^3 µg/L
Max. Initial Conc.	1.710×10^7 µg/L	1.074×10^8 µg/L	7.290×10^6 µg/L
NO₃			
Arrival Time	2027.3 yr	2050.0 yr	2026.0 yr
Peak Conc.	5.648×10^6 µg/L	1.291×10^6 µg/L	3.339×10^6 µg/L
Max. Initial Conc.	2.711×10^9 µg/L	2.159×10^9 µg/L	7.048×10^8 µg/L

*Maximum initial concentration is based on inventory data (Section E.2.4.3) and listed for comparison with the simulated peak concentration at the compliance boundary.

E.4.7 LOCATION OF INVENTORY DISTRIBUTION AND NO BARRIER CASE (CASE 7)

The location of inventory distribution and no barrier suite of simulations, Case 7, investigated solute transport through three cross-sections in the S and SX tank farms considering natural surface infiltration, with no water-line leaks and closure barrier by the year 2040, and an inventory location close to the water table. This suite of simulations differs from the Case 1 simulations in that a displaced-nonuniform distribution was used for the initial inventory; where the inventory distribution by depth was maintained, but concentrated between tanks and shifted toward the water table (Section E.2.4.2.3). These simulations were initialized using a steady-flow solution defined by the upper surface recharge rate of 100 mm/yr and a hydraulic gradient in the unconfined aquifer. Plot-file output for these simulations was generated at the years 2000, 2010, 2040, 2540, and 3000 and include values for the aqueous saturation, aqueous pressure, aqueous moisture content, and concentrations for the four solute species. The moisture content field for these simulations remains unchanged from the initial steady-flow field until the year 2040, when the closure barrier becomes effective.

Solute BTCs at the first compliance point for the three cross-sections (S-CC', SX-DD', and SX-FF') are shown in Attachment E3, Figures E3.91 through E3.99, for the three solute species (technetium-99, chromium, and nitrate), respectively. Aqueous flux at the water table for the three cross-sections (S-CC', SX-DD', and SX-FF') are shown in Attachment E3, Figures E3.100 through E3.102, respectively. Times and aqueous concentrations for the BTC peaks at the first compliance boundary are shown in Table E.21. Area-weighted averages (across the three

cross-sections) of the solute BTCs were generated for the three solute species and are shown in Attachment E3, Figures E3.103 through E3.105 for technetium-99, chromium, and nitrate, respectively. These results indicate that locating the inventory near the water table greatly influences solute transport to the first compliance point, yielding earlier peak arrival times and higher peak concentrations. For cross-section S-CC', compared with the uniform distribution (Case 1), peak concentrations at the first compliance point, due to the displaced-nonuniform distribution, were 23.6 to 41.7 times higher, depending on the solute. The corresponding factors varied from 4.61 to 9.40 for cross-section SX-DD' and 12.9 to 25.4 for cross-section SX-FF', depending on the solute.

Table E.21. Peak Concentrations and Arrival Times at the First Compliance Point (i.e., WMA S-SX Boundary) for Case 7

Parameter	S-CC'	SX-DD'	SX-FF'
Tc-99			
Arrival Time	2006.9 yr	2014.9 yr	2007.6 yr
Peak Conc.	5.754×10^6 pCi/L	1.159×10^7 pCi/L	7.285×10^6 pCi/L
Max. Initial Conc.*	6.262×10^8 pCi/L	2.033×10^9 pCi/L	4.425×10^8 pCi/L
Cr			
Arrival Time	2014.6 yr	2019.6 yr	2014.3 yr
Peak Conc.	6.640×10^4 µg/L	7.633×10^5 µg/L	6.372×10^4 µg/L
Max. Initial Conc.	1.710×10^7 µg/L	1.074×10^8 µg/L	7.290×10^6 µg/L
NO₃			
Arrival Time	2006.6 yr	2014.9 yr	2005.9 yr
Peak Conc.	2.447×10^7 µg/L	1.545×10^7 µg/L	1.310×10^7 µg/L
Max. Initial Conc.	2.711×10^9 µg/L	2.159×10^9 µg/L	7.048×10^8 µg/L

*Maximum initial concentration is based on inventory data (Section E.2.4.3) and listed for comparison with the simulated peak concentration at the compliance boundary.

E.4.8 DENSITY AND VISCOSITY EFFECTS CASE (CASE 8)

The density and viscosity effects suite of simulations, Case 8, investigated solute transport through three cross-sections in the S and SX tank farms considering natural surface infiltration, with no water-line leaks and closure barrier by the year 2040. This suite of simulations differs from the Case 1 simulations in that the aqueous phase density and viscosity were dependent on the nitrate concentration, as described in Section E.2.2.5. These simulations were initialized using a steady-flow solution defined by the surface recharge rate of 100 mm/yr and a hydraulic gradient in the unconfined aquifer. Inventories of the four contaminant species were initialized using the uniform distribution pattern. Plot-file output for these simulations was generated at the years 2000, 2010, 2040, 2540, and 3000 and include values for the aqueous saturation, aqueous pressure, aqueous moisture content, and concentrations for the four solute species.

Solute BTCs at the first compliance point for the three cross-sections (S-CC', SX-DD', and SX-FF') are shown in Attachment E3, Figures E3.106 through E3.114 for the three solute species (technetium-99, chromium, and nitrate), respectively. Aqueous flux at the water table for the three cross-sections (S-CC', SX-DD', and SX-FF') are shown in Figures E3.115 through E3.117, respectively. Times and aqueous concentrations for the BTC peaks at the first compliance boundary are shown in Table E.22. Area-weighted averages (across the three cross-sections) of the solute BTCs were generated for the three solute species and are shown in Attachment E3, Figures E3.118 through E3.120 for technetium-99, chromium, and nitrate, respectively.

Table E.22. Peak Concentrations and Arrival Times at the First Compliance Point (i.e., WMA S-SX Boundary) for Case 8

Parameter	S-CC'	SX-DD'	SX-FF'
Tc-99			
Arrival Time	2032.7 yr	2050.0 yr	2032.3 yr
Peak Conc.	1.393×10^5 pCi/L	1.260×10^6 pCi/L	2.905×10^5 pCi/L
Max. Initial Conc.*	4.491×10^6 pCi/L	9.480×10^7 pCi/L	5.074×10^6 pCi/L
Cr			
Arrival Time	2050.3 yr	2052.3 yr	2051.3 yr
Peak Conc.	2.819×10^3 µg/L	1.052×10^5 µg/L	4.545×10^3 µg/L
Max. Initial Conc.	6.456×10^4 µg/L	1.244×10^7 µg/L	1.089×10^5 µg/L
NO₃			
Arrival Time	2032.7 yr	2050.0 yr	2032.3 yr
Peak Conc.	8.538×10^5 µg/L	3.423×10^6 µg/L	1.024×10^6 µg/L
Max. Initial Conc.	3.254×10^7 µg/L	4.448×10^8 µg/L	3.616×10^7 µg/L

*Maximum initial concentration is based on inventory data (Section E.2.4.3) and listed for comparison with the simulated peak concentration at the compliance boundary.

Increasing nitrate concentration increases both the aqueous density and viscosity. These property changes have opposite effect; that is, increasing aqueous density increases the gravitational body force on a nitrate plume, but increasing viscosity reduces the plume fluidity. Because of the opposing flow effects, the solute migration toward the WMA S-SX boundary was nearly unchanged from the Case 1 simulations.

E.4.9 BASE CASE WITH 50 MM/YR METEORIC RECHARGE CASE (CASE 9)

The base case with 50 mm/yr meteoric recharge suite of simulations, Case 9, investigated solute transport through three cross-sections in WMA S-SX considering natural surface infiltration, with no water-line leaks and no interim surface barriers, but with a closure barrier by the year 2040. These simulations along with those from Cases 1, 10, and 11 form a sensitivity study on the effect of meteoric recharge on the migration of solutes to the WMA S-SX boundary.

The simulations in this case were initialized using a steady-flow solution defined by the surface recharge rate of 50 mm/yr and a hydraulic gradient in the unconfined aquifer. Inventories of the four contaminant species were initialized using the uniform distribution pattern. Plot-file output for these simulations was generated at the years 2000, 2040, 2540, and 3000 and include values for the aqueous saturation, aqueous pressure, aqueous moisture content, and concentrations for the four solute species. The moisture field for these simulations remains unchanged from the initial steady-flow field until the year 2040, when the closure barrier becomes effective.

Solute BTCs at the first compliance point for the three cross-sections (S-CC', SX-DD', and SX-FF') are shown in Attachment E3, Figures E3.121 through E3.129, for the three solute species (technetium-99, chromium, and nitrate), respectively. Aqueous fluxes at the water table for the three cross-sections (S-CC', SX-DD', and SX-FF') are shown in Figures E3.130 through E3.132, respectively. Breakthrough times and aqueous concentrations at the first compliance point are shown in Table E.23, along with the maximum initial aqueous concentrations. Area-weighted averages (across the three cross-sections) of the solute BTCs were generated for the three solute species and are shown in Attachment E3, Figures E3.133 through E3.135 for technetium-99, chromium, and nitrate, respectively.

Table E.23. Peak Concentrations and Arrival Times at the First Compliance Point (i.e., WMA S-SX Boundary) for Case 9

Parameter	S-CC'	SX-DD'	SX-FF'
Tc-99			
Arrival Time	2055.9 yr	2074.0 yr	2054.3 yr
Peak Conc.	9.234×10^4 pCi/L	3.744×10^5 pCi/L	1.988×10^5 pCi/L
Max. Initial Conc.*	4.491×10^6 pCi/L	9.480×10^7 pCi/L	5.074×10^6 pCi/L
Cr			
Arrival Time	2072.3 yr	2081.7 yr	2070.3 yr
Peak Conc.	8.966×10^2 µg/L	2.221×10^4 µg/L	1.651×10^3 µg/L
Max. Initial Conc.	6.456×10^4 µg/L	1.244×10^7 µg/L	1.089×10^5 µg/L
NO₃			
Arrival Time	2055.3 yr	2071.3 yr	2054.0 yr
Peak Conc.	5.688×10^5 µg/L	1.048×10^6 µg/L	7.135×10^5 µg/L
Max. Initial Conc.	3.254×10^7 µg/L	4.448×10^8 µg/L	3.616×10^7 µg/L

*Maximum initial concentration is based on inventory data (Section E.2.4.3) and listed for comparison with the simulated peak concentration at the compliance boundary.

The steady-flow saturation field for cross-section SX-DD' (tanks SX-107, SX-108, and SX-109) with 50 mm/yr of meteoric recharge is shown in Figure E.20. This field shows little variation from that for the 100 mm/yr meteoric recharge case (Case 1) (Figure E.8). Although this series of simulations yielded only slight changes in the initial mean saturation (Tables E.15 and E.24), peak concentrations and their arrival times at the WMA S-SX boundary changed considerably.

Reductions in solute concentrations at the WMA S-SX boundary were primarily correlated with the initial inventory distributions. The technetium-99 and nitrate solute concentrations were reduced to approximately 60% of the Case 1 values; whereas, the chromium solute concentrations showed reductions to approximately 30%. Comparisons of solute BTCs for the various initial meteoric recharge rates at the first compliance point are shown for each combination of cross-section and solute in Attachment E5, Figures E5.1 through E5.9. Comparisons of aqueous fluxes at the water table for the various initial meteoric recharge rates for the three cross-sections are shown in Figures E5.10 through E5.12.

Figure E.20. Case 9 Aqueous-Phase Saturation at 2000 (50 mm/yr) for Cross-Section SX-DD'

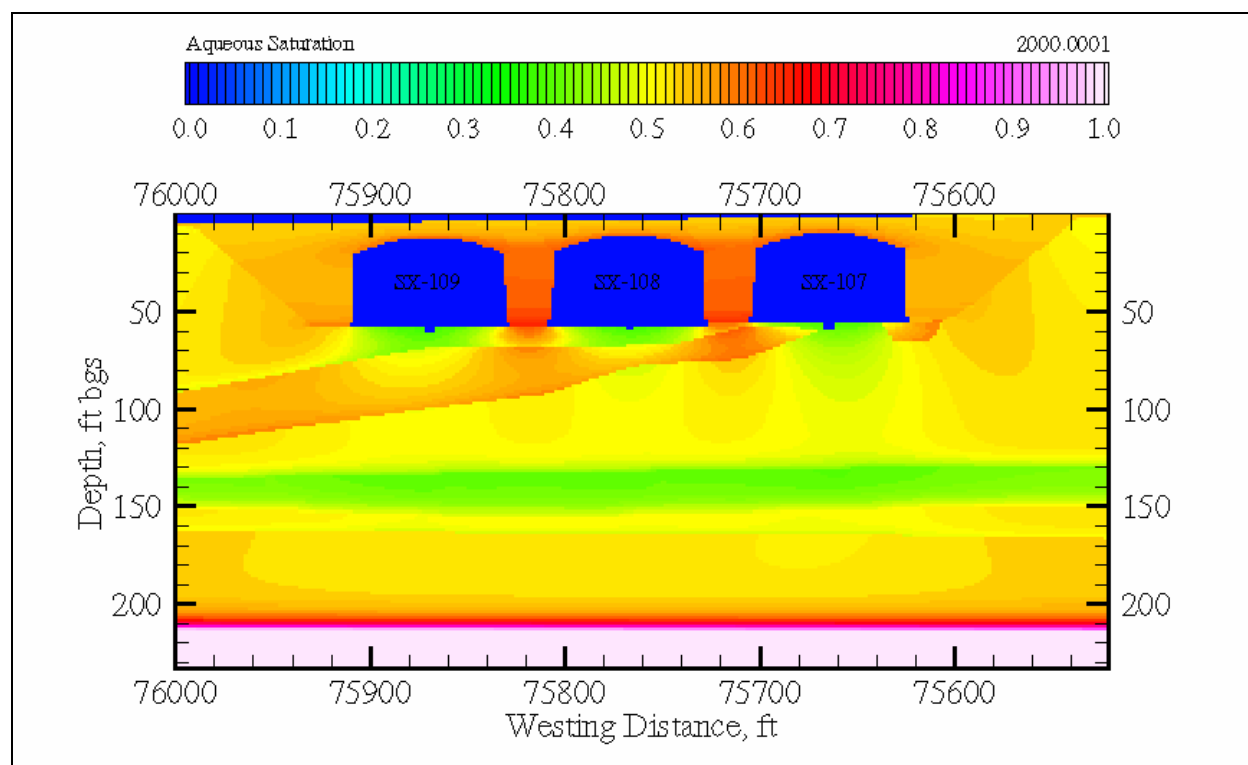


Table E.24. Case 9 Mean Aqueous-Phase Saturation

Year	Meteoric Recharge	S-CC'	SX-DD'	SX-FF'
2000	50 mm/yr	0.5135	0.5125	0.5057
2040	50 to 0.1 mm/yr	0.5135	0.5125	0.5057
2540	0.1 to 3.5 mm/yr	0.3625	0.3623	0.3576
3000	3.5 mm/yr	0.4115	0.4106	0.4060

The water table level showed little variation with the rate of surface recharge; therefore, the mean aqueous saturation in the cross-section gives a general indication of the effect of surface recharge on the flow environment. Mean aqueous phase saturations at selected times during the simulation period are shown in Table E.24 for the three cross-sections (S-CC', SX-DD', and SX-FF'). As expected, the mean saturations follow the trends in surface recharge (i.e., higher mean saturations at higher surface recharge). However, the rate of change in mean saturation is slow, as evidenced by the gradual decrease in saturation during transition from 50 to 0.1 mm/yr in 2040 until the next rate change in 2540. In contrast, the aqueous flow field changes almost immediately to variations in the surface recharge. The saturation values in Table E.24 show little variation between cross-sections.

E.4.10 BASE CASE WITH 30 MM/YR METEORIC RECHARGE (CASE 10)

The base case with 30 mm/yr meteoric recharge suite of simulations, Case 10, investigated solute transport through three cross-sections in WMA S-SX considering natural surface infiltration, with no water-line leaks and no interim surface barriers, but with a closure barrier by the year 2040. These simulations along with those from Cases 1, 9, and 11 form a sensitivity study on the effect of meteoric recharge on the migration of solutes to the WMA S-SX boundary.

The simulations in this case were initialized using a steady-flow solution defined by the surface recharge rate of 30 mm/yr and a hydraulic gradient in the unconfined aquifer. Inventories of the four contaminant species were initialized using the uniform distribution pattern. Plot-file output for these simulations was generated at the years 2000, 2040, 2540, and 3000 and include values for the aqueous saturation, aqueous pressure, aqueous moisture content, and concentrations for the four solute species. The moisture content field for these simulations remains unchanged from the initial steady-flow field until the year 2040, when the closure barrier becomes effective.

Solute BTCs at the first compliance point for the three cross-sections (S-CC', SX-DD', and SX-FF') are shown in Attachment E3, Figures E3.136 through E3.144, for the three solute species (technetium-99, chromium, and nitrate), respectively. Aqueous fluxes at the water table for the three cross-sections (S-CC', SX-DD', and SX-FF') are shown in Figures E3.145 through E3.147, respectively. Breakthrough times and aqueous concentrations at the first compliance point are shown in Table E.25, along with the maximum initial aqueous concentrations.

Area-weighted averages (across the three cross-sections) of the solute BTCs were generated for the three solute species and are shown in Attachment E3, Figures E3.148 through E3.150 for technetium-99, chromium, and nitrate, respectively.

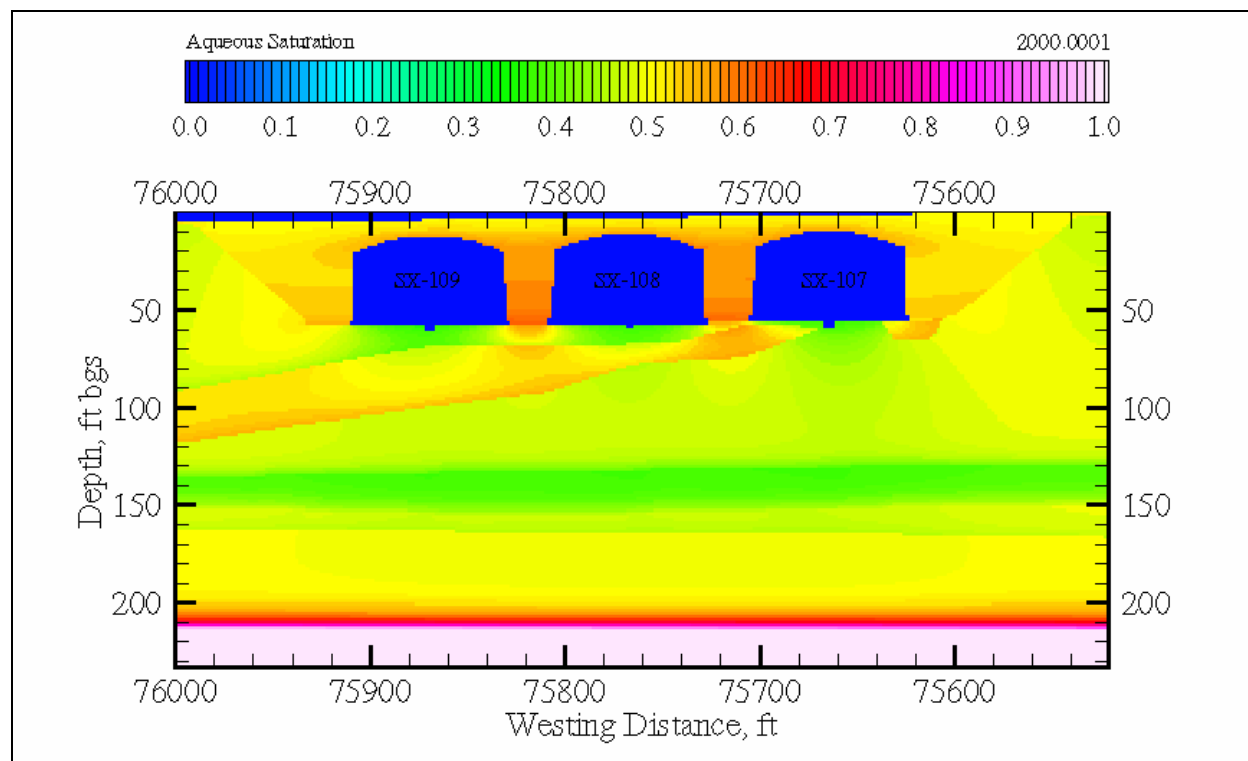
Table E.25. Peak Concentrations and Arrival Times at the First Compliance Point (i.e., WMA S-SX Boundary) for Case 10

Parameter	S-CC'	SX-DD'	SX-FF'
Tc-99			
Arrival Time	2073.0 yr	2125.3 yr	2070.3 yr
Peak Conc.	5.219×10^4 pCi/L	1.114×10^5 pCi/L	1.233×10^5 pCi/L
Max. Initial Conc.*	4.491×10^6 pCi/L	9.480×10^7 pCi/L	5.074×10^6 pCi/L
Cr			
Arrival Time	2115.3 yr	3000.0 yr	2070.3 yr
Peak Conc.	3.013×10^2 µg/L	7.248×10^3 µg/L	5.903×10^2 µg/L
Max. Initial Conc.	6.456×10^4 µg/L	1.244×10^7 µg/L	1.089×10^5 µg/L
NO₃			
Arrival Time	2072.3 yr	2113.0 yr	2070.0 yr
Peak Conc.	3.268×10^5 µg/L	3.240×10^5 µg/L	4.324×10^5 µg/L
Max. Initial Conc.	3.254×10^7 µg/L	4.448×10^8 µg/L	3.616×10^7 µg/L

*Maximum initial concentration is based on inventory data (Section E.2.4.3) and listed for comparison with the simulated peak concentration at the compliance boundary.

The steady-flow saturation field for cross-section SX-DD' (tanks SX-107, SX-108, and SX-109) with 30 mm/yr of meteoric recharge is shown in Figure E.21. The saturation field shows slight variation from those for the 50 mm/yr (Case 9) and 100 mm/yr (Case 1) meteoric recharge cases (Figures E.8 and E.20). Most notable is the overall reduction in saturation and the reduction in shadowing beneath the tanks. The effects of lowering the initial meteoric recharge to 30 mm/yr were similar to those of lowering the recharge from 100 to 50 mm/yr; peak concentrations at the WMA S-SX boundary were lowered and arrival times of the concentration peaks were delayed. Again, reductions in solute concentrations at the WMA S-SX boundary were primarily correlated with the initial inventory distributions. Comparisons of solute BTCs for the four initial meteoric recharge rates (100, 50, 30, and 10 mm/yr) at the first compliance point are shown for each combination of cross-section and solute in Attachment E5, Figures E5.1 through E5.9. Likewise, comparisons of aqueous fluxes at the water table for the four initial meteoric recharge rates for the three cross-sections are shown in Figures E5.10 through E5.12.

Figure E.21. Case 10 Aqueous-Phase Saturation at 2000 (30 mm/yr) for Cross-Section SX-DD'



The water table level showed little variation with the rate of surface recharge; therefore, the mean aqueous saturation in the cross-section gives a general indication of the effect of surface recharge on the hydrologic environment. Mean aqueous phase saturations at selected times during the simulation period are shown in Table E.26 for the three cross-sections (S-CC', SX-DD', and SX-FF'). The saturation values in Table E.26 show little variation between cross-sections.

Table E.26. Case 10 Mean Aqueous-Phase Saturation

Year	Meteoric Recharge	S-CC'	SX-DD'	SX-FF'
2000	30 mm/yr	0.4902	0.4893	0.4829
2040	30 to 0.1 mm/yr	0.4902	0.4893	0.4829
2540	0.1 to 3.5 mm/yr	0.3625	0.3623	0.3576
3000	3.5 mm/yr	0.4115	0.4106	0.4060

E.4.11 BASE CASE WITH 10 MM/YR METEORIC RECHARGE (CASE 11)

The base case with 10 mm/yr meteoric recharge suite of simulations, Case 11, investigated solute transport through three cross-sections in the WMA S-SX considering natural surface infiltration, with no water-line leaks and no interim surface barriers, but with a closure barrier by the year 2040. These simulations along with those from Cases 1, 9, and 10 form a sensitivity study on the

effect of meteoric recharge on the migration of solutes to the WMA S-SX boundary.

The simulations in this case were initialized using a steady-flow solution defined by the surface recharge rate of 10 mm/yr and a hydraulic gradient in the unconfined aquifer. Inventories of the four contaminant species were initialized using the uniform distribution pattern. Plot-file output for these simulations was generated at the years 2000, 2040, 2540, and 3000 and include values for the aqueous saturation, aqueous pressure, aqueous moisture content, and concentrations for the four solute species. The moisture content field for these simulations remains unchanged from the initial steady-flow field until the year 2040, when the closure barrier becomes effective.

Solute BTCs at the first compliance point for the three cross-sections (S-CC', SX-DD', and SX-FF') are shown in Attachment E3, Figures E3.151 through E3.159, for the three solute species (technetium-99, chromium, and nitrate), respectively. Aqueous fluxes at the water table for the three cross-sections (S-CC', SX-DD', and SX-FF') are shown in Figures E3.160 through E3.162, respectively. Breakthrough times and aqueous concentrations at the first compliance point are shown in Table E.27, along with the maximum initial aqueous concentrations. Area-weighted averages (across the three cross-sections) of the solute BTCs were generated for the three solute species and are shown in Attachment E3, Figures E3.163 through E3.165 for technetium-99, chromium, and nitrate, respectively.

Table E.27. Peak Concentrations and Arrival Times at the First Compliance Point (i.e., WMA S-SX Boundary) for Case 11

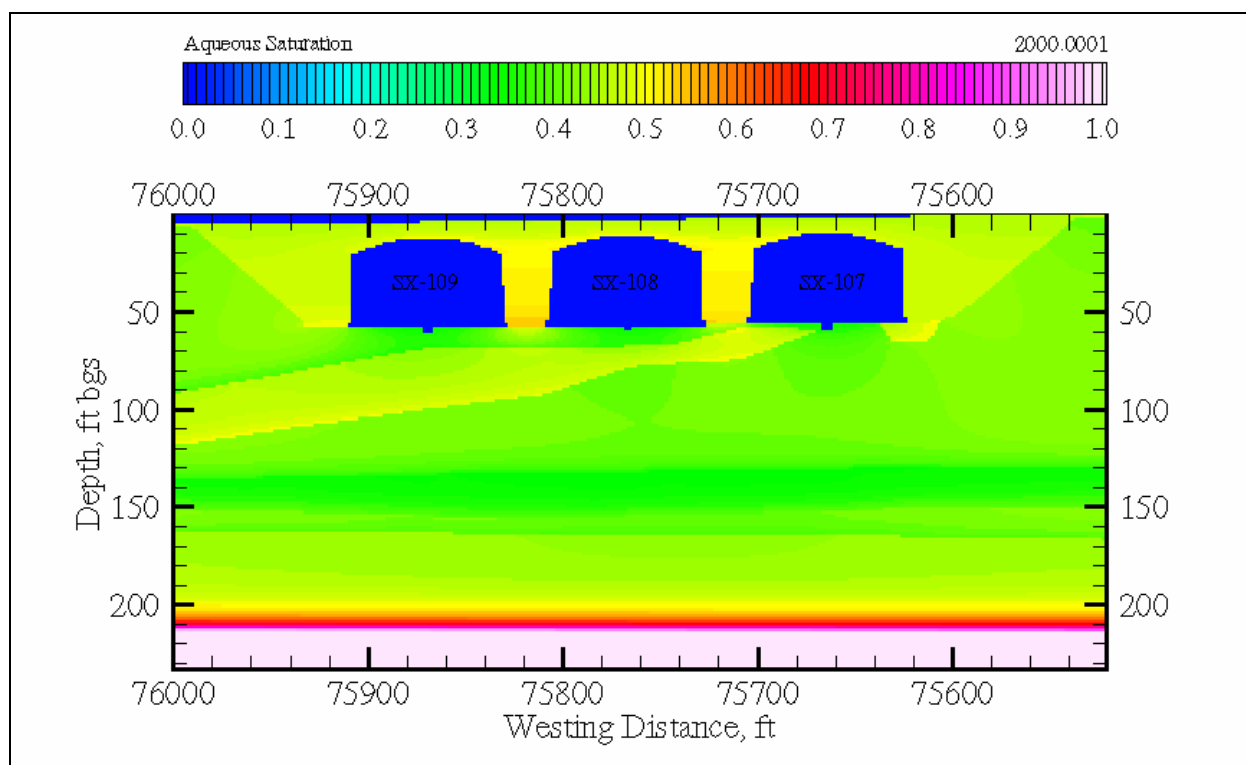
Parameter	S-CC'	SX-DD'	SX-FF'
Tc-99			
Arrival Time	2176.0 yr	3000.0 yr	2153.0 yr
Peak Conc.	1.057×10^4 pCi/L	6.775×10^4 pCi/L	2.783×10^4 pCi/L
Max. Initial Conc.*	4.491×10^6 pCi/L	9.480×10^7 pCi/L	5.074×10^6 pCi/L
Cr			
Arrival Time	3000.0 yr	3000.0 yr	3000.0 yr
Peak Conc.	1.609×10^2 µg/L	4.157×10^3 µg/L	3.133×10^2 µg/L
Max. Initial Conc.	6.456×10^4 µg/L	1.244×10^7 µg/L	1.089×10^5 µg/L
NO₃			
Arrival Time	2171.0 yr	3000.0 yr	2152.0 yr
Peak Conc.	6.819×10^4 µg/L	1.812×10^5 µg/L	9.895×10^4 µg/L
Max. Initial Conc.	3.254×10^7 µg/L	4.448×10^8 µg/L	3.616×10^7 µg/L

*Maximum initial concentration is based on inventory data (Section E.2.4.3) and listed for comparison with the simulated peak concentration at the compliance boundary.

The steady-flow saturation field for cross-section SX-DD' (tanks SX-107, SX-108, and SX-109) with 10 mm/yr of meteoric recharge is shown in Figure E.22. Compared against the steady-flow saturation fields for 100, 50, and 30 mm/yr (Figures E.8, E.20, and E.21), the saturation field at 10 mm/yr shows no shadowing from the tanks and only slight increases in moisture between the

tanks. The 10 mm/yr recharge rate differs from the higher recharge rates investigated; the downward aqueous flow was sufficiently low to delay the peak arrival times to after the year 3000 for those solutes with shallower initial inventories. This behavior was predicted for chromium in all three cross-sections, and for technetium-99 and nitrate in cross-section SX-DD'. In general, the solute transport response to lower meteoric recharge is similar to that for surface barriers, but with greater consequence because of the earlier implementation of the reduced migration rates toward the groundwater. Comparisons of solute BTCs for the four initial meteoric recharge rates (100, 50, 30, and 10 mm/yr) at the first compliance point are shown for each combination of cross-section and solute in Attachment E5, Figures E5.1 through E5.9. Comparison of aqueous fluxes at the water table for the four initial meteoric recharge rates for the three cross-sections are shown in Figures E5.10 through E5.12.

Figure E.22. Case 11 Aqueous-Phase Saturation at 2000 (50 mm/yr) for Cross-Section SX-DD'



The water table level showed little variation with the rate of surface recharge; therefore, the mean aqueous saturation in the cross-section gives a general indication of the effect of surface recharge on the hydrologic environment. Mean aqueous phase saturations at selected times during the simulation period are shown in Table E.28 for the three cross-sections (S-CC', SX-DD', and SX-FF'). As expected the mean saturations follow the trends in surface recharge (i.e., higher mean saturations at higher surface recharge). The saturation values in Table E.28 show little variation between cross-sections.

Table E.28. Case 11 Mean Aqueous-Phase Saturation

Year	Meteoric Recharge	S-CC'	SX-DD'	SX-FF'
2000	50 mm/yr	0.4463	0.4455	0.4108
2040	50 to 0.1 mm/yr	0.4463	0.4455	0.4108
2540	0.1 to 3.5 mm/yr	0.3625	0.3623	0.3576
3000	3.5 mm/yr	0.4115	0.4106	0.4060

E.4.12 ALTERNATE INVENTORY DISTRIBUTION CASE (CASE 12)

The alternate inventory distribution suite of simulations, Case 12, investigated solute transport through three cross-sections in WMA S-SX considering natural surface infiltration, with no water-line leaks and closure barrier by the year 2040, and an alternate nonuniform distribution. The alternate inventory distributions are shown in Attachment E2, Figures E2.37 through E2.48. This suite of simulations differs from the Case 1 simulations in that an alternate distribution was used for the initial inventory; where the inventory distribution by depth was maintained but uniformly spread over the region beneath the tanks. These simulations were initialized using a steady-flow solution defined by the surface recharge rate of 100 mm/yr and a hydraulic gradient in the unconfined aquifer. Plot-file output for these simulations was generated at the years 2000, 2010, 2040, 2540, and 3000 and include values for the aqueous saturation, aqueous pressure, aqueous moisture content, and concentrations for the four solute species. The moisture content field for these simulations remains unchanged from the initial steady-flow field until the year 2040, when the closure barrier becomes effective. This set of simulations was performed to investigate the sensitivity of the Case 1 results to moderate variations in the inventory distribution.

Solute BTCs at the first compliance point for the three cross-sections (S-CC', SX-DD', and SX-FF') are shown in Attachment E3, Figures E3.166 through E3.174 for the three solute species (technetium-99, chromium, and nitrate), respectively. Aqueous flux at the water table for the three cross-sections (S-CC', SX-DD', and SX-FF') are shown in Figures E3.175 through E3.177, respectively. Times and aqueous concentrations for the BTC peaks at the first compliance boundary are shown in Table E.29. Area-weighted averages (across the three cross-sections) of the solute BTCs were generated for the three solute species, as shown in Attachment E3, Figures E3.178 through E3.180 for technetium-99, chromium, and nitrate, respectively. When peak arrival concentration was weighted by maximum initial concentration, the breakthrough concentrations of the alternate distribution varied from those for the uniform distribution (i.e., Case 1 simulation) by 9.7 to 81.6%, depending on the solute. The results provide an indication of variations in peak arrival concentrations with uncertainty in the areal location of the initial inventory.

Table E.29. Peak Concentrations and Arrival Times at the First Compliance Point (i.e., WMA S-SX Boundary) for Case 12

Parameter	S-CC'	SX-DD'	SX-FF'
Tc-99			
Arrival Time	2032.3 yr	2050.3 yr	2032.6 yr
Peak Conc.	1.346×10^5 pCi/L	5.857×10^5 pCi/L	3.132×10^5 pCi/L
Max. Initial Conc.*	3.959×10^6 pCi/L	3.463×10^7 pCi/L	7.515×10^6 pCi/L
Cr			
Arrival Time	2050.7 yr	2052.7 yr	2051.3 yr
Peak Conc.	2.661×10^3 µg/L	4.453×10^4 µg/L	3.829×10^3 µg/L
Max. Initial Conc.	1.107×10^5 µg/L	1.847×10^6 µg/L	1.220×10^5 µg/L
NO₃			
Arrival Time	2031.9 yr	2050.3 yr	2031.3 yr
Peak Conc.	5.988×10^5 µg/L	8.148×10^5 µg/L	5.137×10^5 µg/L
Max. Initial Conc.	1.714×10^7 µg/L	3.678×10^7 µg/L	1.173×10^7 µg/L

*Maximum initial concentration is based on inventory data (Section E.2.4.3) and listed for comparison with the simulated peak concentration at the compliance boundary.

E.4.13 NO BARRIER AND 200,000 GAL WATER-LINE LEAK CASE (CASE 13)

The no barrier and 200,000 gal water-line leak suite of simulations, Case 13, investigated solute transport through one cross-section considering natural surface infiltration and a closure barrier by the year 2040. This suite of simulations differs from the Case 1 simulations in that a water-line leak occurs for tank SX-115 in cross-section SX-FF'. The water-line leak was modeled as a point source of water (200,000 gal over a 5-day period) spread over a 15 ft radius between tanks SX-114 and SX-115. The 15 ft radius leak area was translated to the two-dimensional simulation by using a computational grid width of 1 ft and assuming that the center of the circular leak area was situated on the center line between tanks. This approach results in a two-dimensional water-line leak of 8,488 gal over a 5-day period. These simulations were initialized using a steady-flow solution defined by the surface recharge rate of 100 mm/yr and a hydraulic gradient in the unconfined aquifer. Inventories of the four contaminant species were initialized using the uniform distribution pattern. Plot-file output for these simulations was generated at the years 2000, 2000.0137, 2000.0274, 2000.0685, 2000.137, 2000.5, 2001, 2040, 2540, and 3000 and include values for the aqueous saturation, aqueous pressure, aqueous moisture content, and concentrations for the four solute species.

The flow environment following the leak event is shown in a series of color-scaled images of aqueous saturation at 5, 10, 25, 50, 183, and 365 days after the leak in Figures E.23 through E.28, respectively. After 5 days (Figure E.23), the 200,000 gal leak has completely saturated the backfill material between tanks SX-114 and SX-115, with a portion of the saturated zone extending above the tank dome and below the tank bottom. After 10 days (Figure E.24), the

leak-water has descended into the coarser grained gravelly-sand strata. At 25 and 50 days (Figures E.25 and E.26), the leak has passed through and migrated along the gravelly-sand strata, crossed the tanks SX-114 and SX-115 domes, and started to form perched water above the Plio-Pleistocene strata. Between 50 days and 1 year (Figures E.27 and E.28), the leak plume descended through the Plio-Pleistocene strata, reached the groundwater, and formed two auxiliary plumes from the leak water that crossed the tank domes. After one year, the saturation field had not returned to steady-flow conditions (Figure E.28). This result differs from the 25,000 gal leak, where the saturation field had returned to steady-flow conditions after 1 year.

Figure E.23. Case 13 Aqueous-Phase Saturation at 2000 plus 5 days for Cross-Section SX-FF'

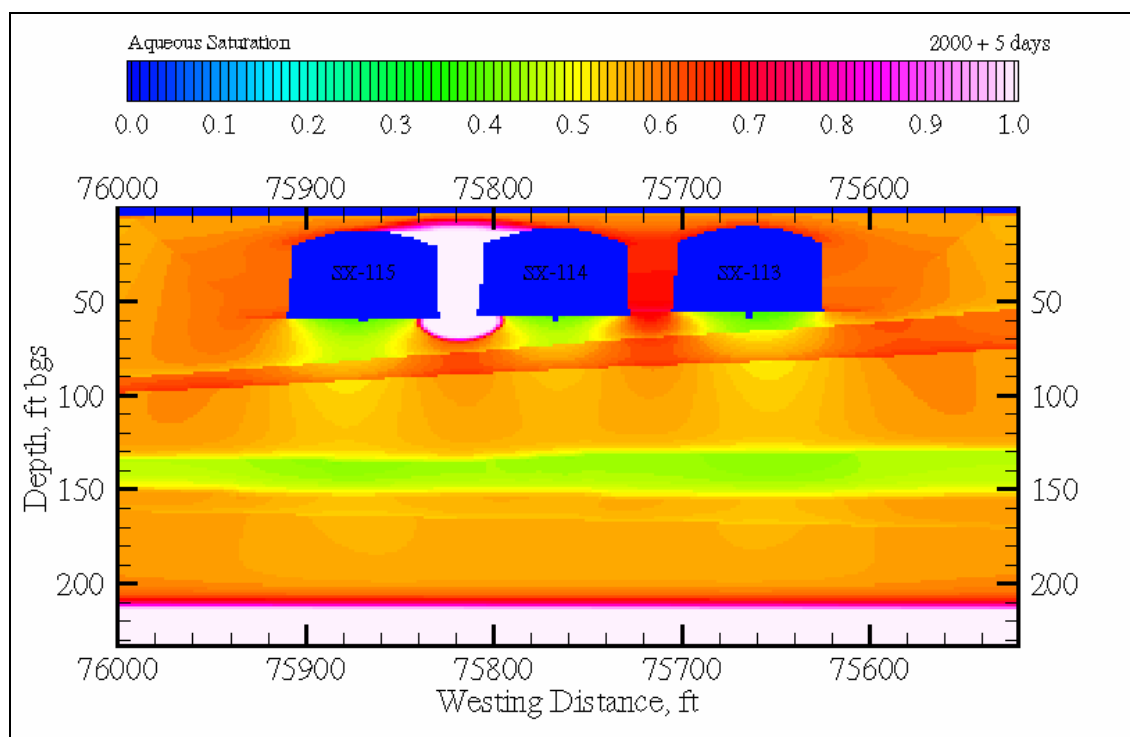


**Figure E.24. Case 13 Aqueous-Phase Saturation at
2000 plus 10 days for Cross-Section SX-FF'**

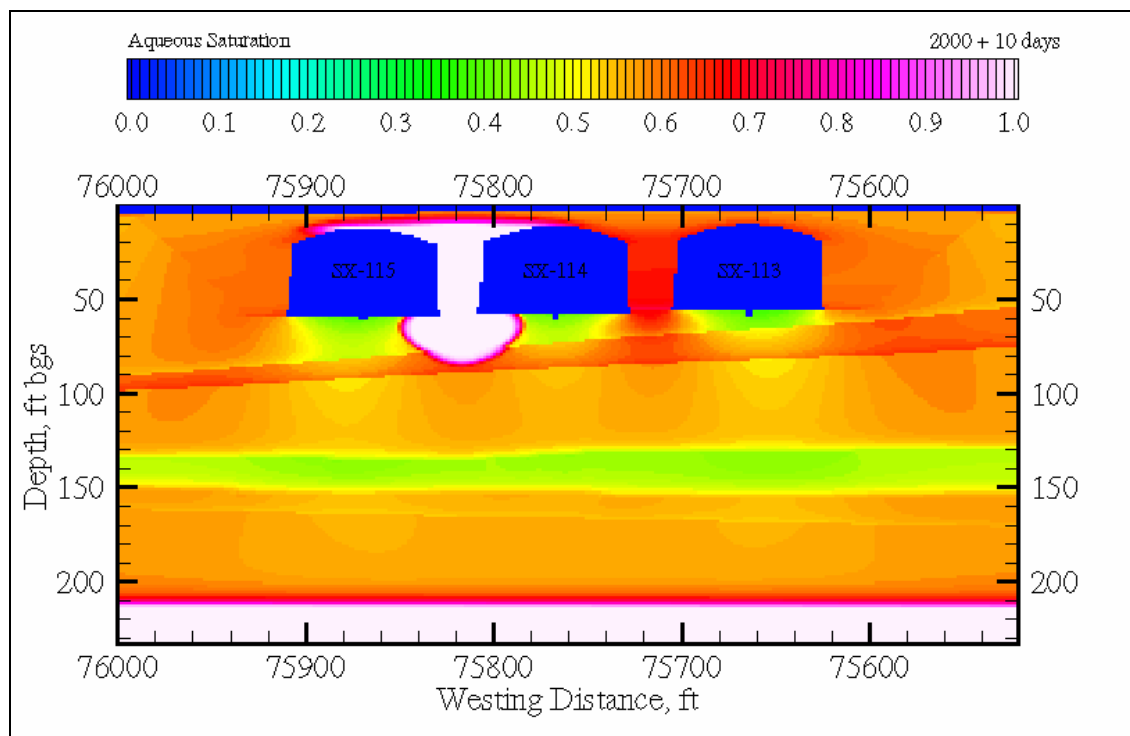


**Figure E.25. Case 13 Aqueous-Phase Saturation at
2000 plus 25 days for Cross-Section SX-FF'**

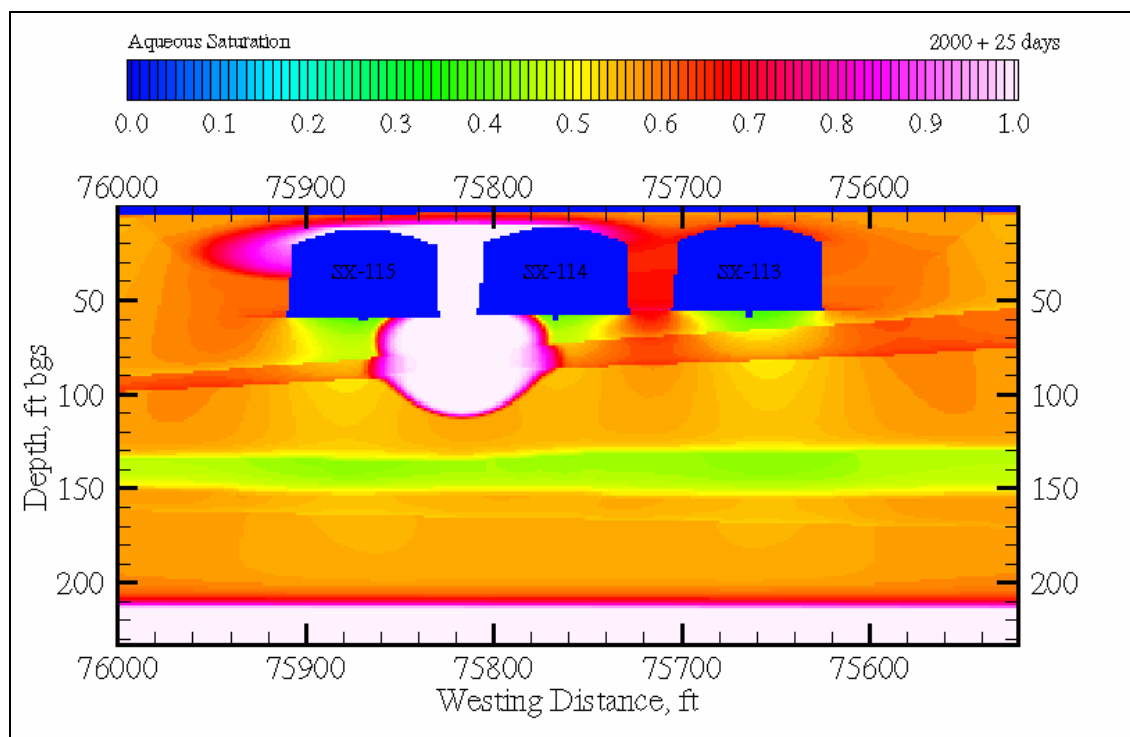


Figure E.26. Case 13 Aqueous-Phase Saturation at 2000 plus 50 days for Cross-Section SX-FF'

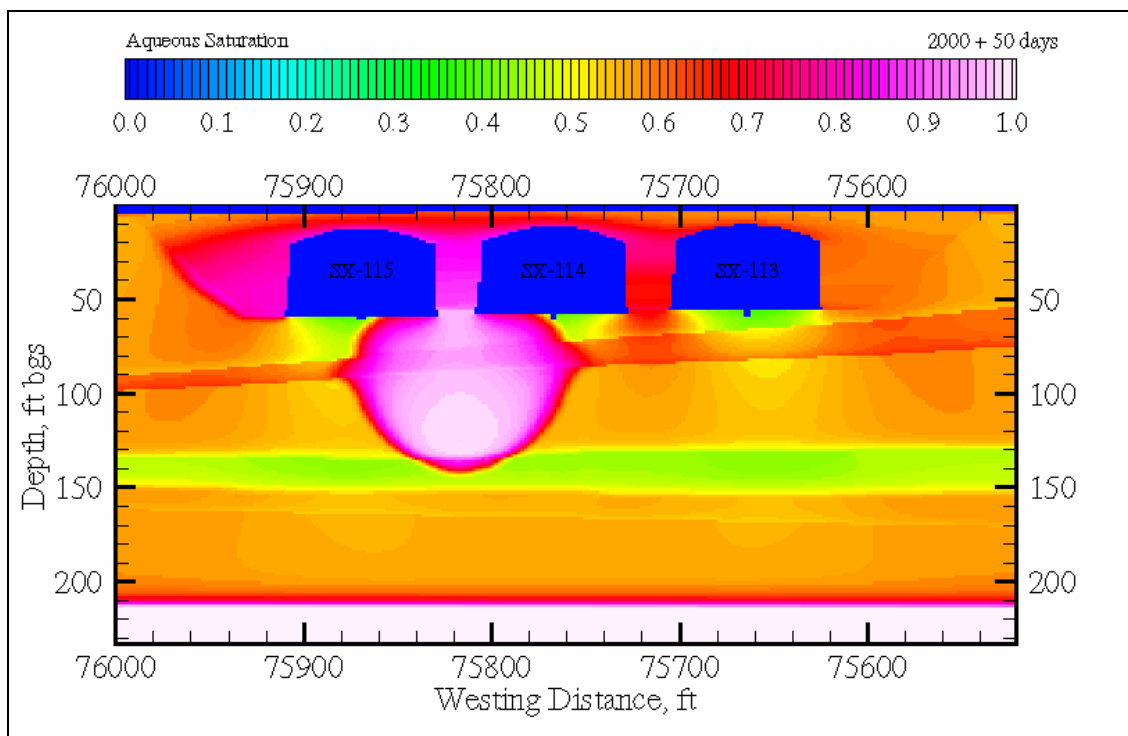


Figure E.27. Case 13 Aqueous-Phase Saturation at 2000 plus 183 days for Cross-Section SX-FF'

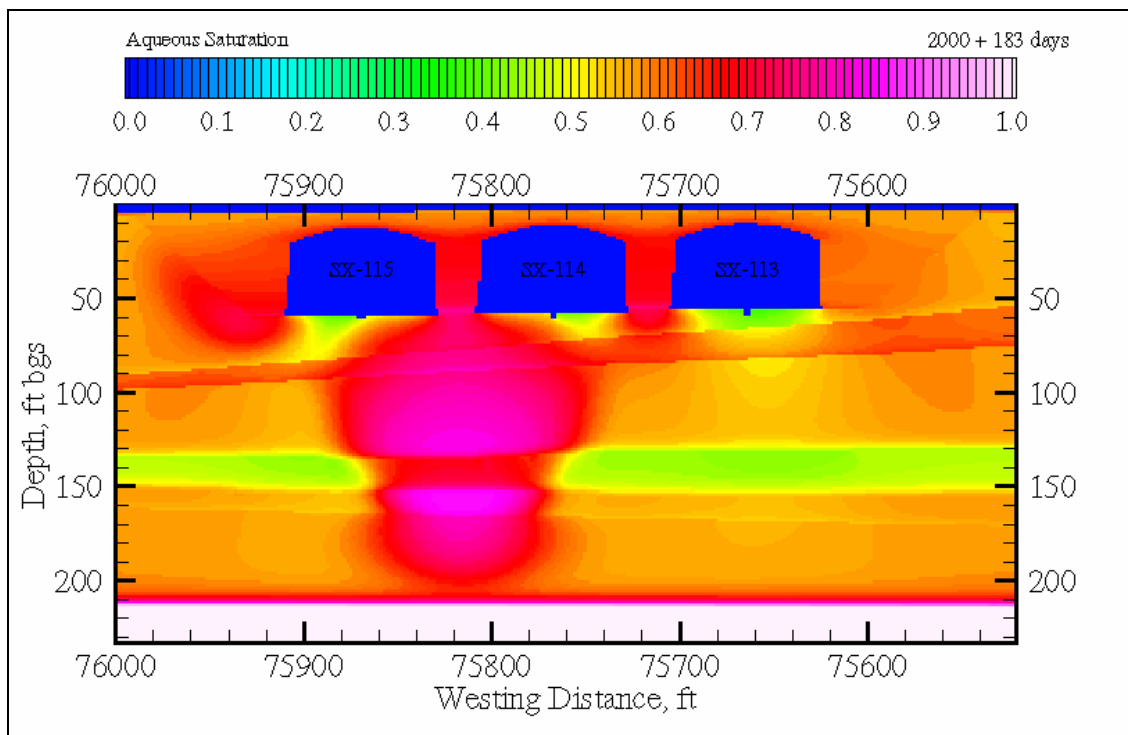
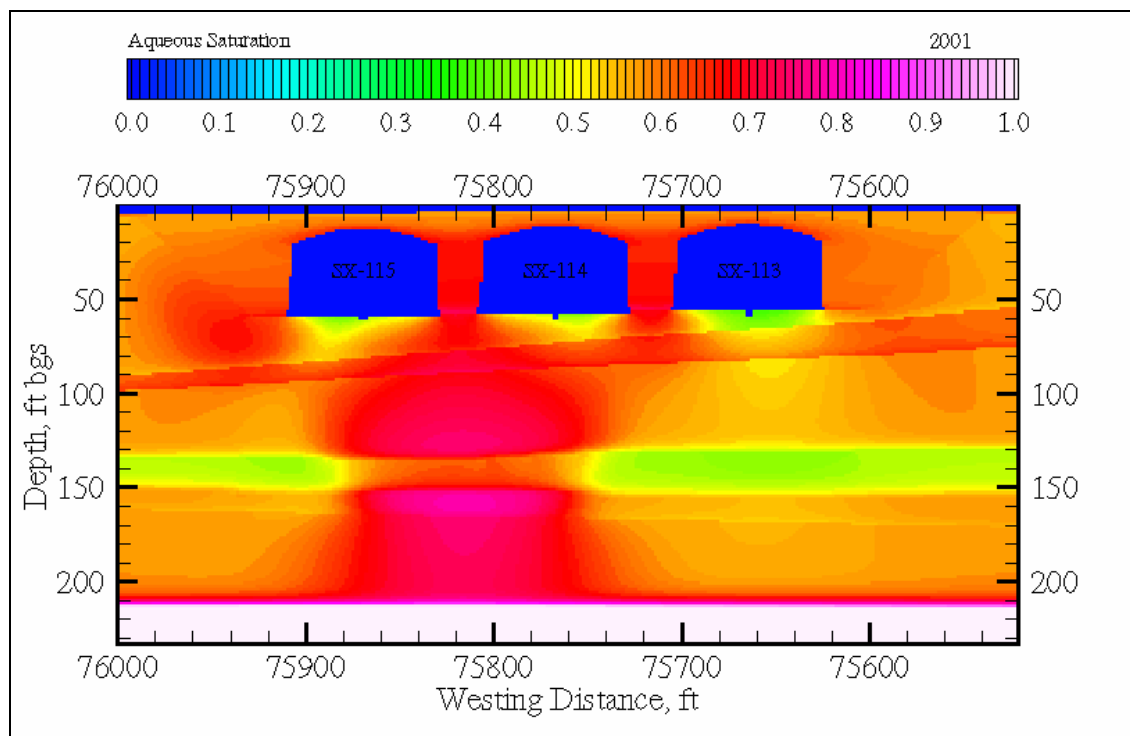


Figure E.28. Case 13 Aqueous-Phase Saturation at 2000 plus 365 days for Cross-Section SX-FF'



Solute BTCs at the first compliance point for cross-section SX-FF' are shown in Attachment E3, Figures E3.187 through E3.189 for the three solute species (technetium-99, chromium, and nitrate), respectively. BTCs for cross-sections S-CC' and SX-DD' are shown in Figures E3.181 through E3.186. Aqueous fluxes at the water table for the three cross-sections are shown in Figures E3.190 through E3.192. Peak concentrations and arrival times for the BTCs at the first compliance boundary are shown in Table E.30. Area-weighted averages of the solute BTCs were generated for the three solute species and are shown in Attachment E3, Figures E3.193 through E3.195 for technetium-99, chromium, and nitrate, respectively. The saturation fields (Figures E.23 through E.28) showed saturation around the tank domes and the leak plumes rapidly descending through various strata. However, the BTCs at the WMA S-SX boundary suggest only slight differences in shapes and arrival concentrations (Attachment E3, Figures E3.187 through E3.189). Arrival times for the solutes in cross-section SX-FF' were advanced by approximately three years, but the peak concentrations were decreased, compared against the Case 1 and Case 3. Decreases in peak concentrations were a direct result of dilution due to the leak event.

Table E.30. Peak Concentrations and Arrival Times at the First Compliance Point (i.e., WMA S-SX Boundary) for Case 13

Parameter	SX-FF'
Tc-99	
Arrival Time	2027.5 yr
Peak Conc.	2.445×10^5 pCi/L
Max. Initial Conc.*	5.074×10^6 pCi/L
Cr	
Arrival Time	2049.3 yr
Peak Conc.	4.323×10^3 µg/L
Max. Initial Conc.	1.089×10^5 µg/L
NO ₃	
Arrival Time	2028.5 yr
Peak Conc.	9.522×10^5 µg/L
Max. Initial Conc.	3.616×10^7 µg/L

*Maximum initial concentration is based on inventory data (Section E.2.4.3) and listed for comparison with the simulated peak concentration at the compliance boundary.

The impact on the transport of contaminants of the 200,000 gal leak event is shown by comparing the distribution of technetium-99 at 2001 and 2040 (Figures E.29 and E.30). By 2001, the technetium-99 concentration field has been deformed toward the water table within the leak-plume column. This deformation alters the shape of the BTC (Attachment E3, Figure E3.187), but the undisturbed regions of the technetium-99 plume, outside of the leak-plume column, descend in response to the rate of meteoric recharge over a 40-year period. The similarity in technetium-99 plumes for 2040 below tanks SX-113 and SX-115 (Figure E.30) shows this effect.

Figure E.29. Case 13 Technetium-99 Aqueous Concentration at 2001 for Cross-Section SX-FF'

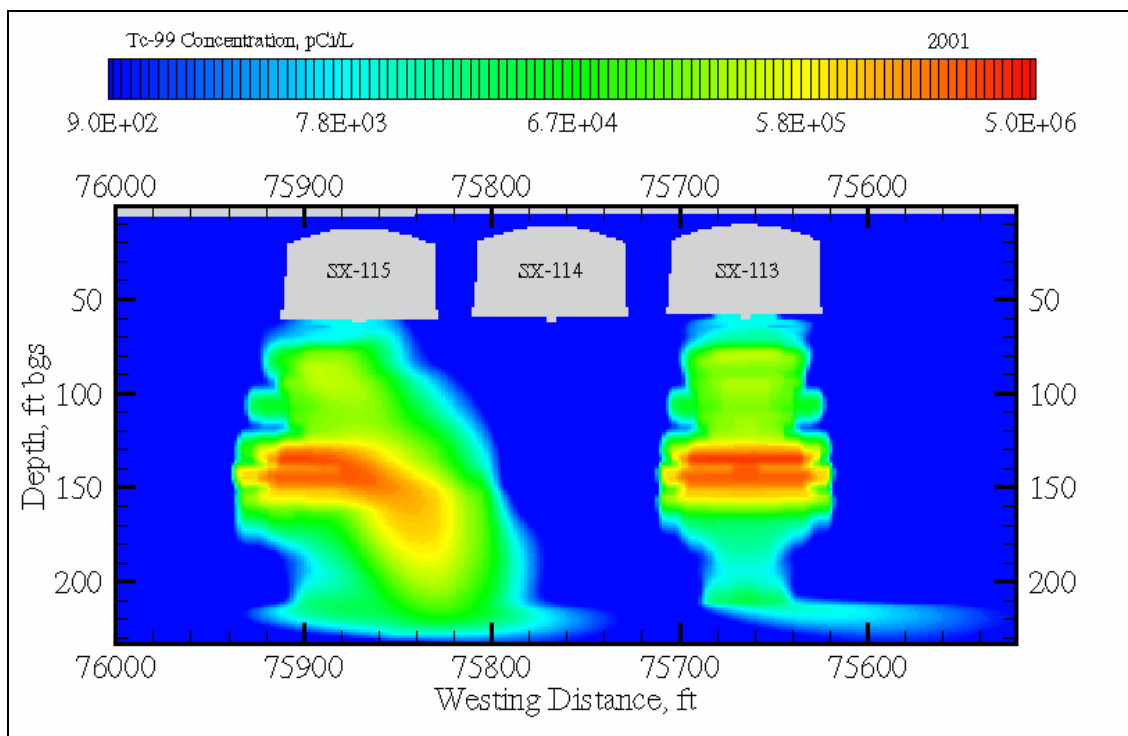
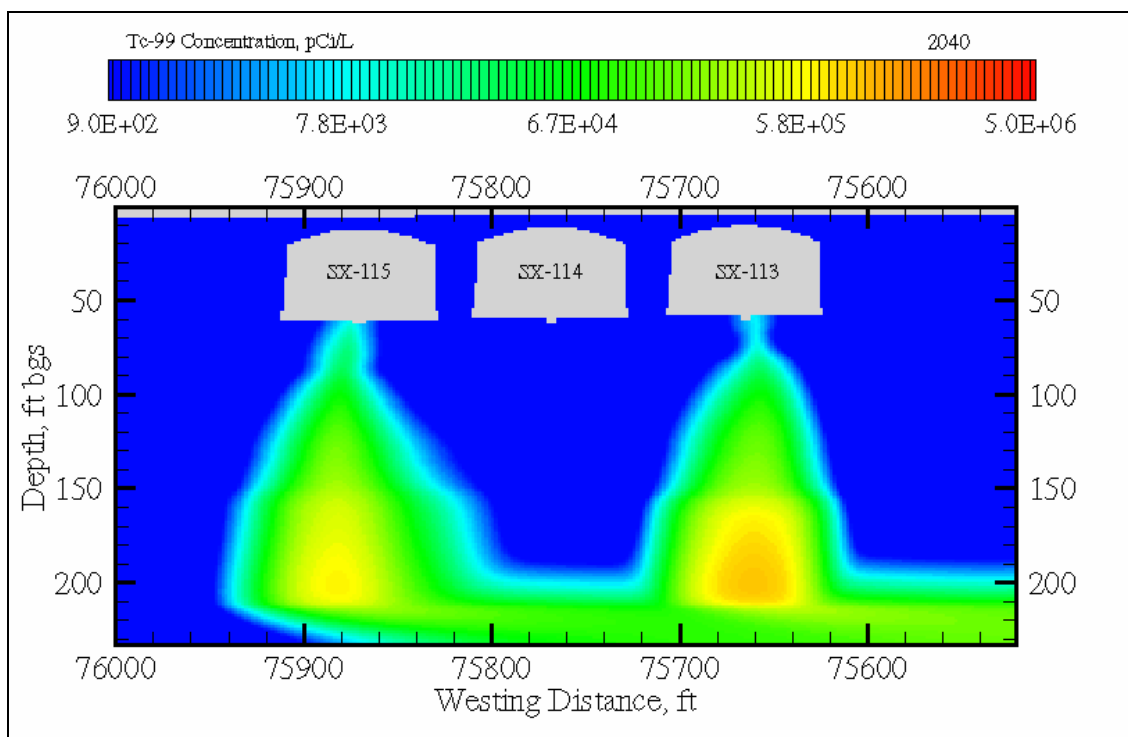


Figure E.30. Case 13 Technetium-99 Aqueous Concentration at 2040 for Cross-Section SX-FF'



E.4.14 THREE-DIMENSIONAL SIMULATIONS

The objective of this suite of simulations is to determine the differences in results between the simulations constrained along a two-dimensional cross-section compared to the results of a simulation extended to three dimensions. Specifically, the two-dimensional cross-section simulations are along the maximum diameter of the rows of tanks, focusing the recharge over the cross-section within the most narrow zones between the tanks.

A three-dimensional simulation was constructed from a one-quarter section around tank SX-108 (Attachment E3, Figure E3.196). The geology around the tank (from east/west cross-section SX-DD' in the x and z directions) and inventory were duplicated and extended toward the north (i.e., y-direction). The radial extent of the cross-section extends to the midpoint between tanks SX-108 and SX-109 to the west and between tank SX-105 to the north. Attachment E3, Figure E3.197 shows the zonations along the southern-most y-plane, which has the maximum radius of the tank (i.e., the same plane used in the two-dimensional simulations). Transient simulations were conducted using the inventory and recharge rates from Case 1 with the three-dimensional domain and with a two-dimensional domain along the southern-most y-plane for direct comparison of results. The tank SX-108 three-dimensional simulation domain consisted of 119,422 nodes ($x,y,z = 29 \times 29 \times 142$ nodes). Within this domain, approximately 12,000 nodes were inactive, representing the tank itself. The three-dimensional simulation execution time was approximately 5 days for a 1,000-year simulation (0.333 year time step) running on a 600-Mhz Pentium II processor with 256 MB RAM.

Attachment E3, Figure E3.198 shows the steady-flow volumetric water flux vectors in the x-z directions for three y-planes (front, middle, and back) within the three-dimensional domain from the 100 mm/yr recharge rate used for the first 40 years. These vectors illustrate the umbrella-effect of the tanks, where the recharge sheds from the top of the tank. The highest water fluxes occur in the thinnest zone on the front plane (i.e., $y=1$). Directly below the tank, the vectors show water moving back under the tank. Variations in the water fluxes near the tanks are dampened out towards the bottom of the domain resulting in a relatively uniform flow field in the lower half. The impact of the geology is also illustrated in Figure E3.198 where the vectors are refracted from the sloping bottom contact of Unit 3 (gravelly sand/sandy gravel) at a depth of 24.4 to 30.5 m (80 to 100 ft) below ground surface. Volumetric water fluxes are shown in the x-y directions at 4 different depths (z-planes) around the tanks in Figures E3.199 and E3.200. These figures show relatively high water fluxes in the x-y direction moving away from the tanks across upper dome (Figure E3.199) and moving back under the tanks below the bottom (Figure E3.200). At depths between the upper dome and bottom of the tank, water fluxes are dominantly vertical (z-direction) and very low in the x-y plane (see Figures E3.199 and E3.200).

Figure E3.201 shows the aqueous saturation along three different planes (front, middle, and back) in the y-direction at the beginning of the simulation (i.e., year 2000 with 100 mm/yr recharge). The impact of the tank on aqueous saturations can still be seen on the back (northern-most) y plane, which is 3 m (10 ft) north of the edge of the tank. Figure E3.202 shows the results of the technetium-99 plume along three y-planes by year 2040 (compare to initial conditions in Figure E3.197). Figure E3.203 shows a comparison of the technetium-99 mass fluxes at the bottom of the domain for nodes on the east, center, and west of the two y-planes on

the north and south of the domain ($y=1$ and $y=29$). No variation was seen in the water fluxes for these nodes.

A comparison of the water and technetium-99 fluxes at the bottom of the simulation domain between the three-dimensional tank SX-108 and two-dimensional tank SX-108 simulations is shown in Figures E3.204 and E3.205. These figures compare the two-dimensional simulation results with the three-dimensional results from the front plane and the average over the entire three-dimensional domain. These data were scaled to unit widths. The results show little difference between the water fluxes over the 1,000-year duration of these simulations (Figure E3.204). While the simulated mass fluxes were similar overall, the peak technetium-99 mass fluxes (around year 2050) were slightly higher in the three-dimensional simulation than for the two-dimensional simulation. The peak technetium-99 mass flux for the front plane ($y=1$) of the three-dimensional simulation was also slightly higher than the mass flux average for the entire three-dimensional domain.

E.4.15 SOLUTE MASS BALANCE

Mass balance checks were performed on the non-decaying solutes (i.e., nitrate and chromium) for each combination of simulation case and cross-section, using Equation E.18.

$$m_{error} = \frac{m_{initial} - m_{final} - m_{exiting}}{m_{initial}} \quad (E.18)$$

where:

m_{error} = mass balance error, expressed in percent

$m_{initial}$ = initial solute inventory computed from the STOMP plot-file output at the year 2000

m_{final} = final solute inventory computed from the STOMP plot-file output at the year 3000

$m_{exiting}$ = integrated solute inventory leaving the computation domain, computed from the STOMP surface-flux output.

Initial and final solute masses were computed using a two-step process: (1) STOMP plot-file outputs were converted to two-dimensional Tecplot format using the utility PlotTec; (2) solute mass was integrated using the Tecplot statistical tools package. The solute mass leaving the computational domain through the groundwater was determined using surface-flux output, defined for the western surfaces below the water table. The surface-flux output provided both the solute-flux rate and integral. Other than solving the solute mass conservation equations, the STOMP simulator contains no algorithms for correcting local or global mass. Therefore, mass balance errors, reported below represent the actual mass balance errors from the conservation equations. Mass balance errors, expressed as percent error, are shown in Table E.31 for the non-decaying species nitrate and chromium. The average mass balance error for the simulations without concentration dependent density and viscosity was $1.90 \times 10^{-5} \%$ and for those simulations with concentration dependent density and viscosity was $5.48 \times 10^{-2} \%$. The simulations with concentration dependent density and viscosity showed higher mass balance errors, because of the loose coupling between the aqueous-phase flow properties and the solute

concentrations. This level of error in the conservation of solute mass, indicates that a fully coupled solution approach was not needed for the investigated simulations.

Table E.31. Solute Mass Balance Errors

m_{error}	Cross-Section S-CC'		Cross-Section SX-DD'		Cross-Section SX-FF'	
	Cr	NO ₃	Cr	NO ₃	Cr	NO ₃
Case 1	4.75×10^{-6}	5.52×10^{-6}	1.48×10^{-5}	3.94×10^{-6}	3.65×10^{-7}	5.69×10^{-6}
Case 2	1.33×10^{-5}	1.68×10^{-5}	2.06×10^{-7}	1.09×10^{-5}	5.33×10^{-6}	1.29×10^{-5}
Case 3	4.75×10^{-6}	5.52×10^{-6}	1.48×10^{-5}	3.94×10^{-6}	1.39×10^{-5}	5.76×10^{-6}
Case 5	3.03×10^{-5}	1.01×10^{-5}	4.03×10^{-5}	3.25×10^{-5}	5.94×10^{-5}	4.13×10^{-6}
Case 6	2.97×10^{-7}	2.18×10^{-5}	2.91×10^{-5}	4.49×10^{-5}	2.87×10^{-5}	1.12×10^{-5}
Case 7	6.65×10^{-5}	1.41×10^{-5}	4.03×10^{-5}	3.21×10^{-5}	1.32×10^{-5}	1.11×10^{-5}
Case 8	4.56×10^{-2}	2.19×10^{-2}	9.83×10^{-2}	9.04×10^{-2}	5.06×10^{-2}	2.20×10^{-2}
Case 9	2.46×10^{-7}	1.80×10^{-5}	2.07×10^{-5}	4.32×10^{-6}	4.32×10^{-5}	2.44×10^{-5}
Case 10	1.77×10^{-6}	2.23×10^{-5}	5.89×10^{-5}	3.76×10^{-6}	2.02×10^{-5}	1.42×10^{-5}
Case 11	9.80×10^{-6}	4.78×10^{-6}	1.95×10^{-4}	1.79×10^{-5}	5.23×10^{-5}	8.15×10^{-6}
Case 12	4.56×10^{-6}	1.05×10^{-5}	1.57×10^{-5}	1.05×10^{-5}	1.97×10^{-5}	3.28×10^{-6}
Case 13	4.75×10^{-6}	5.52×10^{-6}	1.48×10^{-5}	3.94×10^{-6}	1.12×10^{-6}	4.12×10^{-6}

E.5.0 STREAMTUBE MODELING RESULTS

An analytical streamtube model was used to route the simulated WMA S-SX average concentrations for each case to three compliance locations: 200 West Area fence, 200 Area exclusion boundary (located approximately 1.25 km [0.78 mi] east of the 200 East Area), and the Columbia River. The analytic streamtube model was based on an approach described by Baetsle (1969), as documented in Freeze and Cherry (1979). The streamtube model assumes transport from a point source, represented by a series of solute slugs, and considers longitudinal, lateral, and transverse vertical dispersion; molecular diffusion; and first order decay. The method of superposition was used to integrate the individual slug sources.

Distances and travel times from WMA S-SX to the three compliance points were derived from steady-state VAM3D unconfined aquifer flow simulations of the Hanford Site (Lu 1996). The simulation results represent ‘post-Hanford’ or future conditions representing the water table at the Site without the additional impact of any unconfined aquifer discharges. Results of the VAM3D simulated hydraulic heads and streamlines are shown in Figures E.5 and E.6; these figures are based on Lu (1996). Two streamlines from Figure E.6 starting at S tank farm and SX tank farm were used to determine the unconfined aquifer path length to the three compliance points. Travel markers indicating 20-year intervals on the streamlines were used to estimate the travel time to the three compliance points. The two streamlines (for S and SX tank farms) had similar lengths and travel times to the compliance points, resulting in only one estimate for WMA S-SX (see Table E.32). Both of these streamlines move roughly east from WMA S-SX toward the Columbia River on the south side of Gable Mountain. Other groundwater flow simulations of the Hanford Site have shown the potential for a different pathline from WMA S-SX that goes northward through the Gable Mountain/Gable Butte gap. These pathlines were not considered in this analysis.

Table E.32. Distances and Travel Times from WMA S-SX

Compliance Point	Distance (mi)	Time (yrs)
200 West fence	1.12	140
Exclusion Boundary	6.52	300
Columbia River Shoreline	14.0	500

Note: Derived from flow lines and 20-year travel markers from post-Hanford simulation (Section E.2.3.1).

Given the large variation in groundwater velocities between the three compliance points (see Table E.33), three streamtubes were constructed representing the aquifer between WMA S-SX and each compliance point. Solute mass flux across WMA S-SX boundary was a composite of the simulated aquifer outlet mass fluxes from the S-CC', SX-DD', and SX-FF' cross-sections and was converted into slugs of mass as input to the analytical streamtube model. Groundwater velocities for each streamtube are constant.

Table E.33. Streamtube Characteristics

From	To	Distance (mi)	Velocity (ft/day)
WMA S-SX	200 West fence	1.12	0.116
200 West fence	Exclusion boundary	5.40	0.488
Exclusion boundary	Columbia River	7.48	0.541

A FORTRAN program was written to implement the mass flux conversion to time varying solute slugs, the analytical solution of Baetsle (1969), and superpositioning of the time-varying mass fluxes. The BTCs for each case and each species (i.e., technetium-99, chromium, and nitrate) were calculated from the streamtube for each compliance boundary, using the FORTRAN program.

The two-dimensional transport simulations (Section E.3.0) yielded solute mass flux and concentration at the WMA S-SX boundary along the tank centerlines for the three cross-sections (S-CC', SX-DD', and SX-FF'), as shown in Figure E.31. Translation of the centerline solute mass flux or concentration to an average value across the WMA boundary was computed using two translations. In the first translation, the centerline quantities are converted to average quantities on the WMA boundary line within the regions shown in Figure E.31 as the cross-section projections. The length of the cross-section projection equals the mean inventory diameter, where the mean inventory diameter was computed for each combination of solute specie and concentration, as described in the inventory section (Section E.2.4.3). As shown graphically in Figure E.31, the mean inventory diameter is *not* the tank diameter.

Off centerline solute mass flux and concentration are computed by assuming the concentration distribution shown in Equation E.19.

$$C_{\ell}(x) = \hat{C}_{\ell} \frac{l_c(x)}{\langle D \rangle} = \hat{C}_{\ell} \frac{\sqrt{\langle D \rangle^2 - 4x^2}}{\langle D \rangle} \quad (\text{E.19})$$

where:

$C_{\ell}(x)$ = solute mass flux or concentration as a function of distance x along the WMA boundary

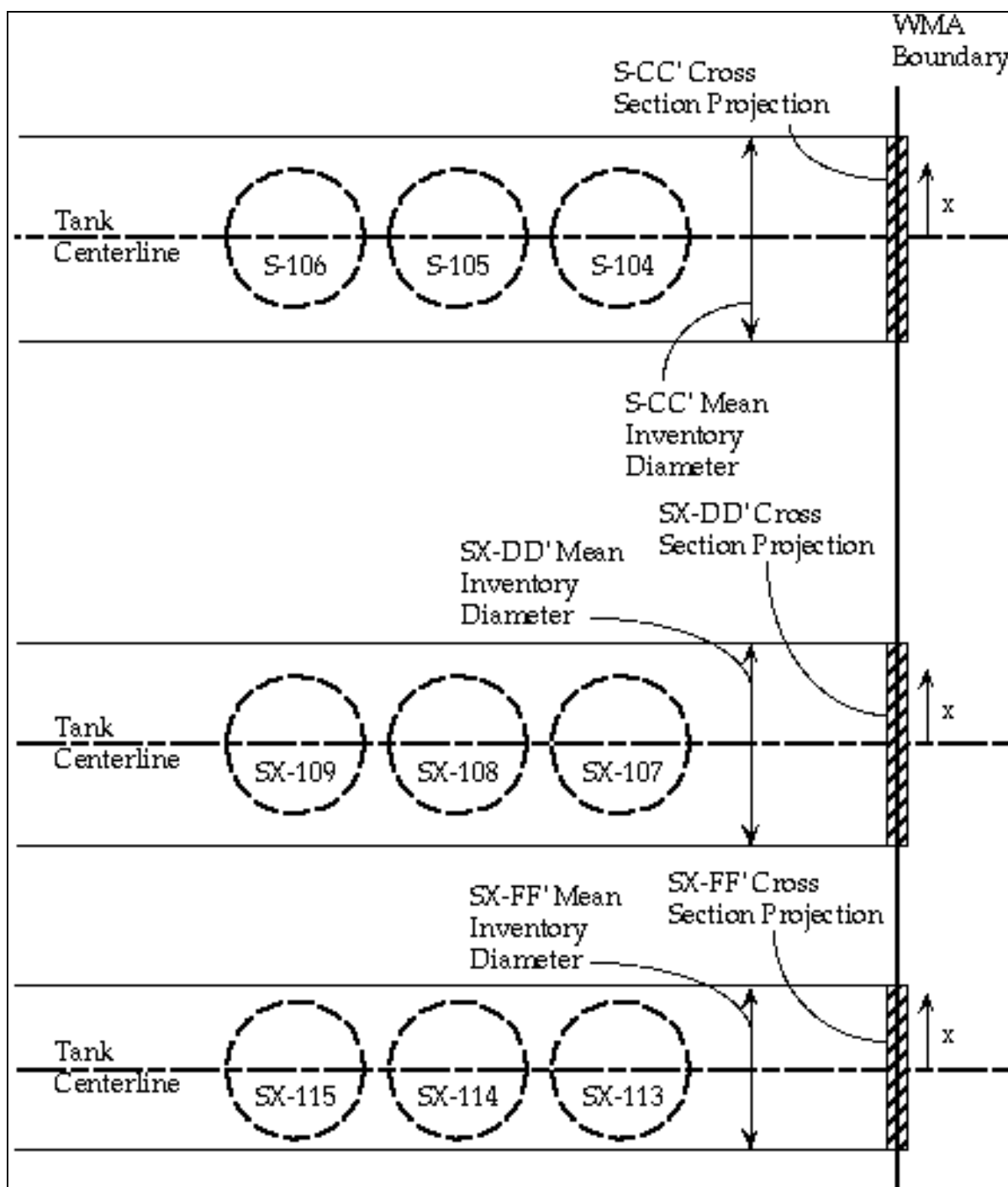
\hat{C}_{ℓ} = tank centerline solute mass flux or concentration

$l_c(x)$ = chord length across the mean inventory circle as a function of distance x along the WMA boundary

$\langle D \rangle$ = mean inventory diameter

x = distance from the tank centerline along the WMA boundary.

Figure E.31. Translation Geometry



The average solute mass flux or concentration is computed by integrating Equation E.19, as shown in Equation E.20.

$$\tilde{C}_\ell = \hat{C}_\ell \int_0^{\langle D \rangle/2} \frac{2\sqrt{\langle D \rangle^2 - 4x^2}}{\langle D \rangle^2} dx = \hat{C}_\ell \frac{\pi}{4} \quad (\text{E.20})$$

where:

\tilde{C}_ℓ = average solute mass flux or concentration along the WMA boundary within the cross-section projection.

An average solute mass flux or concentration is computed according to Equation E.20 for the three cross-sections (i.e., $\tilde{C}_\ell^{scc'}$ for S-CC', $\tilde{C}_\ell^{sxdd'}$ for SX-DD', and $\tilde{C}_\ell^{sxff'}$ for SX-FF').

The three cross-sectional average solute mass fluxes or concentrations are translated to a single average solute mass flux or concentration for the entire WMA S-SX boundary length using length-weighted averaging according to Equation E.21.

$$\bar{C}_\ell = \sum_{i=scc', sxdd', sxff'} \frac{\langle D^i \rangle}{L_{WMA}} \tilde{C}_\ell^i \quad (\text{E.21})$$

where:

\bar{C}_ℓ = average solute mass flux or concentration for the WMA boundary

$\langle D^i \rangle$ = mean inventory diameter for cross-section i

L_{WMA} = north-south length of the WMA S-SX boundary.

Results of the streamtube analyses are summarized in Tables E.34 through E.36, showing the peak time (year) and peak concentration for each case and compliance location, for the three species (technetium-99, chromium, and nitrate), respectively. Peak concentrations and times are a direct result of the superposition of mass fluxes from cross-sections S-CC', SX-DD', and SX-FF' averaged over the fence-line of the WMA.

Table E.34. Streamtube Analysis Summary for Technetium-99

Tc-99 Conc.	WMA S-SX		200 West fence		Exclusion Boundary		Columbia River	
(pCi/L)	Time	Conc.	Time	Conc.	(pCi/L)	Time	Conc.	Time
Case 1	2046	6.85E+04	2181	4.89E+03	2344	3.80E+02	2545	1.28E+02
Case 2	2030	2.90E+04	2179	1.91E+03	2341	1.47E+02	2543	5.11E+01
Case 3	2046	6.74E+04	2180	4.89E+03	2344	3.79E+02	2545	1.29E+02
Case 4	2046	6.83E+04	2181	4.89E+03	2344	3.79E+02	2545	1.28E+02
Case 5	2044	7.49E+04	2179	5.29E+03	2342	4.11E+02	2543	1.39E+02
Case 6	2029	3.44E+04	2178	2.09E+03	2340	1.62E+02	2542	5.61E+01
Case 7	2011	1.71E+05	2149	6.89E+03	2314	5.42E+02	2514	1.78E+02
Case 8	2046	6.92E+04	2180	4.96E+03	2344	3.85E+02	2545	1.30E+02
Case 9	2061	3.53E+04	2203	2.50E+03	2365	1.91E+02	2567	6.67E+01
Case 10	2075	1.74E+04	2223	1.32E+03	2384	9.97E+01	2586	3.54E+01
Case 11	3000*	4.34E+03	2312	3.08E+02	2471	2.26E+01	2673	8.28E+00
Case 12	2046	6.87E+04	2180	4.95E+03	2344	3.84E+02	2545	1.30E+02
Case 13	2047	6.31E+04	2179	4.76E+03	2342	3.68E+02	2543	1.25E+02

Note: Groundwater limit 900 pCi/L.

*Peak concentrations arrive after year 3000.

Table E.35. Streamtube Analysis Summary for Chromium

Cr Conc.	WMA S-SX		200 West fence		Exclusion Boundary		Columbia River	
(µg/L)	Time	Conc.	Time	Conc.	(µg/L)	Time	Conc.	Time
Case 1	2052	7.33E+03	2191	4.49E+02	2354	3.49E+01	2556	1.19E+01
Case 2	2057	1.02E+03	2210	8.55E+01	2370	6.44E+00	2573	2.31E+00
Case 3	2052	7.34E+03	2191	4.52E+02	2354	3.51E+01	2555	1.20E+01
Case 4	2052	7.30E+03	2191	4.47E+02	2354	3.48E+01	2556	1.18E+01
Case 5	2051	8.71E+03	2188	5.23E+02	2351	4.08E+01	2552	1.38E+01
Case 6	2051	1.29E+03	2205	1.03E+02	2365	7.76E+00	2568	2.77E+00
Case 7	2017	1.49E+04	2157	7.78E+02	2321	6.09E+01	2522	2.02E+01
Case 8	2052	7.42E+03	2191	4.55E+02	2354	3.54E+01	2555	1.20E+01
Case 9	2074	2.04E+03	2226	1.54E+02	2386	1.17E+01	2589	4.14E+00
Case 10	2119	6.38E+02	2272	5.55E+01	2430	4.11E+00	2632	1.50E+00
Case 11	3000*	3.86E+02	3000*	7.27E+00	2771	5.13E-01	2972	1.89E-01
Case 12	2052	7.28E+03	2191	4.51E+02	2354	3.51E+01	2555	1.19E+01
Case 13	2052	7.20E+03	2189	4.55E+02	2353	3.53E+01	2554	1.20E+01

Note: Groundwater limit 50 µg/L.

*Peak concentrations arrive after year 3000.

Table E.36. Streamtube Analysis Summary for Nitrate

NO₃ Conc.	WMA S-SX		200 West fence		Exclusion Boundary		Columbia River	
(µg/L)	Time	Conc.	Time	Conc.	Time	Conc.	Time	Conc.
Case 1	2041	1.28E+05	2178	9.49E+03	2342	7.37E+02	2542	2.49E+02
Case 2	2029	6.88E+04	2177	4.31E+03	2339	3.34E+02	2541	1.15E+02
Case 3	2041	1.27E+05	2178	9.50E+03	2341	7.38E+02	2542	2.50E+02
Case 4	2041	1.28E+05	2178	9.46E+03	2342	7.35E+02	2542	2.49E+02
Case 5	2038	1.39E+05	2176	1.02E+04	2340	7.96E+02	2540	2.69E+02
Case 6	2027	8.41E+04	2175	4.81E+03	2337	3.73E+02	2539	1.29E+02
Case 7	2007	3.57E+05	2148	1.31E+04	2312	1.03E+03	2513	3.39E+02
Case 8	2041	1.29E+05	2178	9.61E+03	2341	7.47E+02	2542	2.52E+02
Case 9	2058	7.76E+04	2199	5.32E+03	2361	4.09E+02	2563	1.42E+02
Case 10	2074	4.12E+04	2221	3.04E+03	2382	2.31E+02	2584	8.17E+01
Case 11	2167	8.45E+03	2315	7.45E+02	2473	5.48E+01	2676	2.01E+01
Case 12	2039	1.28E+05	2177	9.63E+03	2340	7.48E+02	2541	2.53E+02
Case 13	2041	1.21E+05	2177	9.42E+03	2340	7.30E+02	2541	2.48E+02

Note: Groundwater limit 45,000 µg/L.

*Peak concentrations arrive after year 3000.

The first streamtube extended from the WMA boundary to the 200 West fence compliance boundary; peak concentrations at the 200 West fence generally decreased to less than 10% of the WMA boundary concentration. Those simulations with broader BTCs at the WMA boundary had lower percent decreases; whereas, those with sharper BTCs had greater percent decreases from longitudinal dispersion. The second streamtube extended from the 200 West fence to the 200 Area exclusion boundary. Again, the concentrations at the 200 Area exclusion boundary generally decreased to less than 10% of the 200 West fence boundary concentration. Results for the final streamtube (between the 200 Area exclusion boundary and Columbia River) showed the smallest decrease in peak concentrations for all the streamtubes, even though the residence time in this streamtube was the longest. The peak concentrations at the Columbia River boundary generally decreased to less than 40% of the 200 Area exclusion boundary concentration. The reason for the lower percentage decrease in concentrations for this streamtube is that the peak concentrations have already been significantly attenuated by the earlier two streamtubes resulting in larger and broader pulses. The increase in unconfined aquifer velocity accounted for most of the decrease in peak concentrations for this streamtube.

E.6.0 HUMAN HEALTH RISK AND DOSE RESULTS

This section presents the results of the human health risk and dose assessment. The risk and dose values presented are based on the groundwater concentrations generated through contaminant transport modeling (Sections E.1.0 and E.2.0) and were calculated using the approach described in Section E.3.0. Groundwater concentration values from cross-sections S-CC', SX-DD', and SX-FF' at the WMA S-SX boundary used Equation E.19 in Section E.5.0 to calculate the risk and dose values with the methodology described in Section E.3.0. Note that risk and dose results are presented only for a select group of simulation cases (Table E.37). Results for these cases are representative of the larger set of cases considered in the contaminant transport analysis and include information on the impacts associated with existing conditions (Case 1); interim barrier use (Case 2); and variable meteoric recharge rates (Cases 9, 10, 11). The remaining cases generally represent variations around the existing conditions or interim barrier cases and are not specifically discussed in this section because their impacts are of similar magnitude to either Case 1 or 2.

Table E.37. Human Health Risk and Dose Assessment Cases

Case	Description	Rationale
1	Base case (no action alternative)	Reference case. Estimation of impacts from past contaminant releases at WMA S-SX if no interim measures or interim corrective measures were implemented.
2	Barrier alternative and no water-line leaks	Interim corrective measure case. Estimation of degree to which implementation of an interim surface barrier would decrease impacts from past contaminant releases at WMA S-SX.
9	Base case with 50 mm/yr meteoric recharge	Meteoric recharge sensitivity cases. Estimation of degree to which meteoric recharge modeling assumptions affect estimated base case impacts from past contaminant releases at WMA S-SX.
10	Base case with 30 mm/yr meteoric recharge	
11	Base case with 10 mm/yr meteoric recharge	

WMA = waste management area.

Risk and dose results for the five cases shown in Table E.37 are presented individually in Sections E.6.1 to E.6.5. As discussed in Section E.3.1, multiple exposure scenarios are considered in this assessment to account for the uncertainty of long-term Hanford Site land use. To simplify the presentation, the individual case discussions focus on the results for the industrial worker scenario. Results for all the receptor scenarios are provided in table format for each case; however, for comparison purposes, a single scenario is sufficient because the relationship between the receptor scenarios remains relatively consistent within each case. For example, regardless of the case or compliance point, the peak residential farmer ILCR is always approximately 35 times higher than the peak industrial worker ILCR, and the MTCA Method B peak hazard index is always approximately 2.2 times higher than the MTCA Method C peak hazard index.

E.6.1 BASE CASE, NO ACTION ALTERNATIVE (CASE 1)

Results for the base case (Case 1) are summarized in Table E.38. Results for Case 1 reveal three general trends that are also evident in the results for the other cases considered (Cases 2, 9, 10, 11). First, peak values for the cross-sections at the WMA S-SX boundary exceed the peak values for the downgradient compliance points. Second, peak values at the WMA S-SX boundary are highest for cross-sections SX-DD' or SX-FF', followed by cross-section S-CC'. Third, peak values at the last compliance point (i.e., the Columbia River shoreline) are generally three to four orders of magnitude lower than the peak values at the WMA S-SX boundary.

Peak values for Case 1 are the highest of the five cases considered. Between the WMA S-SX boundary and the Columbia River shoreline compliance location, the peak industrial worker ILCR varies from 9.98×10^{-3} to 1.33×10^{-6} . Peak ILCR values are driven by technetium-99. The peak industrial worker hazard index varies from 3.00×10^2 to 4.22×10^{-2} . Peak hazard index values are driven by chromium. The peak dose varies from 5.94×10^2 mrem/yr to 7.94×10^{-2} mrem/yr. Peak dose values are driven by technetium-99.

Temporal variations in ILCR for Case 1 are shown in Figure E.32 for compliance points at the WMA S-SX boundary and in Figure E.33 for compliance points between the WMA S-SX boundary and the Columbia River. Temporal variations in hazard index and dose for Case 1 are similar to those shown for ILCR. At the WMA S-SX boundary, peaks for the three cross-sections arrive within approximately the first 50 years and are all relatively sharp. Peaks at the 200 West fence, 200 Area exclusion boundary, and Columbia River shoreline compliance locations arrive after approximately 180, 350, and 550 years, respectively, and are broader than the peaks at the WMA S-SX boundary.

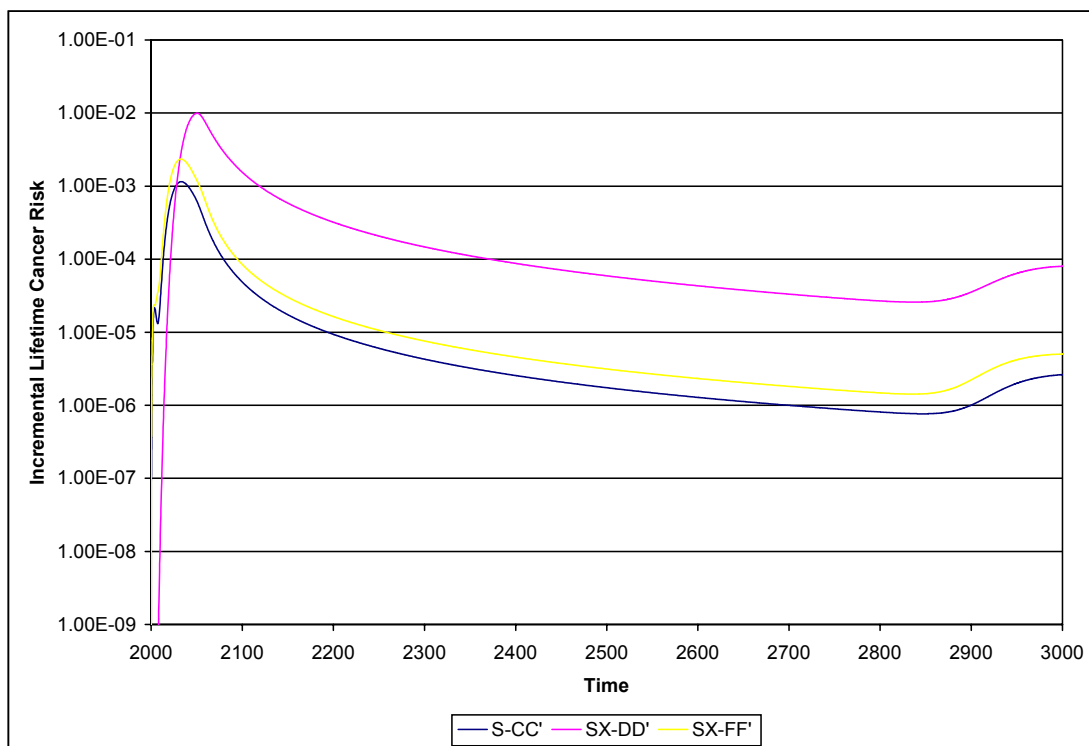
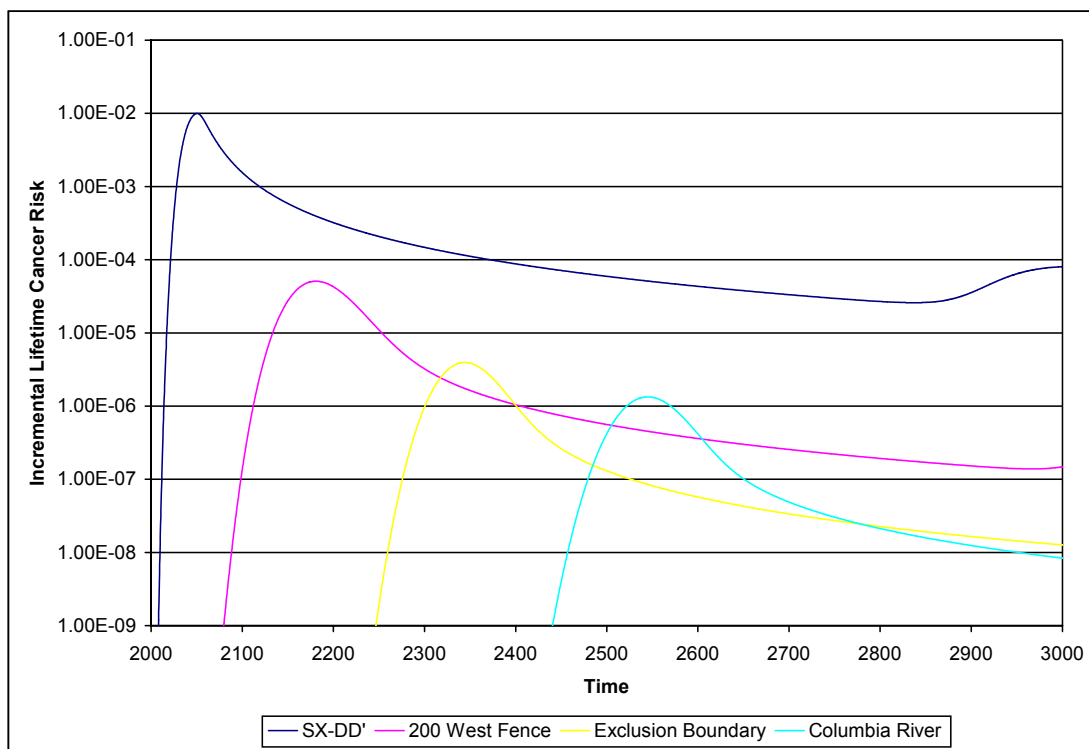
Figure E.32. Case 1 Industrial Worker ILCR Versus Time at WMA S-SX Boundary**Figure E.33. Case 1 Industrial Worker ILCR Versus Time at Compliance Points Between the WMA S-SX Boundary and the Columbia River**

Table E.38. Peak Long-Term Human Health Impacts for Case 1

Compliance Point		Residential Farmer		Industrial Worker		Recreational Shoreline User ^a		MTCA Method B ^b		MTCA Method C ^b		Dose to Worker
		ILCR	HI	ILCR	HI	ILCR	HI	ILCR	HI	ILCR	HI	mrem/yr
S-SX WMA Boundary	S - CC'	4.13E-02	5.07E+03	1.15E-03	1.16E+01	N/A	N/A	N/A	2.13E+02	N/A	9.75E+01	6.91E+01
	SX - DD'	3.57E-01	2.09E+04	9.98E-03	3.00E+02	N/A	N/A	N/A	2.77E+03	N/A	1.26E+03	5.94E+02
	SX - FF'	8.39E-02	6.09E+03	2.34E-03	1.96E+01	N/A	N/A	N/A	5.20E+02	N/A	2.38E+02	1.40E+02
200 West Fence		1.82E-03	7.70E+01	5.07E-05	1.60E+00	N/A	N/A	N/A	1.32E+01	N/A	6.02E+00	3.02E+00
200 Area Exclusion Boundary		1.41E-04	5.98E+00	3.94E-06	1.24E-01	N/A	N/A	N/A	1.02E+00	N/A	4.67E-01	2.35E-01
Columbia River Shoreline		4.77E-05	2.02E+00	1.33E-06	4.22E-02	2.21E-07	4.52E-03	N/A	3.48E-01	N/A	1.59E-01	7.94E-02

^aExposures defined to occur only within 400 m (1,300 ft) of the Columbia River shoreline.

^bCancer risks not shown because MTCA addresses only nonradioactive contaminants and no nonradioactive carcinogenic chemicals were identified as contaminants of concern for WMA S-SX.

HI = hazard index.

ILCR = incremental lifetime cancer risk.

MTCA = Model Toxics Control Act.

N/A = not applicable.

E.6.2 BARRIER ALTERNATIVE AND NO WATER-LINE LEAKS CASE (CASE 2)

Results for Case 2, barrier alternative and no water-line leaks, are summarized in Table E.39. Results for Case 2 show the same general trends regarding the compliance points as discussed above for Case 1. Peak values for Case 2 are generally a factor of 2 to 10 lower than the corresponding values for Case 1. Between the WMA S-SX boundary and the Columbia River shoreline, the peak industrial worker ILCR varies from 1.65×10^{-3} to 5.30×10^{-7} . Peak ILCR values are driven by technetium-99. The peak industrial worker hazard index varies from 2.99×10^1 to 8.79×10^{-3} . Peak hazard index values are driven by chromium and nitrate. The peak dose ranges from 9.85×10^1 mrem/yr to 3.16×10^{-2} mrem/yr. Peak dose values are driven by technetium-99.

Temporal variations in ILCR for Case 2 are shown in Figure E.34 for compliance points at the WMA S-SX boundary and in Figure E.35 for compliance points between the WMA S-SX boundary and the Columbia River. Temporal variations in hazard index and dose for Case 2 are similar to those shown for ILCR. At the WMA S-SX boundary, peak arrival times for the three cross-sections are similar to Case 1 but the peaks are broader in shape. All three peaks arrive within approximately the first 60 years. Peaks at the 200 West fence, 200 Area exclusion boundary, and Columbia River shoreline compliance locations are also similar to and slightly broader than Case 1 and arrive after approximately 180, 350, and 550 years, respectively.

Figure E.34. Case 2 Industrial Worker ILCR Versus Time at WMA S-SX Boundary

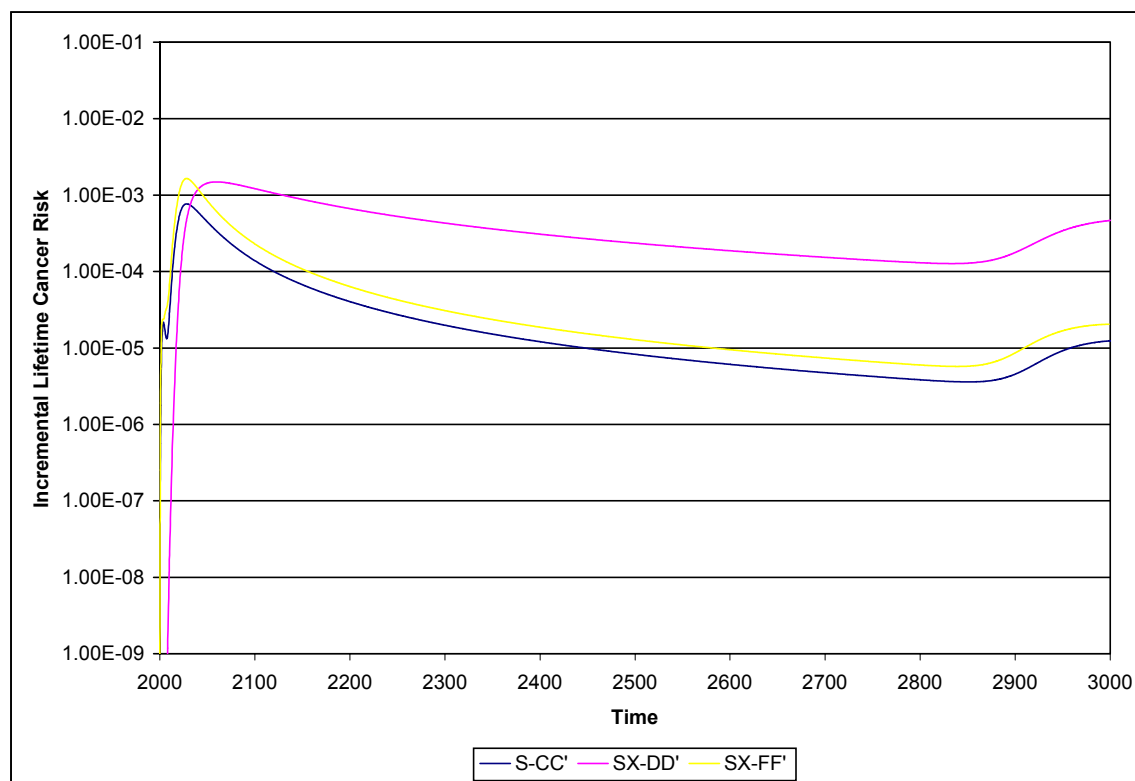


Figure E.35. Case 2 Industrial Worker ILCR Versus Time at Compliance Points Between the WMA S-SX Boundary and the Columbia River

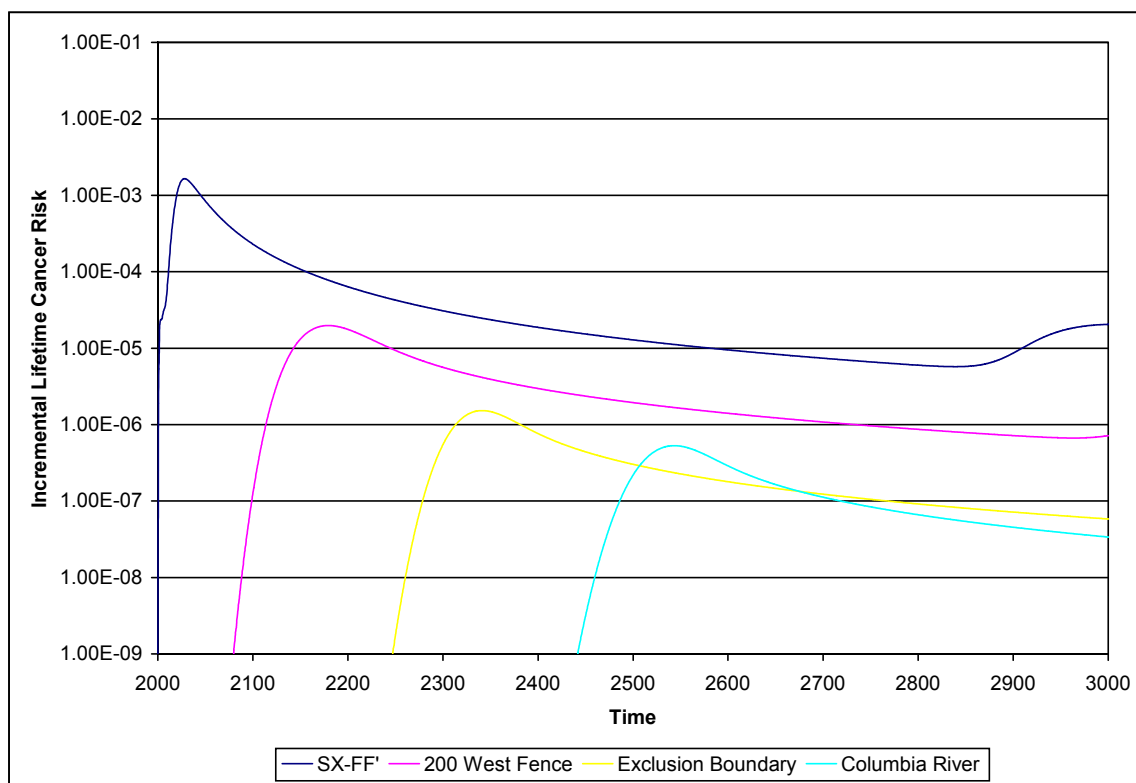


Table E.39. Peak Long-Term Human Health Impacts for Case 2

Compliance Point		Residential Farmer		Industrial Worker		Recreational Shoreline User ^a		MTCA Method B ^b		MTCA Method C ^b		Dose to Worker
		ILCR	HI	ILCR	HI	ILCR	HI	ILCR	HI	ILCR	HI	mrem/yr
S-SX WMA Boundary	S - CC'	2.76E-02	3.43E+03	7.68E-04	5.35E+00	N/A	N/A	N/A	1.36E+02	N/A	6.20E+01	4.61E+01
	SX - DD'	5.32E-02	3.35E+03	1.49E-03	2.99E+01	N/A	N/A	N/A	3.28E+02	N/A	1.57E+02	8.86E+01
	SX - FF'	5.91E-02	4.11E+03	1.65E-03	9.77E+00	N/A	N/A	N/A	3.39E+02	N/A	1.55E+02	9.85E+01
200 West Fence		7.08E-04	3.36E+01	1.98E-05	3.25E-01	N/A	N/A	N/A	3.38E+00	N/A	1.55E+00	1.18E+00
200 Area Exclusion Boundary		5.46E-05	2.60E+00	1.53E-06	2.45E-02	N/A	N/A	N/A	2.58E-01	N/A	1.18E-01	9.10E-02
Columbia River Shoreline		1.90E-05	9.00E-01	5.30E-07	8.79E-03	8.81E-08	9.60E-04	N/A	9.14E-02	N/A	4.18E-02	3.16E-02

^aExposures defined to occur only within 400 m (1,300 ft) of the Columbia River shoreline.

^bCancer risks not shown because MTCA addresses only nonradioactive contaminants and no nonradioactive carcinogenic chemicals were identified as contaminants of concern for WMA S-SX.

HI = hazard index.

ILCR = incremental lifetime cancer risk.

MTCA = Model Toxics Control Act.

N/A = not applicable.

E.6.3 BASE CASE WITH 50 MM/YR METEORIC RECHARGE (CASE 9)

Results for Case 9, base case with 50 mm/yr meteoric recharge, are summarized in Table E.40. Results for Case 9 show the same general trends regarding the compliance points as discussed above for Case 1. Peak values for Case 9 are generally a factor of 2 to 4 lower than the corresponding values for Case 1. Between the WMA S-SX boundary and the Columbia River shoreline, the peak industrial worker ILCR varies from 3.03×10^{-3} to 6.92×10^{-7} . Peak ILCR values are driven by technetium-99. The peak industrial worker hazard index varies from 6.73×10^1 to 1.52×10^{-2} . Peak hazard index values are driven by chromium and nitrate. The peak dose varies from 1.80×10^2 mrem/yr to 4.13×10^{-2} mrem/yr. Peak dose values are driven by technetium-99.

Temporal variations in ILCR for Case 9 are shown in Figure E.36 for compliance points at the WMA S-SX boundary and in Figure E.37 for compliance points between the WMA S-SX boundary and the Columbia River. Temporal variations in hazard index and dose for Case 9 are similar to those shown for ILCR. Overall, the temporal variations for Case 9 resemble those for Case 2. At the WMA S-SX boundary, peaks for the three cross-sections have slightly delayed arrival times and broader shapes compared to Case 1. All three peaks arrive within the first 75 years. Peaks at the 200 West fence, 200 Area exclusion boundary, and Columbia River shoreline compliance locations are also slightly delayed and broadened compared to Case 1.

Figure E.36. Case 9 Industrial Worker ILCR Versus Time at WMA S-SX Boundary

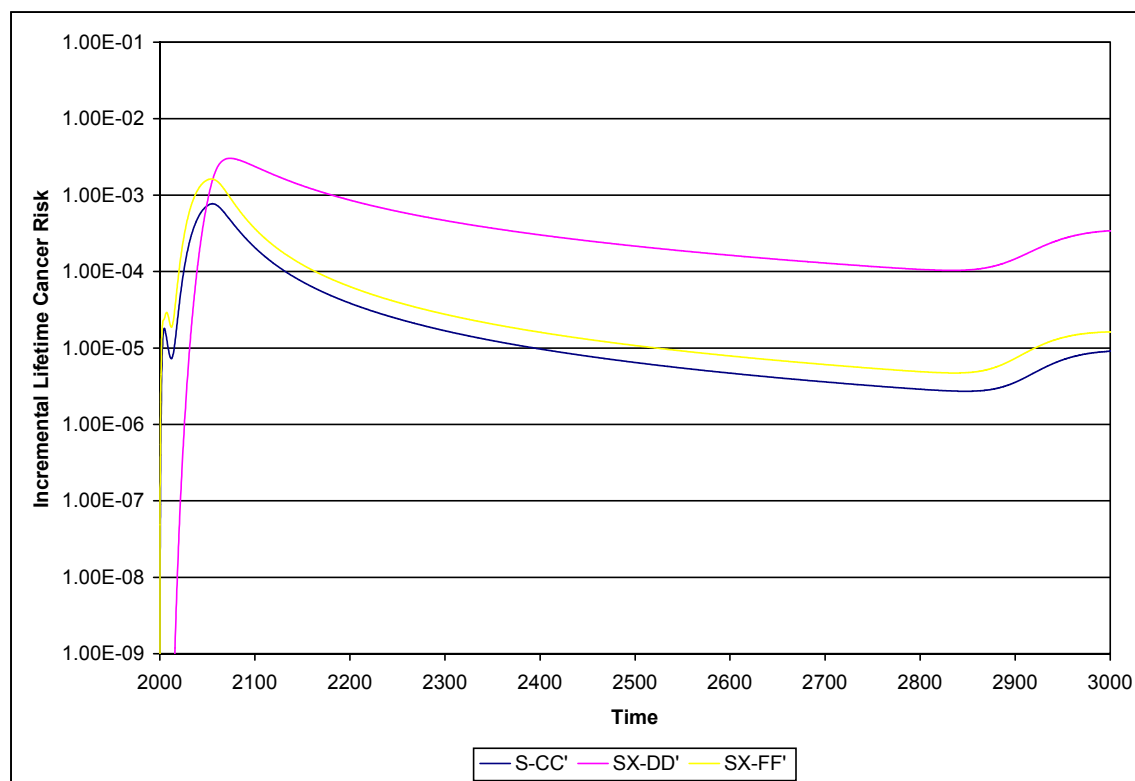


Figure E.37. Case 9 Industrial Worker ILCR Versus Time at Compliance Points Between the WMA S-SX Boundary and the Columbia River

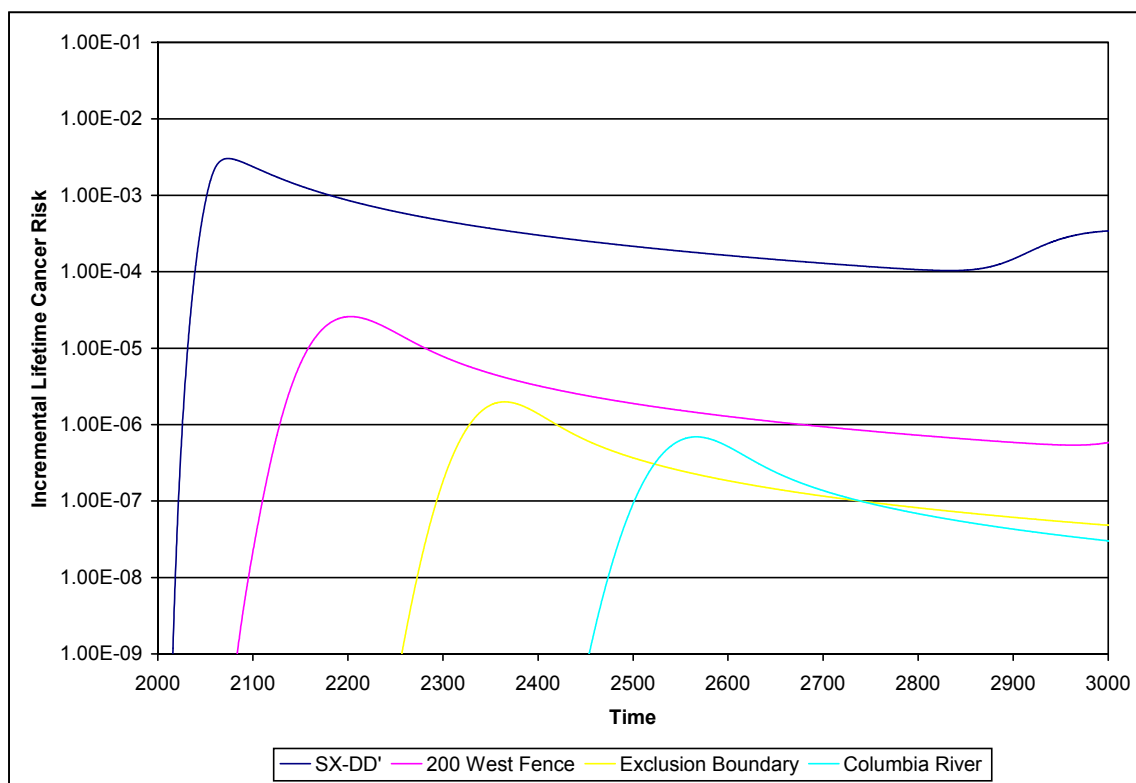


Table E.40. Peak Long-Term Human Health Impacts for Case 9

Compliance Point		Residential Farmer		Industrial Worker		Recreational Shoreline User ^a		MTCA Method B ^b		MTCA Method C ^b		Dose to Worker
		ILCR	HI	ILCR	HI	ILCR	HI	ILCR	HI	ILCR	HI	mrem/yr
S-SX WMA Boundary	S - CC'	2.76E-02	3.40E+03	7.70E-04	6.29E+00	N/A	N/A	N/A	1.40E+02	N/A	6.39E+01	4.63E+01
	SX - DD'	1.08E-01	6.45E+03	3.03E-03	6.73E+01	N/A	N/A	N/A	6.95E+02	N/A	3.18E+02	1.80E+02
	SX - FF'	5.81E-02	4.23E+03	1.62E-03	1.19E+01	N/A	N/A	N/A	3.58E+02	N/A	1.64E+02	9.69E+01
200 West Fence		9.27E-04	4.20E+01	2.59E-05	5.63E-01	N/A	N/A	N/A	5.21E+00	N/A	2.38E+00	1.54E+00
200 Area Exclusion Boundary		7.10E-05	3.22E+00	1.99E-06	4.29E-02	N/A	N/A	N/A	3.97E-01	N/A	1.81E-01	1.18E-01
Columbia River Shoreline		2.48E-05	1.12E+00	6.92E-07	1.52E-02	1.15E-07	1.64E-03	N/A	1.40E-01	N/A	6.40E-02	4.13E-02

^aExposures defined to occur only within 400 m (1,300 ft) of the Columbia River shoreline.

^bCancer risks not shown because MTCA addresses only nonradioactive contaminants and no nonradioactive carcinogenic chemicals were identified as contaminants of concern for WMA S-SX.

HI = hazard index.

ILCR = incremental lifetime cancer risk.

MTCA - Model Toxics Control Act.

N/A = not applicable.

E.6.4 BASE CASE WITH 30 MM/YR METEORIC RECHARGE (CASE 10)

Results for Case 10, base case with 30 mm/yr meteoric recharge, are summarized in Table E.41. Results for Case 10 show the same general trends regarding the compliance points as discussed above for Case 1. Peak values for Case 10 are generally a factor of 2 to 15 lower than the corresponding values for Case 1. Between the WMA S-SX boundary and the Columbia River shoreline, the peak industrial worker ILCR varies from 1.01×10^{-3} to 3.67×10^{-7} . Peak ILCR values are driven by technetium-99. The peak industrial worker hazard index varies from 2.07×10^1 to 5.69×10^{-3} . Peak hazard index values are driven by chromium and nitrate. The peak dose ranges from 6.01×10^1 mrem/yr to 2.19×10^{-2} mrem/yr. Peak dose values are driven by technetium-99.

Temporal variations in ILCR for Case 10 are shown in Figure E.38 for compliance points at the WMA S-SX boundary and in Figure E.39 for compliance points between the WMA S-SX boundary and the Columbia River. Temporal variations in hazard index and dose for Case 10 are similar to those shown for ILCR. At the WMA S-SX boundary, peaks for the three cross-sections are further delayed in arrival times and have even broader shapes compared to Case 9. The three peaks arrive within approximately 125 years. The curves for the three cross-sections begin to rise again after approximately 900 years and are still rising at the end of the 1,000-year analysis period. Peaks at the 200 West fence, 200 Area exclusion boundary, and Columbia River shoreline compliance locations are also further delayed and broadened compared to Case 9.

Figure E.38. Case 10 Industrial Worker ILCR Versus Time at WMA S-SX Boundary

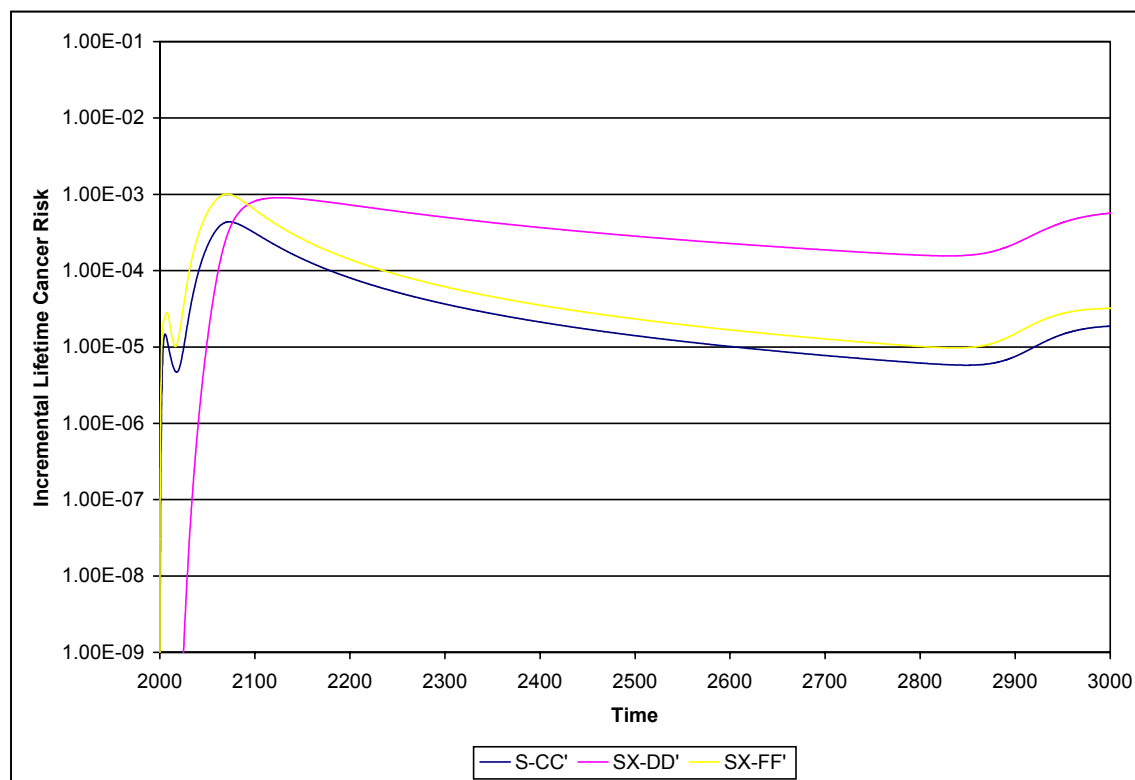


Figure E.39. Case 10 Industrial Worker ILCR Versus Time at Compliance Points Between the WMA S-SX Boundary and the Columbia River

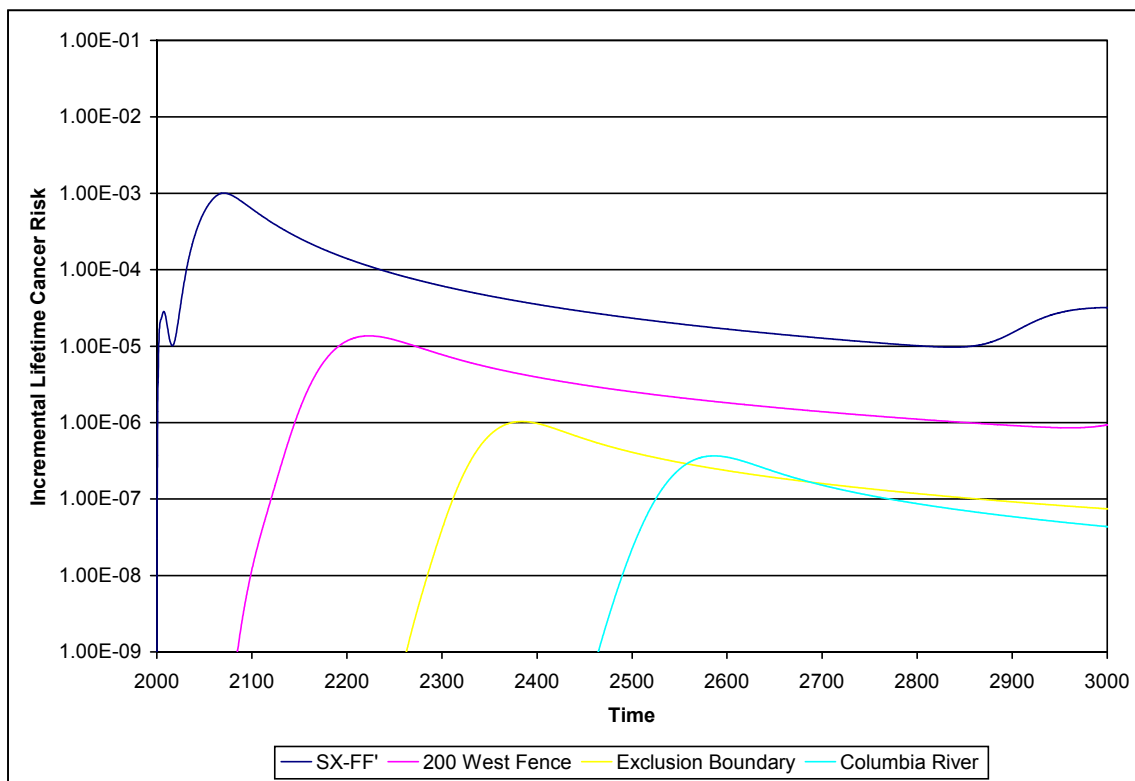


Table E.41. Peak Long-Term Human Health Impacts for Case 10

Compliance Point		Residential Farmer		Industrial Worker		Recreational Shoreline User ^a		MTCA Method B ^b		MTCA Method C ^b		Dose to Worker
		ILCR	HI	ILCR	HI	ILCR	HI	ILCR	HI	ILCR	HI	mrem/yr
S-SX WMA Boundary	S - CC'	1.56E-02	1.95E+03	4.36E-04	3.08E+00	N/A	N/A	N/A	7.75E+01	N/A	3.54E+01	2.61E+01
	SX - DD'	3.23E-02	1.98E+03	9.02E-04	2.07E+01	N/A	N/A	N/A	1.98E+02	N/A	9.03E+01	5.37E+01
	SX - FF'	3.61E-02	2.60E+03	1.01E-03	6.30E+00	N/A	N/A	N/A	2.15E+02	N/A	9.82E+01	6.01E+01
200 West Fence		4.88E-04	2.36E+01	1.36E-05	2.11E-01	N/A	N/A	N/A	2.23E+00	N/A	1.02E+00	8.14E-01
200 Area Exclusion Boundary		3.70E-05	1.79E+00	1.03E-06	1.57E-02	N/A	N/A	N/A	1.67E-01	N/A	7.63E-02	6.17E-02
Columbia River Shoreline		1.31E-05	6.34E-01	3.67E-07	5.69E-03	6.10E-08	6.22E-04	N/A	6.02E-02	N/A	2.75E-02	2.19E-02

^aExposures defined to occur only within 400 m (1,300 ft) of the Columbia River shoreline.

^bCancer risks not shown because MTCA addresses only nonradioactive contaminants and no nonradioactive carcinogenic chemicals were identified as contaminants of concern for WMA S-SX.

HI = hazard index.

ILCR = incremental lifetime cancer risk.

MTCA - Model Toxics Control Act.

N/A = not applicable.

E.6.5 BASE CASE WITH 10 MM/YR METEORIC RECHARGE (CASE 11)

Results for Case 11, base case with 10 mm/yr meteoric recharge, are summarized in Table E.42. Results for Case 11 show the same general trends regarding the compliance points as discussed above for Case 1. Peak values for Case 11 are generally a factor of 15 to 50 lower than the corresponding values for Case 1. Between the WMA S-SX boundary and the Columbia River shoreline, the peak industrial worker ILCR varies from 5.94×10^{-4} to 8.59×10^{-8} . Peak ILCR values are driven by technetium-99. The peak industrial worker hazard index varies from 1.25×10^1 to 7.54×10^{-4} . Peak hazard index values are driven by chromium. The peak dose varies from 3.26×10^1 mrem/yr to 5.12×10^{-3} mrem/yr. Peak dose values are driven by technetium-99.

Temporal variations in ILCR for Case 11 are shown in Figure E.40 for compliance points at the WMA S-SX boundary and in Figure E.41 for compliance points between the WMA S-SX boundary and the Columbia River. Temporal variations in hazard index and dose for Case 11 are similar to those shown for ILCR. At the WMA S-SX boundary, peaks for the three cross-sections are even further delayed in arrival times and have even broader shapes compared to Case 10. The secondary elevation in ILCR values observed for Case 10 at the end of the 1,000-year analysis period is also observed for Case 11 but is more pronounced. For cross-section SX-DD', the late ILCR peak actually exceeds the earlier peak. Peaks at the 200 West Fence, 200 Area exclusion boundary, and Columbia River shoreline compliance locations are also even further delayed and broadened compared to Case 10 and arrive after approximately 300, 480, and 680 years, respectively.

Figure E.40. Case 11 Industrial Worker ILCR Versus Time at WMA S-SX Boundary

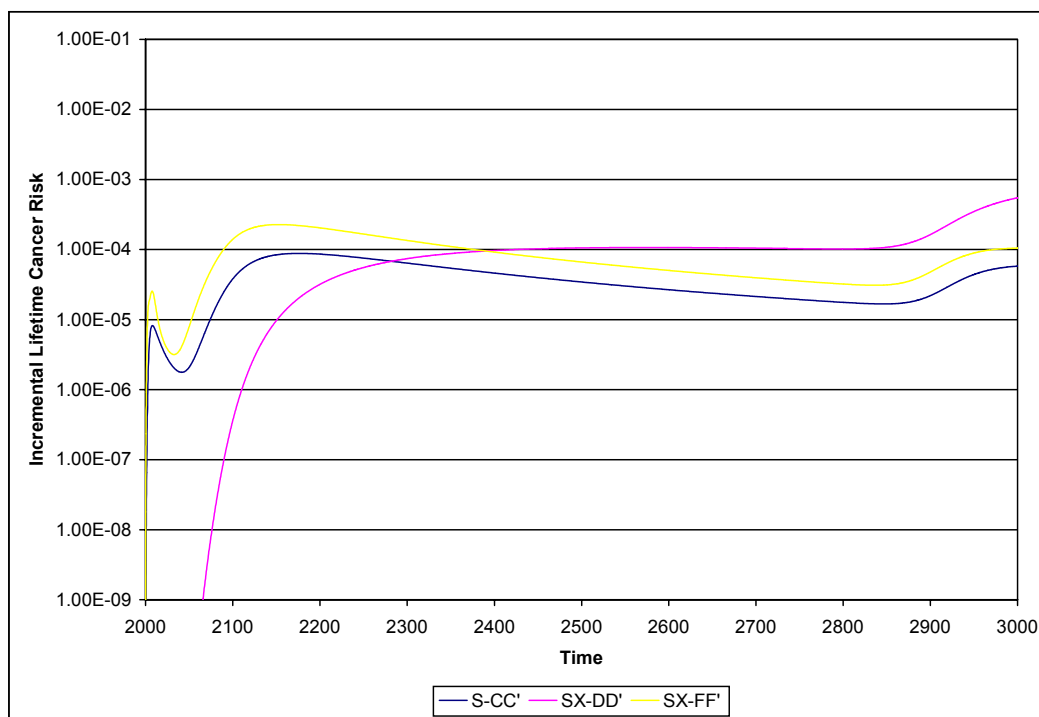


Figure E.41. Case 11 Industrial Worker ILCR Versus Time at Compliance Points Between the WMA S-SX Boundary and the Columbia River

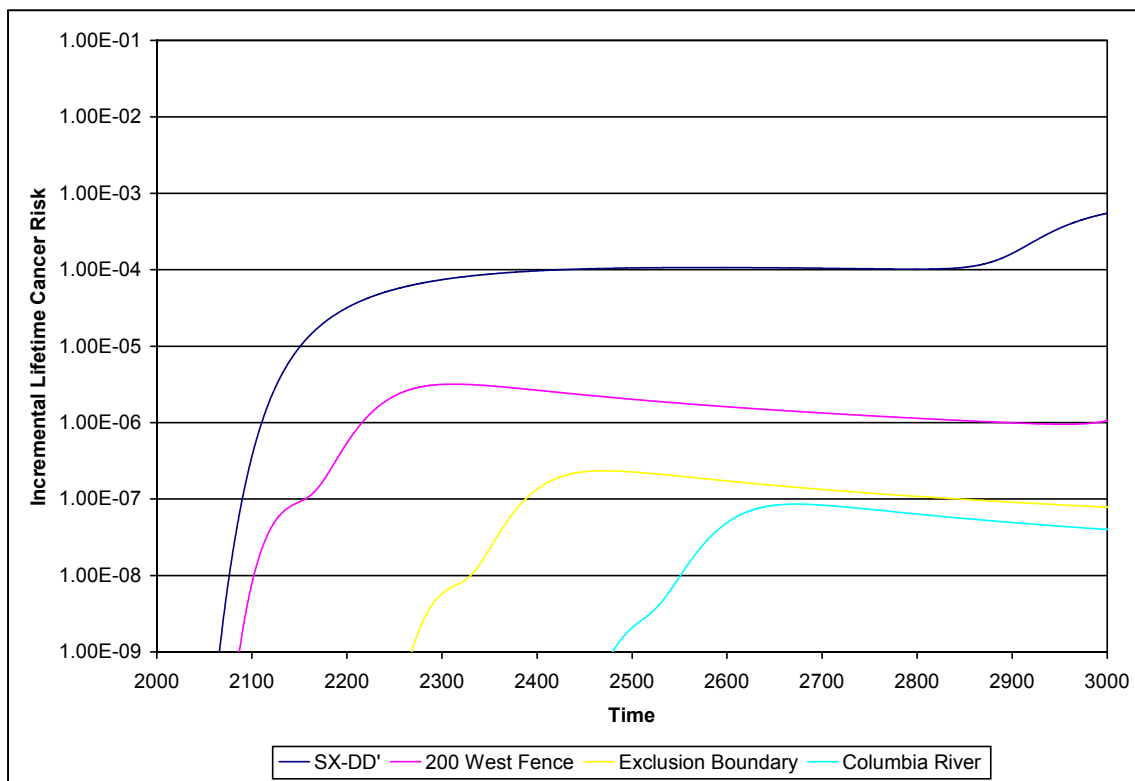


Table E.42. Peak Long-Term Human Health Impacts for Case 11

Compliance Point		Residential Farmer		Industrial Worker		Recreational Shoreline User ^a		MTCA Method B ^b		MTCA Method C ^b		Dose to Worker
		ILCR	HI	ILCR	HI	ILCR	HI	ILCR	HI	ILCR	HI	mrem/yr
S-SX WMA Boundary	S - CC'	3.16E-03	4.08E+02	8.82E-05	7.67E-01	N/A	N/A	N/A	1.59E+01	N/A	7.25E+00	5.29E+00
	SX - DD'	1.96E-02	1.12E+03	5.49E-04	1.25E+01	N/A	N/A	N/A	1.27E+02	N/A	5.82E+01	3.26E+01
	SX - FF'	8.14E-03	5.94E+02	2.27E-04	1.43E+00	N/A	N/A	N/A	4.84E+01	N/A	2.21E+01	1.36E+01
200 West Fence		1.14E-04	5.70E+00	3.19E-06	2.81E-02	N/A	N/A	N/A	3.85E-01	N/A	1.76E-01	1.90E-01
200 Area Exclusion Boundary		8.40E-06	4.19E-01	2.35E-07	2.04E-03	N/A	N/A	N/A	2.81E-02	N/A	1.28E-02	1.40E-02
Columbia River Shoreline		3.07E-06	1.54E-01	8.59E-08	7.54E-04	1.43E-08	8.38E-05	N/A	1.03E-02	N/A	4.73E-03	5.12E-03

^aExposures defined to occur only within 400 m (1,300 ft) of the Columbia River shoreline.

^bCancer risks not shown because MTCA addresses only nonradioactive contaminants and no nonradioactive carcinogenic chemicals were identified as contaminants of concern for WMA S-SX.

HI = hazard index.

ILCR = incremental lifetime cancer risk.

MTCA = Model Toxics Control Act.

N/A = not applicable.

E.7.0 REFERENCES

- 40 CFR 141, "National Primary Drinking Water Regulations," *Code of Federal Regulations*, as amended.
- 64 FR 61615, 1999, "Hanford Comprehensive Land-Use Plan Environmental Impact Statement (HCP EIS), Hanford Site, Richland, Washington; Record of Decision (ROD)," *Federal Register*, Vol. 64, No. 218 pp 61615, November 12.
- Agnew, S. F., 1997, *Hanford Defined Wastes: Chemical and Radionuclide Compositions*, LA-UR-96-3860, Rev. 4, Los Alamos National Laboratory, Los Alamos, New Mexico.
- Atomic Energy Act of 1954*, 42 USC 2011 et seq., as amended.
- Baetlsé, L. H., 1969, "Migration of radionuclides in porous media," *Progress in Nuclear Energy, Series XII, Health Physics*, ed. A. M. F. Duhamel, p. 707-730, Pergamon Press, Elmsford, New York.
- DOE, 1999, *Hanford Remedial Action Environmental Impact Statement and Comprehensive Land Use Plan*, DOE/EIS-0222F, U.S. Department of Energy, Washington, D.C.
- DOE and Ecology, 1996, *Tank Waste Remediation System, Hanford Site, Richland, Washington, Final Environmental Impact Statement*, DOE/EIS-0189, U.S. Department of Energy and Washington State Department of Ecology, Washington, D.C.
- DOE-GJPO, 1997, *Tank Summary Data Report for Tank S-104*, U.S. Department of Energy, Grand Junction Projects Office, Grand Junction, Colorado.
- DOE-RL, 1995a, *Corrective Measures Study for the 100-NR-1 and 100-NR-2 Operable Units*, DOE/RL-95-111, Rev. 0, U.S. Department of Energy, Richland Operations Office, Richland, Washington.
- DOE-RL, 1995b, *Hanford Site Risk Assessment Methodology*, DOE/RL-91-45, Rev. 3, U.S. Department of Energy, Richland Operations Office, Richland, Washington.
- DOE-RL, 1995c, *Limited Field Investigation for the 200-UP-2 Operable Unit*, Rev. 0, DOE/RL-95-13, U.S. Department of Energy, Richland Operations Office, Richland, Washington.
- DOE-RL, 1996, *Programmatic Agreement Among the U.S. Department of Energy, Richland Operations Office, the Advisory Council on Historic Preservation, and the Washington State Historic Preservation Office for the Maintenance, Deactivation, Alteration, and Demolition of the Built Environment on the Hanford Site, Washington*, DOE/RL-96-77, Rev. 0, U.S. Department of Energy, Richland Operations Office, Richland, Washington.
- DOE-RL, 1999a, *Hanford Immobilized Low-Activity Tank Waste Performance Assessment*, DOE/RL-97-69, Rev. 0, U.S. Department of Energy, Richland Operations Office, Richland, Washington.

- DOE-RL, 1999b, *Retrieval Performance Evaluation Methodology for the AX Tank Farm*, DOE/RL-98-72, U.S. Department of Energy, Richland Operations Office, Richland, Washington.
- DOE-RL, 2000, *Phase I RCRA Facility Investigation/Corrective Measures Study Work Plan for Single-Shell Tank Waste Management Areas*, DOE/RL-99-36, Rev. 1, U.S. Department of Energy, Richland Operations Office, Richland, Washington.
- EPA, 1995, *Record of Decision for the U.S. DOE Hanford 100 Areas; 100-BC-1, 100-DR-1, 100-HR-1 Operable Units*, Hanford Site, Benton County, Washington, U.S. Environmental Protection Agency, Region 10, Richland, Washington.
- EPA, 2000a, *Integrated Risk Information System*, at <http://www.epa.gov/radiation/heast/userguid.htm> as of September 28, U.S. Environmental Protection Agency, Washington, D.C.
- EPA, 2000b, *User's Guide: Radionuclide Carcinogenicity*, at <http://www.epa.gov/radiation/heast/userguid.htm> as of September 28, U.S. Environmental Protection Agency, Washington, D.C.
- Freeze, R. A., and J. A. Cherry, 1979, *Groundwater*, p. 394-395, Prentice-Hall, Inc., Englewood Cliffs, New Jersey.
- FSUWG, 1992, *The Future of Hanford: Uses and Cleanup, The Final Report of the Hanford Future Site Uses Working Group*, Hanford Future Site Uses Working Group, Westinghouse Hanford Company, Richland, Washington.
- Gardner, W. R., 1958, "Some Steady-State Solutions of the Unsaturated Moisture Flow Equation with Applications to Evaporation from a Water Table," *Soil Sci.* 85:228-232.
- Gelhar, L. W., 1993, *Stochastic Subsurface Hydrology*, Prentice Hall, New York.
- Goodman, D., 2000, *Estimation of SX-Farm Vadose Zone Cs-137 Inventories from Geostatistical Analysis of Drywell and Soil Core Data*, HNF-5782, Rev. 0, Montana State University, Bozeman, Montana.
- Johnson, V., T. Jones, S. Reidel, and M. Wood, 1999, *Subsurface Physical Conditions Description of the S-SX Waste Management Area*, HNF-4963, Rev. 0, Lockheed Martin Hanford Corporation, Richland, Washington.
- Jones, T. E., R. A. Watrous, and G. T. Maclean, 2000, *Inventory Estimates for Single-Shell Tank Leaks in S and SX Tank Farms*, RPP-6285, Rev. 0, CH2M HILL Hanford Group, Inc., Richland, Washington.
- Kaplan, D. L., and R. J. Serne, 1999, *Geochemical Data Package For the Immobilized Low-Activity Waste Performance Assessment*, PNNL-13037, Pacific Northwest National Laboratory, Richland, Washington.

- Khaleel, R., J. F. Relyea, and J. L. Conca, 1995, "Evaluation of van Genuchten-Mualem Relationships to Estimate Unsaturated Conductivity at Low Water Contents," *Water Resource Research*, 31:2659-2668.
- Khaleel, R. and J. F. Relyea, 1997, "Correcting Laboratory-Measured Moisture Retention Data for Gravels," *Water Resource Research*, 33:1875-1878.
- Khaleel, R., 1999, *Far-Field Hydrology Data Package for Immobilized Low-Activity Tank Waste Performance Assessment*, HNF-4769, Rev. 1, Fluor Daniel Northwest, Inc. Richland, Washington.
- Khaleel, R., T. E. Jones, A. J. Knepp, F. M. Mann, D. A. Myers, P. M. Rogers, R. J. Serne, and M. I. Wood, 2000, *Modeling Data Package for S-SX Field Investigation Report (FIR)*, RPP-6296, Rev. 0, CH2M HILL Hanford Group, Inc., Richland, Washington.
- Kincaid, C. T., J. W. Shade, G. A. Whyatt, M. G. Piepho, K. Rhoads, J. A. Voogd, J. H. Westsik, Jr., M. D. Freshley, K. A. Blanchard, and B. G. Lauzon, 1995, *Performance Assessment of Grouted Double-Shell Tank Waste Disposal at Hanford*, WHC-SD-WM-EE-004, Rev. 1, Westinghouse Hanford Company, Richland, Washington.
- Kincaid, C. T., M. P. Bergeron, C. R. Cole, M. D. Freshley, N. L. Hassig, V. G. Johnson, D. I. Kaplan, R. J. Serne, G. P. Streile, D. L. Strenge, P. D. Thorne, L. W. Vail, G. A. Whyatt, S. K. Wurstner, 1998, *Composite Analysis for Low-Level Waste Disposal in the 200 Area Plateau of the Hanford Site*, PNNL-11800, Pacific Northwest National Laboratory, Richland, Washington.
- Law, A., S. Panday, C. Denslow, K. Fecht, and A. Knepp, 1996, *Hanford Sitewide Groundwater Flow and Transport Model Calibration Report*, BHI-00608, Rev. 0, Bechtel Hanford, Inc., Richland, Washington.
- Lu, A. H., 1996, *Contaminant Transport in the Unconfined Aquifer: Input to the Low-Level Tank Waste Interim Performance Assessment*, WHC-SD-WM-RPT-241, Rev. 0, Westinghouse Hanford Company, Richland, Washington.
- Millington, R. J., and J. P. Quirk, 1961, "Permeability of Porous Solids," *Trans. Faraday Soc.*, 57:1200-1207.
- "Model Toxics Control Act," RCW 70.105D, *Revised Code of Washington*, as amended.
- Mualem, Y., 1976, "A New Model for Predicting the Hydraulic Conductivity of Unsaturated Porous Media," *Water Resource Research*, 12:513-522.
- Parker, J. C., and M. Th. van Genuchten, 1984a, "Flux-Averaged and Volume-Averaged Concentrations in Continuum Approaches to Solute Transport," *Water Resources Research*, 20(7) p. 886-872.

- Parker, J. C., and M. Th. van Genuchten, 1984b, *Determining Transport Parameters from Laboratory and Field Tracer Experiments*, Bulletin 4-3, Virginia Agriculture Experiment Station, Blacksburg, Virginia.
- Polmann, D. J., 1990, *Application of Stochastic Methods to Transient Flow and Transport in Heterogeneous Unsaturated Soils*, Ph.D. Thesis, Massachusetts Institute of Technology, Cambridge, Massachusetts.
- Price, W. H. and K. R. Fecht, 1976a, *Geology of the 241-S Tank Farm*, ARH-LD-133, Atlantic Richfield Hanford Company, Richland, Washington.
- Price, W. H., and K. R. Fecht, 1976b, *Geology of the 241-SX Tank Farm*, ARH-LD-134, Atlantic Richfield Hanford Company, Richland, Washington.
- Raymond, R. E., and E. G. Shdo, 1966, *Characterization of Subsurface Contamination in the SX Farm*, BNWL-CC-701, Battelle Northwest Laboratory, Richland, Washington.
- Resource Conservation and Recovery Act of 1976*, 42 USC 6901, et seq.
- Rittmann, P. D., 1999, *Exposure Scenarios and Unit Dose Factors for the Hanford Immobilized Low-Activity Tank Waste Performance Assessment*, HNF-SD-WM-TI-707, Rev. 1, Fluor Daniel Northwest, Inc., Richland, Washington.
- Talbott, M. E., and L. W. Gelhar, 1994, *Performance Assessment of a Hypothetical Low-Level Waste Facility: Groundwater Flow and Transport Simulation*, NUREG/CR-6114 Vol. 3, U.S. Nuclear Regulatory Commission, Washington, D.C.
- Thompson, R. R., 2001, *Retrieval Performance Evaluation for Single-Shell Tanks S-112 and S-102*, HNF-7644, Rev. 0, CH2M HILL Hanford Group, Inc., Richland, Washington.
- van der Kamp, G., L. D. Luba, J. A. Cherry, and H. Maathuis, 1994, "Field Study of a Long and Very Narrow Contaminant Plume," *Ground Water*, 32:1008-1016.
- van Genuchten, M. Th., 1974, *Mass Transfer Studies in Sorbing Porous Media*, Ph. D. Thesis, New Mexico State University, Las Cruces, New Mexico.
- van Genuchten, M. Th., 1980, "A Closed-Form Solution for Predicting the Conductivity of Unsaturated Soils," *Soil Sci. Soc. Am. J.*, 44:892-898.
- van Genuchten, M. Th., F. J. Leij, and S. R. Yates, 1991, *The RETC Code for Quantifying the Hydraulic Functions of Unsaturated Soils*, EPA/600/2-91/065, U.S. Environmental Protection Agency, Washington, D.C.
- WAC 173-340, "The Model Toxics Control Act Cleanup Regulation," *Washington Administrative Code*, as amended.

- Ward, A. L., G. W. Gee, and M. D. White, 1997, *A Comprehensive Analysis of Contaminant Transport in the Vadose Zone Beneath Tank SX-109*, PNNL-11463, Pacific Northwest National Laboratory, Richland, Washington.
- White, M. D., and M. Oostrom, 2000a, *STOMP Subsurface Transport Over Multiple Phases, Version 2.0, Theory Guide*, PNNL-12030, UC-2010, Pacific Northwest National Laboratory, Richland, Washington.
- White, M. D., and M. Oostrom, 2000b, *STOMP Subsurface Transport Over Multiple Phases, Version 2.0, User's Guide*, PNNL-12034, UC-2010, Pacific Northwest National Laboratory, Richland, Washington.
- White, M. D., M. Oostrom, and M. D. Williams, 2001, *FY00 Initial Assessments for S-SX Field Investigation Report (FIR): Simulations of Contaminant Migration with Surface Barriers*, PNWD-3111, Battelle, Pacific Northwest Division, Richland, Washington.
- Yeh, T. C. J., L. W. Gelhar, and A. L. Gutjahr, 1985, "Stochastic Analysis of Unsaturated Flow in Heterogeneous Soils, 2. Statistically Anisotropic Media with Variable α ," *Water Resource Research*, 21:457-464.

This page intentionally left blank.